The Subsurface Fluid Mechanics
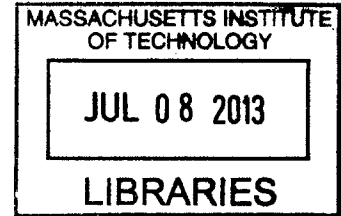# of Geologic Carbon Dioxide Storage

by

Michael Lawrence Szulczewski

S.B. Earth, Atmospheric, and Planetary Science
Massachusetts Institute of Technology, 2005

S.M. Civil and Environmental Engineering
Massachusetts Institute of Technology, 2009

Submitted to the Department of Civil and Environmental Engineering
in partial fulfillment of the requirements for the degree of

Doctor of Philosophy in the Field of Civil and Environmental Engineering

at the

MASSACHUSETTS INSTITUTE OF TECHNOLOGY

June 2013

Author . . . .
Department of Civil and Environmental Engineering
April 30, 2013

Certified by . . . .
Ruben Juanes
Associate Professor of Civil and Environmental Engineering
Thesis Supervisor

Accepted by . . . .
Heidi M. Nepf
Chair, Departmental Committee for Graduate Students

The Subsurface Fluid Mechanics
of Geologic Carbon Dioxide Storage

by

Michael Lawrence Szulczewski

Submitted to the Department of Civil and Environmental Engineering
on April 30, 2013, in partial fulfillment of the
requirements for the degree of
Doctor of Philosophy in the Field of Civil and Environmental Engineering

Abstract

In carbon capture and storage (CCS), CO_2 is captured at power plants and then injected into deep geologic reservoirs for long-term storage. While CCS may be critical for the continued use of fossil fuels in a carbon-constrained world, the subsurface behavior of CO_2 remains poorly understood, which has contributed to the absence of government policy to implement CCS. In this Thesis, we use simulations, experiments, and theory to clarify the fluid mechanics of CO_2 storage, with the goal of informing two practical questions.

The first question is, how much CO_2 can be stored in the United States? This question is important to clarify the role of CCS among the portfolio of other climate-change mitigation options, such as renewable energy and reduced energy consumption. To address this question, we develop models of CO_2 injection and the post-injection migration, and apply them to several reservoirs in the US. We use the models to calculate the total amount of CO_2 that can be stored in these reservoirs without hydraulically fracturing the caprock or allowing the CO_2 to migrate to a major leakage pathway. We find that the US has sufficient storage capacity to stabilize emissions at the current rates for at least 100 years.

The second question is, what are the long-term dissolution rates of CO_2 into the ambient groundwater? This question is important because dissolution mitigates the risk of CO_2 leakage to shallower formations or the surface. We address this question for storage in structural and stratigraphic traps, which are promising locations in a reservoir for injection and will likely be the first sites of large-scale CCS deployment. We describe several mechanisms of CO_2 dissolution in these traps and develop models to predict the dissolution rates. We apply the models to relevant subsurface conditions and find that dissolution rates vary widely depending on the reservoir properties, but that thick reservoirs with high permeabilities could potentially dissolve hundreds of megatons of CO_2 in tens of years.

Thesis Supervisor: Ruben Juanes
Title: Associate Professor of Civil and Environmental Engineering

Acknowledgments

I am deeply grateful to my family, friends, and mentors who have all contributed, in one way or another, to this work. Thank you to:

Contents

List of Figures

Chapter 1

Introduction

A growing body of research indicates that anthropogenic CO_2 emissions are a major contributor to climate change [51], and suggests that avoiding the most damaging effects of climate change requires stabilizing worldwide emissions at the current rate or lower [70, 163]. The most comprehensive and promising proposals for achieving stabilization include several approaches, such as reducing energy consumption; increasing the efficiency of vehicles, buildings, and power plants; and replacing fossil fuels with low-carbon energy sources [133]. To reduce emissions in the short term while fossil fuels continue to supply most of the planet's primary power, carbon capture and storage (CCS) may be critical.

In CCS, CO_2 is captured from the flue gas of power plants or factories, compressed into a supercritical fluid, and then injected underground into reservoirs like deep saline aquifers for long-term storage [80, 92, 142, 19, 131]. These aquifers are typically one to three kilometers underground, ten to five hundred meters thick, and hundreds of kilometers long. They usually consist of a layer of cemented sediments covered by a low-permeability layer called a caprock that retards the upward flow of CO_2 back to the surface. They are saturated with water that ranges from brackish to at least ten times as salty as seawater [85]. Due to their depth and high salinity, they are almost never used for drinking or irrigation water, but rather have been used to store industrial waste for decades [80].

While CCS is a promising option to reduce anthropogenic emissions, the injection of CO_2 and its behavior in the subsurface remain poorly understood. For example, some studies claim that the rise in reservoir pressure accompanying large-scale CO_2 injection will trigger earthquakes and cause leakage, rendering CCS "a risky, and likely unsuccessful,

11

strategy for signicantly reducing greenhouse gas emissions" [172]. In contrast, others cite the successful history of waste-water disposal in the subsurface [29] and argue for more research on injection-related phenomena [83]. The behavior of CO_2 after injection is also contested. While some studies find that convective dissolution of CO_2 into the ambient groundwater depends on properties such as the diffusivity and reservoir thickness [11, 123], others find it is independent under certain conditions [135, 69]. This type of uncertainty in post-injection behavior is reflected in uncertainty of storage capacities: some studies estimate that the US can store only a few years of emissions from coal- and gas-fired power plants [20], while others predict storage for thousands of years of emissions [120].

In this Thesis, we use simulations, theory, and experiments to clarify the subsurface behavior of CO_2 during CCS. In Chapter 2, we develop models of CO_2 injection and post-injection migration, and use them to quantify the storage capacity of 11 deep geologic reservoirs in the United States. The results have been published previously [150]. In Chapter 3, we briefly study a more abstract problem—the evolution of miscible gravity currents in porous layers—to develop part of the theoretical basis required to investigate CO_2 dissolution. These results have also been published previously [148]. In Chapter 4, we apply and extend the theory from Chapter 3 to study CO_2 dissolution during storage in structural and stratigraphic traps.

Chapter 2

The lifetime of carbon capture and storage as a climate-change mitigation technology

2.1 Summary

In this chapter, we clarify the potential of carbon capture and storage to mitigate emissions in the US by quantifying the nationwide storage capacity. We develop a storage-capacity supply curve that, unlike current large-scale capacity estimates, is derived from the fluid mechanics of CO_2 injection and trapping, and incorporates injection-rate constraints. We show that storage supply is a dynamic quantity that grows with the duration of CCS, and we interpret the lifetime of CCS as the time for which the storage supply curve exceeds the storage demand curve from CO_2 production. We show that in the US, if CO_2 production from power generation continues to rise at recent rates, then CCS can store enough CO_2 to stabilize emissions at current levels for at least 100 years. This result suggests that the large-scale implementation of CCS is a geologically-viable climate-change mitigation option in the US over the next century.

2.2 Introduction

Carbon dioxide is a well-documented greenhouse gas, and a growing body of evidence indicates that anthropogenic CO_2 emissions are a major contributor to climate change [51]. One

13

promising technology to mitigate CO_2 emissions is carbon capture and storage (CCS) [92, 133, 80]. In the context of this study, CCS involves capturing CO_2 from the flue gas of power plants, compressing it into a supercritical fluid, and then injecting it into deep saline aquifers for long-term storage [80, 131]. Compared to other mitigation technologies such as renewable energy, CCS is important because it may enable the continued use of fossil fuels, which currently supply over 80% of the primary power for the planet [70, 116]. We focus on CO_2 produced by power plants because electric power generation currently accounts for more than 40% of worldwide CO_2 emissions [78], and because power plants are large, stationary point sources of emissions where CO_2 capture technology will likely be deployed first [80]. We further restrict our analysis to coal- and gas-fired power plants because they emit more CO_2 than any other type of plant: since 2000, they have emitted approximately 97% by mass of the total CO_2 produced by electricity-generating power plants in the US [158]. We focus on storing this CO_2 in deep saline aquifers because they are geographically widespread and their storage capacity is potentially very large [80, 131].

We define the storage capacity of a saline aquifer to be the maximum amount of CO_2 that could be injected and securely stored under geologic constraints, such as the aquifer's size and the integrity of its caprock. Regulatory, legal, and economic factors such as land-use constraints and the locations of power plants will ultimately play an important role in limiting the degree to which this capacity can be utilized [10, 120, 38], but they do not contribute to the estimates of storage capacity in this study.

Although CCS has been identified as the critical enabling technology for the continued use of fossil fuels in a carbon-constrained world [116], the role it can play among the portfolio of climate-change mitigation options remains unclear. This is due in part to uncertainty in the total amount of CO_2 that CCS could store, and therefore uncertainty in the timespan over which it could be extended into the future. Storage capacity estimates for the United States, for example, range over almost four orders of magnitude: from about five [20] to 20,000 billion metric tons (Gt) of CO_2 [120], with other estimates falling in between [39]. This uncertainty in capacity leads to large uncertainty in the potential lifetime of CCS: at a storage rate of 1 Gt CO_2 per year, which is about one sixth of US emissions [158], CCS could operate from 5 to 20,000 years.

An important factor contributing to the uncertainty in storage capacity is the high uncertainty in the hydrogeologic data for deep saline aquifers—recent estimates [120] make use

14

of much larger and more sophisticated datasets than earlier estimates [20]. The large range is also due to the complexity of the storage process: since the subsurface fluid dynamics of CO_2 storage is complicated, studies use different simplifying assumptions and methodologies to estimate large-scale capacity, such as assuming that the entire pore volume of an aquifer is saturated with dissolved CO_2 [39], or extrapolating storage capacities from an ensemble of local-scale simulations [10, 120]. Moreover, the impact of injection-rate constraints due to pressure buildup is not clear. For example, some studies of CO_2 injection support the adoption of CCS with injection-rate management [22], while others conclude that injection constraints render CCS infeasible [44].

Here, we clarify the potential of CCS to mitigate emissions in the US. We develop a storage capacity model that advances previous efforts by explicitly capturing the fluid dynamics of CO_2 storage as well as injection-rate constraints. We treat geologic capacity as a supply of storage space, and the amount of CO_2 that needs to be stored as a demand for that space. We then interpret the lifetime of CCS in the US as the time for which supply exceeds demand.
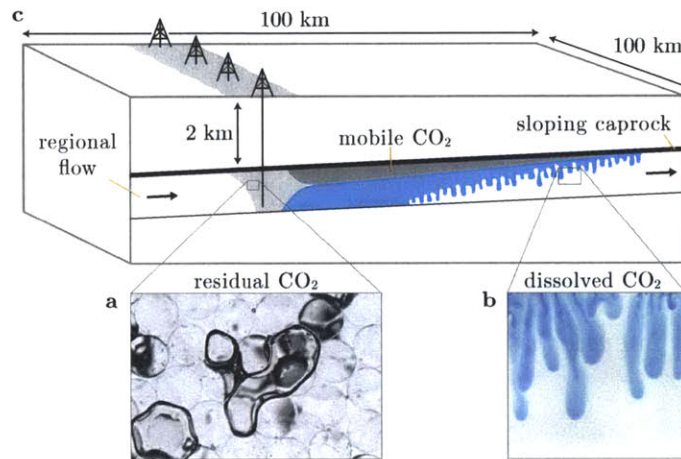
Figure 2-1: Residual and solubility trapping are the key trapping mechanisms that contribute to the CO_2 storage capacity. Inset (**a**) shows blobs of gas immobilized by residual trapping in an experimental analog system: a glass-bead pack saturated with water. Inset (**b**) shows solubility trapping in a different analog system: a Hele-Shaw cell saturated with water, topped with a source of dense, dyed water. As in the CO_2 system, in which the brine with dissolved CO_2 is denser than the ambient brine, dissolution occurs via finger-like protrusions of dense fluid. (**c**) We model trapping at the large scales relevant to a nationwide analysis, and account for the injection and migration of CO_2. We consider a linear arrangement of injection wells in a deep section of the aquifer [126]. Initially, each well produces a radial CO_2 plume, which grows and eventually interferes with those from neighboring wells, leading to a problem that can be approximated as two-dimensional on a vertical cross section. Trapping occurs primarily after injection, when the CO_2 migrates due to the aquifer slope and the natural head gradient. As the buoyant CO_2 plume rises and spreads away from the well array (dark gray), residual trapping immobilizes blobs of CO_2 in its wake (light gray) [81, 67, 82], and solubility trapping shrinks the plume from below (blue) [47, 138].

2.3 CO₂ migration and pressure buildup both constrain storage capacity

2.3.1 CO₂ trapping and migration-limited capacity

To develop the geologic storage supply curve, we first consider how much CO_2 can be trapped in the pore space of an aquifer. Trapping is essential to prevent upward leakage of the buoyant CO_2 to shallower formations or the surface [21, 129]. While trapping can be analyzed over a wide range of length scales, we consider trapping at the large scale of an entire geologic basin because large volumes of CO_2 will need to be stored to offset emissions [133]. We consider residual trapping, in which blobs of CO_2 become immobilized by capillary forces [81], and solubility trapping, in which CO_2 dissolves into the groundwater [47, 138], since these mechanisms operate over relatively short timescales and provide secure forms of storage (Fig. 2-1a,b). To estimate capacity at the basin-scale, we develop an upscaled model for CO_2 migration and trapping that is simple, but captures the key macroscopic physics of these pore-scale trapping processes. The model also incorporates CO_2 migration due to the aquifer slope and natural head gradient, since migration critically impacts trapping. For example, the tendency of CO_2 to migrate in a long, thin tongue along the caprock reduces the effectiveness of residual trapping, which occurs in the wake of the plume, but increases the effectiveness of solubility trapping, which occurs primarily along the underside of the plume (Fig. 2-1c). Modeling migration is also essential to ensure that the mobile CO_2 becomes fully trapped before traveling to leakage pathways such as outcrops, large faults, or high-permeability zones in the caprock. We make many simplifying assumptions in deriving the trapping model, including homogeneity of the reservoir and vertical-flow equilibrium, and arrive at a nonlinear partial differential equation (PDE), which we solve analytically in some limiting cases, but numerically in general [107] (see Supplementary material, §2.6). While the model is complex enough to permit aquifer-specific capacity estimates based on more than twenty parameters, it is simple enough to be applied quickly to a large number of aquifers.

2.3.2 Pressure dissipation and pressure-limited capacity

Although an aquifer's trapping-based storage capacity may be large, it may be impossible to utilize the entire capacity due to limitations on the injection rate [22, 44]. If the injection
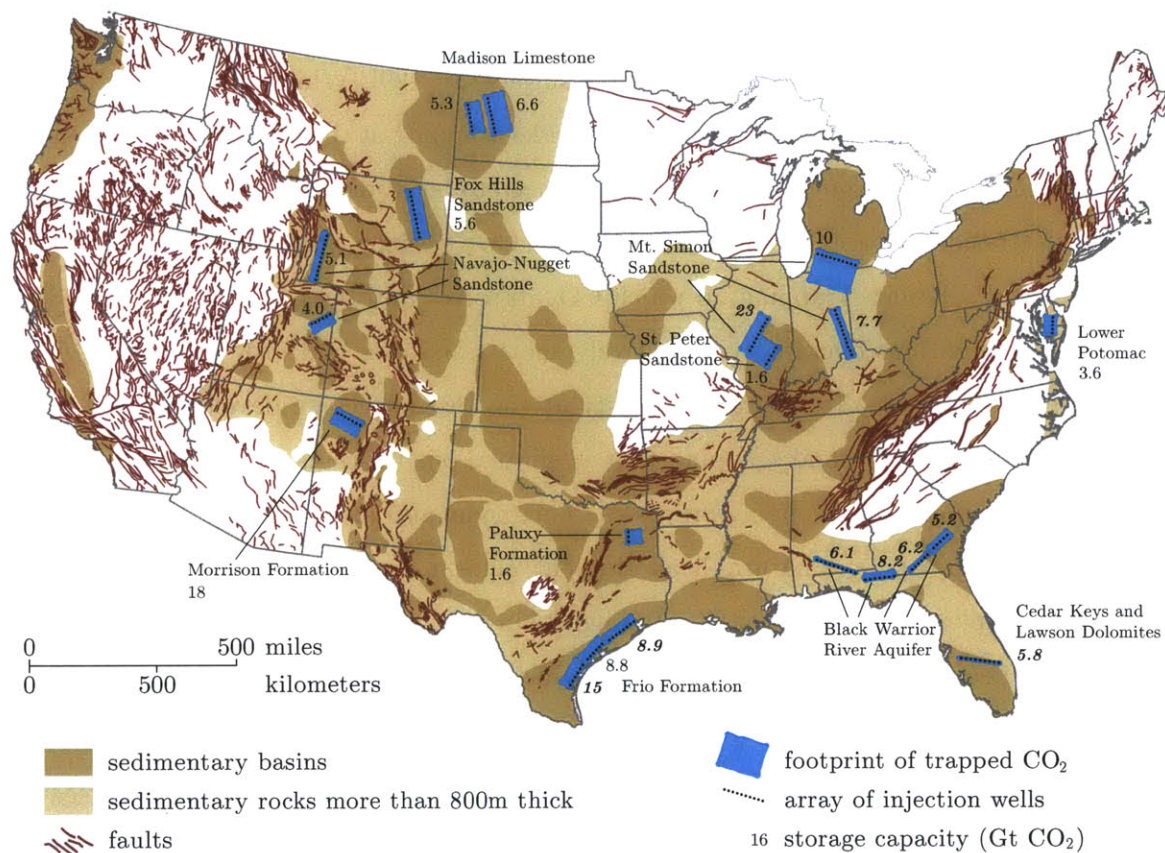
Figure 2-2: We estimate the nationwide storage capacity from 20 arrays of injection wells in 11 aquifers. We select these aquifers because they are large, exhibit few basin-scale faults, and have been relatively well characterized [76]. This map shows the locations of the aquifers and their storage capacities for an injection period of 100 years (capacities for different injection periods are in Table S29). Capacities in boldface italics are constrained by pressure; otherwise, they are constrained by migration. The map also shows the ultimate CO_2 footprints for those capacities, which correspond to the areas infiltrated by migrating, free-phase CO_2 before it becomes completely trapped.

rate is too high, the rise in pressure may create fractures or activate faults. Fracturing and fault activation could induce seismicity, or could create or enhance pathways by which CO_2 could leak [80, Ch.5].

We translate sustainable injection rates into pressure-limited storage capacities (see Supplementary material, §2.6). We calculate the pressure-limited capacity of an aquifer as the total amount of CO_2 that can be injected over a duration T without causing a tensile fracture in the caprock [171]. We neglect multiphase flow effects on the pressure evolution, motivated by the observation that the buoyant CO_2 will spread mostly along the top of the aquifer, and thereby occupy a small fraction of the aquifer volume. Rather than assuming that aquifers are closed [44], we account for pressure dissipation vertically through the geologic basin and interpret geologic cross sections to determine appropriate lateral boundary conditions [22]. As with the trapping model, the pressure model is a PDE that we solve analytically in some limiting cases, but numerically in general (see Supplementary material, §2.6).

While the trapping-based supply curve of an aquifer is independent of time, the pressure-limited supply curve is dynamic, growing approximately as $T^{1/2}$ for short injection durations. This scaling reflects the diffusive character of pressure dissipation in porous media. The trapping-based and pressure-limited supply curves always exhibit a crossover as a function of injection duration, and the complete storage supply curve is the lower of these two curves: it is the pressure-limited supply curve for short injection times, but is the migration-limited supply curve for long injection times (Fig. 2-4a).

2.3.3 US storage capacity

We calculate the storage supply curve for the entire US as the sum of the supply curves for eleven major deep saline aquifers, assuming that CO_2 injection begins simultaneously in each aquifer. The footprints of trapped CO_2 in the aquifers studied illustrate the geographic distribution of storage capacity in the US (Fig. 2-2). We characterize the geology and hydrogeology of each aquifer to determine which portions are suitable for sequestration, considering several criteria that include: (1) the depth must exceed 800 m so that CO_2 is stored efficiently as a high-density, supercritical fluid; (2) the aquifer and caprock must be laterally continuous over long distances; and (3) there must be very few faults that could serve as leakage pathways (see Supplementary material, §2.6). Although abandoned wells

can also serve as leakage pathways [129], data about their locations and integrity is not sufficient to incorporate them into this large-scale study.

Our results for the storage supply of individual aquifers agree well with published estimates. For the portion of the Mt. Simon Sandstone located within the Illinois basin (Region **a**, see Supplementary material, §2.6), the NETL Sequestration Atlas [120] reports a migration-limited capacity of 11–151 Gt, and Birkholzer et al. [22] estimate a pressure-limited capacity of about 13 Gt for an injection time of 50 years. These values compare well with our estimates: our estimate of the migration-limited capacity is 88 Gt, which falls in the center of the range reported by the NETL, and our estimate of the pressure-limited capacity for an injection time of 50 years is 15 Gt, which is about 15% higher than the estimate by Birkholzer et al.

In addition to calculating a baseline storage supply, we perform a sensitivity and uncertainty analysis for each aquifer. While there are many types of uncertainty in storage supply, we consider the impact of statistical uncertainty in the input parameters to estimate the standard deviation in storage supply (see Supplementary material, §2.6).
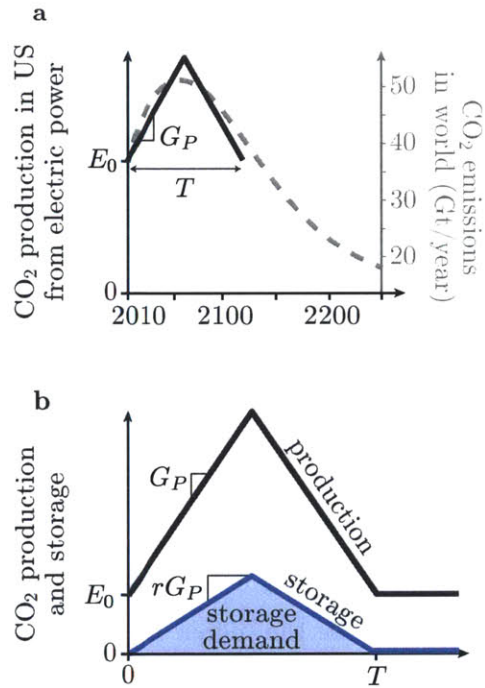
Figure 2-3: (a) Worldwide emission pathways that would stabilize the atmospheric concentration of CO_2 exhibit a characteristic shape: emissions rise to a maximum, decrease, and then level off (dashed gray curve, for stabilization at 750 ppm CO_2) [163]. Our model of CO_2 production pathways in the US (solid black curve) is a simplification of the initial part of that shape. The model is parameterized by two variables: the time required to return to current production rates, T, and the slope of the linear increase, G_p. E_0 is the current production/emission rate. (b) We model the CO_2 storage rate as a fraction, r, of the CO_2 produced from coal- and gas-fired power plants at rates above the current rate. The storage demand is the cumulative CO_2 stored over a storage pathway, which is the total area under the pathway (shaded blue).

2.4 Storage demand vs. supply dictates CCS lifetime

To estimate the demand for CO_2 storage, we first model future CO_2 production from coal-and gas-fired power plants. We assume that the rate of CO_2 production from these plants will increase linearly, reach a maximum, and then decrease linearly with equal and opposite slope until returning to the current rate (Fig. 2-3a). While future CO_2 production trends will likely be complex, we use this simple model because it captures the essential features expected in future trends: an increase in the rate of production as energy demand grows and fossil fuels continue to supply the energy, and then a decrease as low-emissions energy sources begin to replace fossil fuels. We assume that the CO_2 injection rate in each aquifer also follows this ramp-up, ramp-down trend.

This CO_2 production model has two key parameters: the slope of the linear increase, G_p, and the time at which production returns to the current rate, T. Based on data from the electricity sector in the US over the past four decades, we estimate the recent growth rate in production to be $G_p \approx 45$ million tons of CO_2 per year per year (Mt/yr^2) [79]. This rate has slowed recently ($\sim$30 Mt/yr^2 over the past two decades, or $\sim$20 Mt/yr^2 over the past decade), in part due to growth coming more and more from gas-fired plants instead of coal-fired plants. However, we choose the higher historic rate based on our expectation that the deployment of CCS and the abundance of coal will promote the construction of coal-fired plants at rates similar to those in previous decades, and that those plants will be capture-ready. The variable T describes different trajectories of the CO_2 production rate, which we call production pathways in analogy to emission pathways [163].

We define the CO_2 storage rate to be a constant fraction, r, of the surplus CO_2 production rate, or the rate at which CO_2 is produced above the current rate. As a result, storage pathways exhibit the same shape as production pathways: the rate of storage increases linearly, reaches a maximum at the same time production reaches a maximum, and then decreases linearly, returning to zero when production returns to the current rate. The storage demand is the cumulative mass of CO_2 stored over an entire storage pathway: $\frac{r}{4}G_p T^2$ (Fig. 2-3b). This formula indicates that r can also be used to capture uncertainty in the production growth rate, G_p.

The timespan over which CCS can be extended is the time for which the storage supply

curve exceeds the storage demand curve. The time at which the curves intersect corresponds to the longest storage pathway for which there is sufficient storage supply. If the storage demand is all of the surplus CO_2 produced ($r=1$), the demand curve crosses the supply curve at $T=120$ years, with a range of $T=95$ to 165 years (Fig. 2-4b). If the storage demand is one half of CO_2 produced ($r=0.5$), the intersection occurs at $T=190$ years, with a range of $T=145$ to 250 years. If the storage demand is one seventh of the CO_2 production, as proposed in [133], the crossover time is at least 300 years.
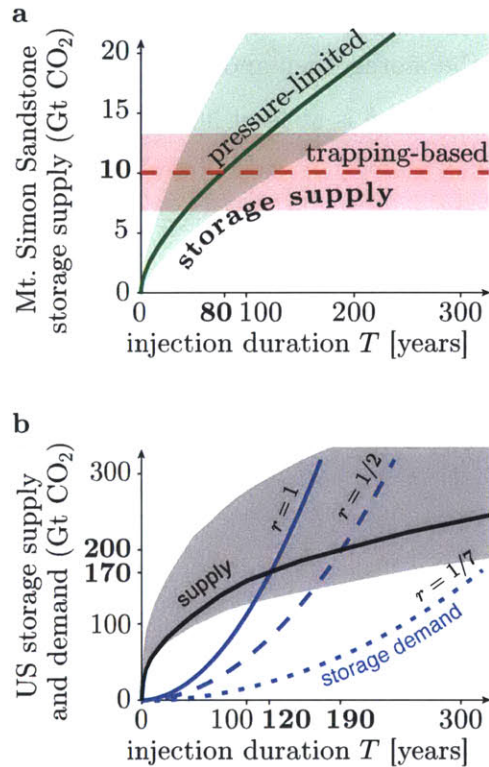
Figure 2-4: (**a**) The storage supply curve of a deep saline aquifer is constrained by both CO_2 trapping and pressure buildup. For short injection times, pressure buildup is the more limiting constraint, and the supply curve increases approximately as the square root of the injection duration, $T^{1/2}$ (see Supplementary material, §2.6). For longer injection times, trapping is the more limiting constraint and the capacity becomes independent of injection time. This is shown for Region **b** of the Mt. Simon Sandstone, where trapping becomes limiting after about 80 years. The shaded areas are uncertainty envelopes based on one standard deviation (see Supplementary material, §2.6). (**b**) The storage supply curve for the entire US (black curve) is the sum of the supply curves of all the aquifers. The uncertainty envelope again represents one standard deviation (shaded gray). The storage demand curves represent storing 100%, 50%, and 15% of all the surplus CO_2 produced at the recent growth rate of 45 Mt/yr^2. The intersection of these curves with the capacity curve marks the maximum time over which CCS can be extended. For a storage demand of all surplus production, the demand curve intersects the supply curve at ∼120 years, indicating that CCS can stabilize atmospheric emissions in the US for at least a century.

2.5 Discussion and conclusions

We have shown that in the US, the storage supply from 11 major deep saline aquifers is sufficient to store large quantities of CO_2 for long times. If the task of stabilizing emissions is divided among several technologies such that the storage demand for CCS is one seventh of the CO_2 produced, CCS can operate for over 300 years. If the storage demand is all the surplus CO_2 produced, CSS can operate for at least a century. This result suggests that geologic storage supply will enable CCS to play a major role among the portfolio of climate-change mitigation options.

Although the storage supply is large, many regulatory and economic factors will play an important role in determining the degree to which this storage supply can be utilized. The successful large-scale deployment of CCS will require, for example, detailed exploration for site selection [58] and comprehensive policy to establish safety and monitoring regulations and drive adoption. Absence of comprehensive policy, in particular, has been identified as the key barrier to the deployment of CCS [2].

Understanding the lifetime of CCS is essential for informing government policy. Since storage supply depends fundamentally on the duration of CCS, policymakers should consider the total time over which CCS will be deployed to identify storage targets or deployment rates that comply with geologic constraints. Alternatively, policymakers should set storage targets recognizing that they can only be achieved for a finite time. Policy for the development of low-emissions energy sources should also consider the lifetime of CCS, which constrains the timescales over which these technologies must be deployed to eventually replace fossil fuels.

2.6 Supplementary material

Here we present our calculation for the growth rate in CO_2 production, describe our mathematical models for CO_2 trapping and pressure build-up, and explain our methodology for applying the models to calculate storage capacity. We also describe the hydrogeologic setting of the aquifers we study and their storage capacities.

2.6.1 Growth rate of CO_2 production

We calculate the growth rate of CO_2 production in the United States based on historical data of electricity production from 1972 to 2008 [79]. From this data, we calculate the coal and gas resources consumed each year by assuming an efficiency of 33% for coal and 44% for gas [157, Tables A2, A8]. We then calculate the CO_2 produced each year by assuming 90 Mt CO_2 per exajoule of coal consumed and 50 Mt CO_2 per exajoule of natural gas consumed [157, Tables A2, A18]. The growth rate of CO_2 production is then the slope of the linear regression of this data: 45 Mt CO_2 per year per year.

2.6.2 CO_2 trapping model

Mathematical model

The volume of CO_2, V_g, that can be trapped in a deep saline aquifer is usually calculated as a fraction of the total available pore volume [10, 24]:

$$V_g = V\phi(1 - S_{wc})\varepsilon, \tag{2.1}$$

where V is the aquifer volume, ϕ is the porosity, S_{wc} is the connate water saturation, and ε is the efficiency factor. We calculate the efficiency factor using a model for how CO_2 migrates through an aquifer and becomes trapped through solubility and capillary trapping [106, 107]. All parameters in the model are defined in Table 2.1. The major assumptions in the model are: (1) the interface between the CO_2 and brine is sharp [17, 77, 128, 67]; (2) capillary pressure effects are negligible; (3) the flow is predominantly horizontal (Dupuit approximation) [17, 168]; (4) CO_2 leakage through the caprock is negligible; (5) the aquifer is homogeneous, isotropic, and incompressible; (6) the fluids are incompressible and their properties are constant; and (7) during the dissolution of CO_2 into brine, the total fluid volume is conserved.

Injection period We divide the model into two parts: the injection period and the post-injection period (Fig. 2-5). During injection, the thickness of the mobile CO_2 plume, h_g, as a function of time, t, and distance along the aquifer, x, is [128, 82, 106, 107]:

$$(1 - S_{wc})\phi\partial_t h_g + \partial_x F_g^i = 0, \tag{2.2}$$
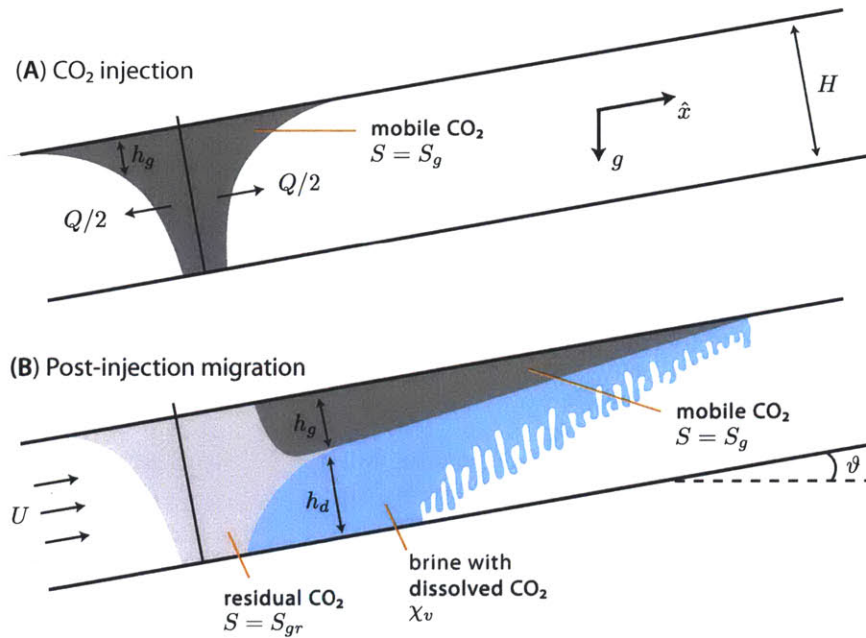
Figure 2-5: (A) During the injection period, CO_2 enters the aquifer at a high flow rate Q, displacing brine to its connate saturation S_{wc}. Since CO_2 is buoyant and less viscous than the brine, the injected CO_2 forms a gravity tongue [128]. No residual trapping occurs since there is little if any imbibition, and solubility trapping is negligible because the injection period is in general much shorter than the time required for dissolution [107]. (B) Once injection stops, the CO_2 plume migrates away from the well array due to buoyancy and the natural hydraulic gradient. Gravity tonguing becomes more severe, with the plume forming a thin wedge along the bottom of the caprock. At the trailing edge of the plume, CO_2 becomes trapped due to capillarity [81]. Along the bottom of the plume, CO_2 dissolves into the brine via convective mixing [47].

Table 2.1: The input parameters used in our models and their symbols. Dimension abbreviations are as follows: L = length, T = time, M = mass, and θ = temperature. Parameters written in Roman are raw input parameters; parameters written in italics are derived parameters.

Parameter [dimensions]	Symbol
Gravitational acceleration [LT^{-2}]	g
Residual CO_2 saturation [–]	S_{gr}
Connate water saturation [–]	S_{wc}
Endpoint relative permeability to CO_2 [–]	k_{gr}^*
Coefficient of CO_2-saturated-brine flux [–]	α
Compressibility [$M^{-1}LT^2$]	c
Undrained Poisson ratio [–]	ν
Geothermal gradient [ΘL^{-1}]	G_T
Surface temperature [Θ]	T_s
Depth to top of aquifer [L]	D
Depth from aquifer to bedrock [L]	B
Net aquifer thickness [L]	H
Length of domain for migration model [L]	L_t
Width of well array [L]	W
Distance from well array to nearest pressure boundary [L]	L_{Pmin}
Distance from well array to farthest pressure boundary [L]	L_{Pmax}
Porosity [–]	ϕ
Caprock slope [–]	ϑ
Darcy velocity [LT^{-1}]	U
Aquifer permeability [L^2]	k_{aq}
Caprock permeability [L^2]	k_c
Salinity [ML^{-3}]	s
Average bulk density of the overburden [ML^{-3}]	$\overline{\rho_o}$
Average density of water in overburden [ML^{-3}]	$\overline{\rho_w}$
Lateral overburden permeability [L^2]	$\overline{k_x}$
Vertical overburden permeability [L^2]	$\overline{k_z}$
CO_2 solubility [–]	χ_v
Brine density [ML^{-3}]	ρ_w
CO_2 density [ML^{-3}]	ρ_g
CO_2-saturated-brine density [ML^{-3}]	ρ_d
Brine viscosity [$ML^{-1}T^{-1}$]	μ_w
CO_2 viscosity [$ML^{-1}T^{-1}$]	μ_g
Fracture pressure [$ML^{-1}T^{-2}$]	P_{frac}

where F_g^i is the flux of CO_2 during injection. Note that the model is one dimensional since we consider injection from a long, line-drive array of wells, as shown in Figure 2. Since the flux of CO_2 due to injection is typically much larger than fluxes due to buoyancy or the natural hydraulic gradient, the flux term is given by

$$F_g^i = \frac{Q}{2W} f, \tag{2.3}$$

where Q/W is the injection rate per unit width of the injection-well array. The fractional flow function f is given by

$$f = \frac{h_g}{h_g + \mathcal{M}(H - h_g)}, \tag{2.4}$$

where H is the thickness of the aquifer and $\mathcal{M}$ is the mobility ratio,

$$\mathcal{M} = \frac{\mu_g}{k_{rg}^* \mu_w}.$$ (2.5)

Post-injection period Once injection stops, the CO_2 plume migrates away from the well array. During migration, it becomes trapped by capillarity at the back of the plume, and by dissolution along the bottom of the plume until the underlying brine is saturated (Fig. 2-5). To determine when the brine is saturated, we model the transport of dissolved CO_2 in the brine in addition to the migration of the free-phase CO_2 plume.

Plume model. The thickness of the plume, h_g, during post-injection is also governed by a one-dimensional hyperbolic equation:

$$(1 - S_{wc})\phi \widetilde{R} \partial_t h_g + \partial_x \left(F_g^p \right) = \mathcal{L},$$ (2.6)

where F_g^p is the CO_2 flux during post-injection. $\widetilde{R}$ is a conditional coefficient that accounts for residual trapping:

$$\widetilde{R} = \begin{cases} 1 & \text{if } \partial_t h_g > -q_d/\phi, \\ 1 - \Gamma & \text{otherwise,} \end{cases}$$ (2.7)

where Γ is the capillary trapping coefficient, which quantifies the fraction of pore space that will be occupied by residual CO_2:

$$\Gamma = \frac{S_{gr}}{1 - S_{wc}}.$$ (2.8)

q_d is the volumetric flux of CO_2 leaving the plume due to dissolution:

$$q_d = \frac{\alpha \chi_v \phi (\rho_d - \rho_w) g k_{aq}}{\mu_w},$$ (2.9)

where α is a constant roughly equal to 0.01 [135], $\Delta \rho_d$ is the density difference between brine and CO_2-saturated brine, and χ_v is the solubility of CO_2 in brine, expressed as the volume of free-phase CO_2 that can be dissolved per unit volume of brine saturated with CO_2.

During post-injection, the flux is given by:

$$F_g^p = UHf + \frac{(\rho_w - \rho_g)gk_{aq}k_{gr}^* \sin\vartheta}{\mu_w}(1-f)h_g, \qquad (2.10)$$

where U is the Darcy velocity of the natural groundwater flow and ϑ is the slope of the caprock. The first term expresses the flux of CO_2 due to the natural hydraulic gradient and the second term expresses the flux due to upslope migration.

The right-hand side of the post-injection model (Eq. 2.6) is a loss term ($\mathcal{L} < 0$) that accounts for dissolution:

$$\mathcal{L} = \begin{cases} -\widetilde{R}(1 - S_{wc})q_d & \text{if } h_d < H - h_g, \\ 0 & \text{otherwise,} \end{cases}$$

where h_d is the effective height of the water column under the plume that is saturated with CO_2. Substituting each of these expressions into Eq. 2.6 yields the complete CO_2 trapping model:

$$(1 - S_{wc})\widetilde{R}\partial_t h_g + \partial_x \left(UHf + \frac{(\rho_w - \rho_g)gk_{aq}k_{gr}^* \sin\vartheta}{\mu_w}(1-f)h_g \right) = \mathcal{L}. \qquad (2.11)$$

CO_2-saturated-brine model. The model for the migration of CO_2-saturated brine tracks the thickness of the region of brine below the plume that is saturated with CO_2, h_d:

$$\chi_v \phi \partial_t h_d + \chi_v \partial_x F_d^p = -\mathcal{L} - \chi_v S_{wc}\phi\partial_t h_g, \qquad (2.12)$$

where F_d^p is the flux of CO_2-saturated brine. The thickness of the CO_2-saturated region grows as a result of dissolution via the $-\mathcal{L}$ term (recall that $\mathcal{L} < 0$), which previously appeared as a loss term in the CO_2 model.

The flux of CO_2-saturated brine F_d^p may occur due to a natural hydraulic gradient or the slope of the aquifer:

$$F_d^p = UH(1-f) - \frac{(\rho_g - \rho_w)gk_{aq}k_{gr}^* \sin\vartheta}{\mu_g}(1-f)h_g. \qquad (2.13)$$

We neglect fluxes that may be caused by the density difference between the brine and CO_2-saturated brine. We also neglect diffusion and dispersion.

Non-dimensional form of the equations. We choose the following non-dimensional variables:

$$\eta_g = h_g/H, \quad \eta_d = h_d/H, \quad \tau = t/T_c, \quad \xi = x/L_c, \tag{2.14}$$

where $L_c = QT_i/2W(1 - S_{wc})\phi H$, with $T_c = T_i$ being the injection time. With these variables, the injection model (Eq. 2.2) becomes:

$$\partial_\tau \eta_g + \frac{1}{2}\partial_\xi f = 0. \tag{2.15}$$

The model for the CO_2 migration during post-injection (Eq.2.11) becomes:

$$\widetilde{R}'\partial_\tau \eta_g + N_f \partial_\xi f + N_s \partial_\xi \left[(1 - f)\eta_g\right] = -\widetilde{R}'N_d, \tag{2.16}$$

and the model for the CO_2-saturated brine (Eq. 2.12) becomes:

$$\widetilde{R}'\partial_\tau \eta_d + (1 - S_{wc})N_f \partial_\xi f_d - (1 - S_{wc})N_s \partial_\xi (f_d \eta_g) = \widetilde{R}'\frac{N_d}{\Gamma_d} - S_{wc}\partial_\tau \eta_g, \tag{2.17}$$

where:

$$\widetilde{R}' = \begin{cases} 1 & \text{if } \partial_\tau \eta_g > -N_d, \\ 1 - \Gamma & \text{otherwise.} \end{cases}$$

and

$$f(\eta_g) = \frac{\mathcal{M}\eta_g}{\mathcal{M}\eta_g + (1 - \eta_g)}, \quad f_d(\eta_g, \eta_d) = \frac{\eta_d}{\mathcal{M}\eta_g + (1 - \eta_g)}.$$

The coefficients in the equations are the flow number, N_f, and the slope number, N_s:

$$N_f = \frac{T_c}{T_i}\frac{2UH}{Q} \quad \text{and} \quad N_s = \frac{T_c}{L_c}\frac{(\rho_w - \rho_g)gk_{aq}k_{gr}^*}{(1 - S_{wc})\phi\mu_g}, \tag{2.18}$$

which express the strength of the natural groundwater flow and the aquifer slope in driving plume migration. The dissolution number, N_d, expresses the strength of dissolution:

$$N_d = \begin{cases} \alpha\chi_v \dfrac{\Delta\rho_d gk_{aq}k_{gr}^* T_c}{H\phi\mu_g} & \text{if } \eta(\xi, \tau) > 0 \text{ and } \eta_d(\xi, \tau) < (1 - \eta(\xi, \tau)), \\ 0 & \text{otherwise.} \end{cases} \tag{2.19}$$

Migration-limited capacity

In an aquifer, a given volume of injected CO_2 will migrate a particular distance before becoming completely trapped by capillarity and solubility [67, 82, 106, 107]. There is a particular injection volume for which the CO_2 plume will just reach the boundary of the aquifer. We define this volume to be the migration-limited storage capacity. Rearranging the expression for non-dimensional distance ξ (Eq. 2.14), we obtain a formula for the injected volume $V_i = QT_i$:

$$V_i = xWH\phi(1 - S_{wc})\frac{2}{\xi}.$$

By setting x to the total length of an aquifer, L_T, ξ to the dimensionless extent of the plume when it is fully trapped, ξ_T, we ensure that this injected volume will just fit in the aquifer. Since the model is one dimensional, we measure the length of an aquifer, L_T, in the direction parallel to migration. We calculate the dimensionless extent of the trapped plume, ξ_T, using the trapping model. To convert volume to mass of CO_2, we multiply by the density of CO_2 in the aquifer, and obtain the final expression for the storage capacity, C_t:

$$C_t = \rho_g L_T W H \phi (1 - S_{wc}) \frac{2}{\xi_T}. \tag{2.20}$$

The expression has the same form as equations commonly used in the literature (Eq. 2.1), but the efficiency factor $\varepsilon = 2/\xi_T$ can now be calculated explicitly.

To calculate the efficiency factor, we first solve the equation for the injection plume (Eq. 2.15) analytically using the method of characteristics [128, 106]. We use the solution as the initial condition for the equations governing post-injection migration (Eq. 2.16–2.17). While these equations can be solved semi-analytically in some limiting cases, we in general solve them numerically using a finite volume method with linear reconstructions and a van Leer limiter, and forward-Euler time stepping [100].

2.6.3 Pressure model

Mathematical model

We have previously derived a one-dimensional version of our pressure model [147]. Here, we extend the model to two dimensions. All variables in the model are defined in Table 2.1. The major assumptions in the model are: (1) the vertical stress is lithostatic; (2) the over-

32

burden is the only source of horizontal stress (the bilateral constraint [171, p.282]); (3) the aquifer, the overburden, and the underburden are homogeneous; (4) the initial pressure is hydrostatic; (5) the aquifer properties and fluid properties are constant; (6) the pressure distribution along the line-drive array of wells is uniform; and (7) the compressibility of the CO_2 is negligible. This final assumption will cause the model to overestimate the pressure rise at the well array, and will therefore lead to conservative estimates of storage capacity.

The assumptions cause errors in the calculated pressure. Neglecting the compressibility of CO_2 will cause the model to overestimate the pressure rise at the well array, and will therefore lead to conservative estimates of storage capacity. Assuming uniform pressure along the well array can lead to an underestimation of the pressure buildup at the wells themselves, and could cause us to overestimate the storage capacity. The validity of this assumption can be estimated by comparing the timescale of pressure communication between wells in the array with the injection time: if the pressure field equilibrates along the well array quickly relative to the injection time, the assumption will be good and the error will be small. With this is mind, we estimate the pressure equilibration time and compare it to an injection time of 100 years, which is the most important time horizon in our study. We assume a permeability of k=100 mD, a brine viscosity of μ=1 mPa s, and an aquifer compressibility of c=0.1 GPa^{-1}, based on aquifer data in Table 2.30. We find that for a well spacing of l=10 km, the timescale of pressure equilibration is roughly $l^2/(k/c\mu) \approx 3$ years, which is much smaller than the 100 year time horizon. Since the well spacing is reasonable and the equilibration occurs relatively quickly, the assumption of uniform pressure along the array likely causes minimal error.

The geologic setting of our system is the same as the setting of the trapping model, but now includes the entire thickness of the basin that contains the target aquifer, as shown in Figure 2-7. In this system, the model for pressure, p, as a function of spatial coordinates x and z and time, t, is:

$$c\partial_t p + \partial_x u_x + \partial_z u_z = I(z), \tag{2.21}$$

where c is the compressibility, I is a function that represents injection into the aquifer, and u_x and u_z are the Darcy velocities in the x and z directions, respectively. Since we neglect

the compressibility of CO_2, these velocities are given by Darcy's law for single-phase flow:

$$u_x = -\frac{k_x(z)}{\mu_w}\partial_x p, \quad u_z = -\frac{k_z(z)}{\mu_w}\left(\partial_z p - \rho_w g\right), \tag{2.22}$$

where k_x and k_z are given by:

$$k_x(z) = \begin{cases} k_{aq} & D \leq z < D + H, \\ \overline{k_x} = k_{aq}/2 & \text{otherwise,} \end{cases}$$

$$k_z(z) = \begin{cases} k_{aq} & D \leq z < D + H, \\ \overline{k_z} = 2k_{cap} & \text{otherwise.} \end{cases}$$

These expressions are conditional because we assign different properties to the aquifer and the regions outside of the aquifer. Within the aquifer, the intrinsic permeability is k_{aq}. Above and below the aquifer, we set the permeability to average values ($\overline{k_x}$ and $\overline{k_z}$) derived from the aquifer permeability and the caprock permeability, k_{cap}, as shown in Figure 2-8. The source term I is conditional since it accounts for a ramping-up of the injection rate, a ramping-down of the injection rate, and then no injection, as shown in Figure 2-6:

$$I(z,t) = \begin{cases} \delta(x)\mathcal{U}(z; D, D+H)\dfrac{2Q_{max}}{WH}\dfrac{t}{T} & 0 \leq t < T/2, \\[2ex] \delta(x)\mathcal{U}(z; D, D+H)\dfrac{2Q_{max}}{WH}\left(1 - \dfrac{t}{T}\right) & T/2 \leq t < T, \\[2ex] 0 & T \leq t, \end{cases}$$

where T_i is the injection time (Figure from main paper) and $\mathcal{U}$ is the rectangular function, which allows injection only within the aquifer:

$$\mathcal{U}(z) = \begin{cases} 1 & D \leq z < D + H, \\ 0 & \text{otherwise.} \end{cases}$$

With these expressions, the model for pressure becomes:

$$c\partial_t p - \frac{k_x(z)}{\mu_w}\partial_{xx}p - \partial_z\left(\frac{k_z(z)}{\mu_w}\left(\partial_z p - \rho_w g\right)\right) = I(z,t) \tag{2.23}$$

34
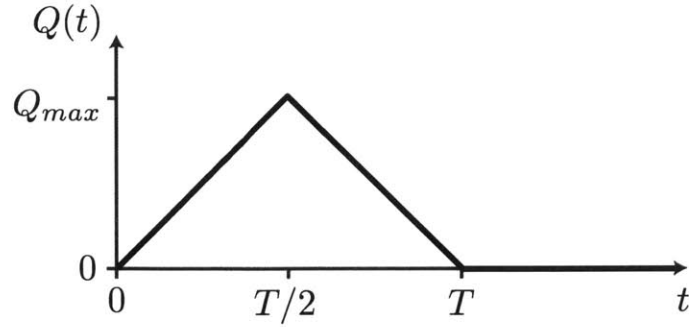
Figure 2-6: In our model, the injection rate of CO_2 increases linearly to a maximum, Q_{max}, decreases linearly to zero, and then remains at zero.
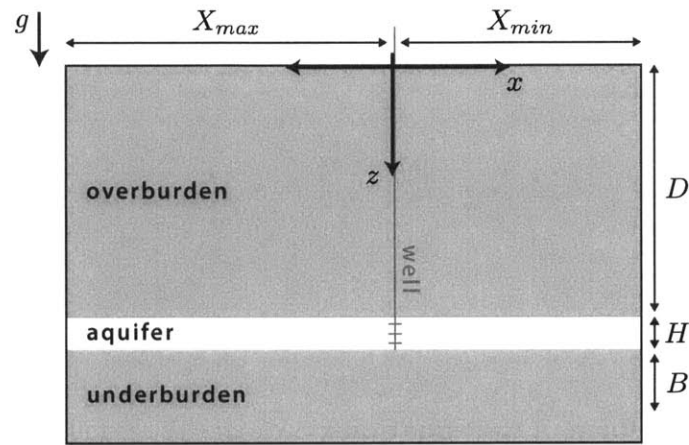
Figure 2-7: Since we consider injection from a line-drive array of wells, our pressure model is two dimensional: it captures behavior in a plane perpendicular to the line-drive array that extends from the ground surface to the basement. We position the center of the coordinate system where the line-drive array intersects the surface.

$$X_{min} < x < X_{max}, \qquad 0 < z < D + H + B, \quad t > 0,$$

where X_{min} is the distance to the nearest lateral boundary and X_{max} is the distance to the farthest lateral boundary. In practice, these boundaries correspond to the edges of the pressure-model domain (see Section 2.6.4).

The initial condition is hydrostatic pressure. The boundary condition at the top of the basin is a constant-pressure condition, and the boundary condition at the bottom of the basin is a no-flow condition. The boundary conditions at the sides of the basin may be either no-flow conditions or constant-pressure conditions depending on the geology. We assume that the same boundary condition applies over an entire side of the basin.
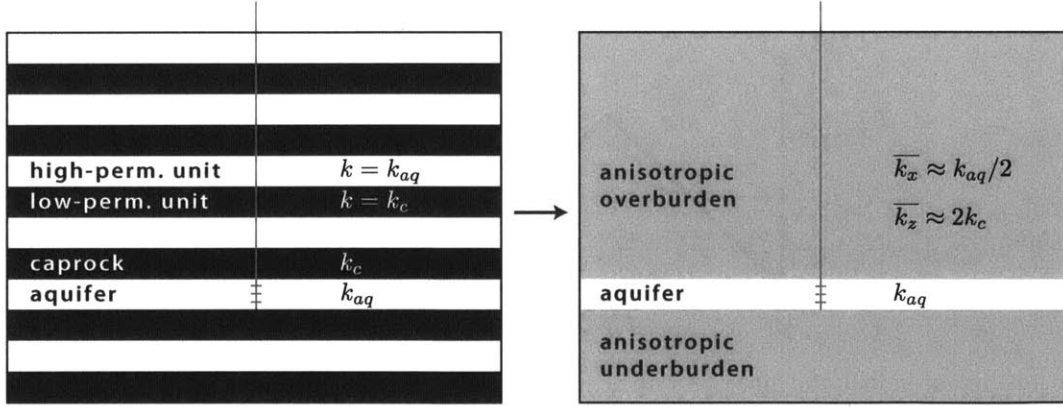
Figure 2-8: We model the entire thickness of a basin by assuming that it consists of multiple layers of high-permeability and low-permeability rock. We assume that each layer of high-permeability rock has the same permeability as the aquifer, and that each layer of low-permeability rock has the same permeability as the caprock. Under these assumptions, we average the permeabilities of all the layers above and below the aquifer to get homogeneous, but anisotropic permeabilities of the overburden and underburden.

Non-dimensional form of the equations. We choose the following non-dimensional variables:

$$\widetilde{p} = \frac{p - (p_o + \overline{\rho_w}gz)}{\overline{P}}, \quad \tau = \frac{t}{T_i}, \quad \xi = \frac{x}{L}, \quad \zeta = \frac{z}{H}. \tag{2.24}$$

We define the characteristic pressure and the characteristic length in the x-direction as:

$$\overline{P} = \frac{2Q_{max}}{HW}\sqrt{\frac{\mu_w T_i}{k_{aq}c}}, \qquad L = \sqrt{\frac{k_{aq}T_i}{\mu_w c}}.$$

The non-dimensional form of the pressure model is:

$$\partial_\tau \widetilde{p} - \lambda_\xi(\zeta)\partial_{\xi\xi}\widetilde{p} - \partial_\zeta\left(\lambda(\zeta)\partial_\zeta\widetilde{p}\right) = \widetilde{I}(\zeta), \tag{2.25}$$

$$\Xi_{min} < \xi < \Xi_{max}, \qquad 0 < \zeta < 1 + \Omega + \beta, \quad \tau > 0,$$

where the dimensionless lengths in the basin are given by:

$$\Xi_{min} = \frac{X_{min}}{L}, \quad \Xi_{max} = \frac{X_{max}}{L}, \quad \Omega = \frac{D}{H}, \quad \beta = \frac{B}{H}.$$

λ_ξ and λ_ζ are dimensionless diffusion coefficients given by:

$$\lambda_\xi(\zeta) = \begin{cases} 1 & \Omega \le \zeta < \Omega + 1, \\ 1/2 & \text{otherwise,} \end{cases}$$

and

$$\lambda_\zeta(\zeta) = \begin{cases} \dfrac{k_{aq}T_i}{\mu_w c H^2} & \Omega \le \zeta < \Omega + 1, \\ \dfrac{2k_{cap}T_i}{\mu_w c H^2} & \text{otherwise.} \end{cases}$$

The dimensionless injection function is:

$$\widetilde{I}(\zeta, \tau) = \begin{cases} \delta(\xi)\mathcal{U}(\zeta; \Omega, \Omega + 1)\tau & 0 \le \tau < 1/2, \\ \delta(\xi)\mathcal{U}(\zeta; \Omega, \Omega + 1)(1 - \tau) & 1/2 \le \tau < 1, \\ 0 & 1 \le \tau. \end{cases}$$

Pressure-limited capacity

For a given injection period T, a particular injection scenario characterized by Q_{max} will lead to a particular maximum pressure in the aquifer. There is a value of Q_{max} for which the maximum pressure will reach the fracture pressure of the aquifer. We define the volume injected in this scenario to be the pressure-limited storage capacity. In our ramp-up, ramp-down injection scenario, the volume injected is

$$V_p = \frac{1}{2}Q_{max}T. \tag{2.26}$$

The maximum injection rate can be obtained by rearranging the expression for the non-dimensional pressure, $\widetilde{p}$ (Eq. 2.24):

$$Q_{max} = HW\sqrt{\frac{k_{aq}c}{\mu_w T}}\frac{p - (p_o + \overline{\rho_w}gz)}{2\widetilde{p}}.$$

Setting the pressure to the fracture pressure, $p = P_{frac}$, and the dimensionless pressure to the maximum dimensionless pressure, $\widetilde{p} = \widetilde{p}_{max}$, yields the maximum injection rate for which the pressure will just reach the fracture pressure. Substituting into the expression

37

for injection volume and multiplying by the density of CO_2 yields the storage capacity in mass of CO_2, C_p:

$$C_p = \rho_g H W \sqrt{\frac{k_{aq} c T}{\mu_w} \frac{P_{frac} - (p_o + \overline{\rho_w} g D)}{4 \widetilde{p}_{max}}}. \tag{2.27}$$

We determine the maximum dimensionless pressure $\widetilde{p}_{max}$ by solving the pressure model (Eq. 2.25) numerically. We use a second-order finite-volume method in space with a Crank-Nicolson time discretization [100].

We define the fracture pressure, P_{frac}, to be the pressure required to create a tensile fracture in an aquifer [55, 171]. Ignoring the cohesive strength of the aquifer rock, a tensile fracture occurs when the pore pressure equals the least principal stress. When this stress is vertical, we calculate it to be the weight of the overburden:

$$P_{frac} = \overline{\rho_o} g D + p_o, \tag{2.28}$$

where $\overline{\rho_o}$ is the average bulk density of the overburden, which we approximate to be 2300 kg/m^3 [149]. When it is horizontal, we approximate it using the bilateral constraint [171, p.282]. This constraint provides a relationship between the effective horizontal stress, σ'_h, and the effective vertical stress, σ'_v:

$$\sigma'_h = \frac{\nu}{1 - \nu} \sigma'_v,$$

$$\sigma_h - P_p = \frac{\nu}{1 - \nu} (\sigma_v - P_p),$$

where σ_h is the principle horizontal stress, σ_v is the vertical principle stress, ν is the Poisson ratio, and P_p is the pore pressure. Assuming that the pore pressure in a basin is hydrostatic, we solve this equation for the initial horizontal stress in an aquifer at depth D. We use this as an estimate of the pressure required to create a vertical fracture in rock with negligible cohesive strength:

$$P_{frac} = \frac{\nu}{1 - \nu} (\overline{\rho_o} g D - \overline{\rho_w} g D) + p_o + \overline{\rho_w} g D, \tag{2.29}$$

We determine whether the least principal stress is horizontal or vertical by using a stress map for the United States [173].

2.6.4 Methodology for application of the models

We calculate the storage capacity of eleven deep saline aquifers in the conterminous United States. We select these aquifers on the basis of their (1) size, (2) depth, and (3) structural integrity, and (4) on the availability of data . We select the largest aquifers because our model applies at large lateral length scales and because large aquifers will contribute the most strongly to the nationwide storage capacity. We select aquifers located at depths greater than 800 m to ensure that CO_2 will be stored efficiently as a high-density supercritical fluid. We study aquifers with as few major faults as possible to help reduce the possibility of leakage. While there are likely many deep saline aquifers that meet these criteria, we further restrict our study to those aquifers that have been well characterized and for which the data is publicly available.

Aquifer boundaries. For each aquifer, we use the four criteria stated above—sufficient size, depth, structural integrity, and data—to determine which parts of it are suitable for sequestration. In general, these criteria may be evaluated at a range of length scales. For example, faults and pinchouts in the caprock may occur at scales ranging from the submeter scale or less to the regional scale. Since we calculate storage capacity at the basin scale, we evaluate these criteria at the basin scale and assume that small-scale variations will have small impacts on the storage capacity. When one of these criteria is not met at the basin scale, we exclude the appropriate region from our analysis by setting a boundary (Fig. 2-9).

Some types of boundaries impose boundary conditions in the pressure model (Fig. 2-9). We set constant pressure boundaries at outcrops. We set no-flow boundaries where the reservoir pinches out between two confining layers, changes to low-permeability rock ($k \leq 10$ millidarcy (mD), 1 darcy=10^{-12} m^2), or becomes cut by basin-scale faults. While faults may be either conductive or sealing, we set them to be no-flow boundaries so that the calculation of pressure-limited capacity is conservative.

Model domains. Within the boundaries of an aquifer, we determine the area over which to apply the trapping model. This region defines the maximum allowable extent of the plume when fully trapped, L_T, and the width of the well array, W. We select model domains in which the aquifer properties exhibit sufficient uniformity for the trapping model
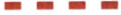
Criterion for suitable aquifers	Feature marked	Boundary condition in pressure model	Symbol
Sufficient data	Limit of available data	no flow	———
Aquifer continuity	Reservoir pinchouts	no flow	———
	Low-perm. regions	no flow	- - - -
Low potential of leakage	Faults	no flow	———
	Outcrops	constant pressure	———
	Caprock pinchouts	*not a pressure boundary*	———
	High-perm. region in caprock	*not a pressure boundary*	- - - -
Sufficient depth	800m - depth contour	*not a pressure boundary*	⊥⊥

Figure 2-9: We exclude portions of an aquifer from our analysis if they do not meet the four criteria in this table. In our geologic maps, we delineate these regions by drawing boundaries. Some of these boundaries impose boundary conditions in the pressure model.

to capture basin-scale behavior of the injected CO_2. In addition, we orient the model domains according to the dominant transport direction. If the transport directions are not co-linear, we compare N_s and N_f to determine the dominant process (Eq. 2.18). We evaluate N_s and N_f using values of their parameters averaged over the entire area within the reservoir boundaries. However, if the depth and isopotential contours are very complicated within some part of that area such that transport from ground water flow or up-slope migration can not be approximated as one-dimensional, we exclude that area from our averaging.

Another constraint on the size of a model domain comes from an assumption in the trapping model: since the model assumes that all behavior perpendicular to the well-array has a negligible or higher-order effect on migration, it rigorously applies to domains in which the ratio of the length parallel to the intended well array to the length parallel to transport is large. While we usually choose domains with an aspect ratio of two or larger, in some cases we use domains that have an aspect ratio closer to one. In these cases, the trapping model predicts a migration distance that is longer than the real migration distance of a given volume of CO_2, since the spread of the real plume parallel to the well array would be important.

In addition to setting the trapping model domain, we set the area over which to apply the pressure model. Since we use the same well array in the pressure model as we do in the trapping model, the widths of these two domains are the same. However, their lengths are often different because not all of the aquifer boundaries correspond to boundary conditions in the pressure model (Fig. 2-9). This is because regions are not suitable for storing CO_2 may be suitable for "storing" some of the pressure perturbation due to injection. The distances from the well array to the edges of the pressure model domain define the distances to the lateral boundaries in the pressure model, X_{min} and X_{max} (Eq. 2.23).

As with the trapping model domains, the pressure-model domains should have large aspect ratios for the pressure model to be strictly valid. However, this is difficult to accomplish in practice, and many of the pressure model domains in this study have aspect ratios near one or less. In these cases, pressure diffusion in the direction parallel to the well array becomes important, resulting in a smaller overpressure at the well array for a given injection scenario compared to the model predictions. Since the model overestimates the pressure rise in these cases, it underestimates the pressure-limited capacity (Eq. 2.27).

Model parameters. Within a model domain, we set the parameters in the models in three ways (Table 2.1): by using aquifer data directly, by using aquifer data to calculate the parameters, or by estimation. We list the method we use and the value of each parameter in the section describing each aquifer (*e.g.* Table 2.2).

We use aquifer data directly to set parameters such as the aquifer depth, thickness, porosity, salinity, and permeability. Since the data often exhibit large uncertainty and variability at the basin scale, we choose representative values. We choose these values to make the storage capacity calculations conservative. For example, if an aquifer exhibits a wide range of porosities, we choose a low value in the range, which will result in a lower trapping-limited storage capacity.

When aquifer data cannot be used directly, we use it to calculate the required parameters. We calculate CO_2 viscosity and density as functions of temperature and pressure [25]. We calculate the temperature in an aquifer, T_{aq}, using the surface temperature, T_s, and the geothermal gradient, G. We calculate the fluid pressure assuming a hydrostatic gradient. Brine density, brine viscosity, and the solubility of CO_2 in brine are functions of salinity in addition to temperature and pressure. While aquifer brines may contain a wide variety of salts, we treat them as consisting of only water and sodium chloride (NaCl), which is by far the dominant salt in nearly every deep saline aquifer [85]. We calculate the density and viscosity of brine using correlations based on temperature, pressure, and concentration of sodium chloride [16]. We determine the solubility of CO_2 in brine from published experimental data for salinities up four molal [42] and from a correlation for higher salinities [46].

In the trapping model, the relevant measure of CO_2 solubility is the volume of free-phase CO_2 that can be dissolved per unit volume of brine saturated with CO_2. This parameter, χ_v (Eq. 2.9), can be calculated from the solubility in terms of mass fraction, χ_m:

$$\chi_v = \frac{\rho_d}{\rho_g}\chi_m.$$

To calculate the density of CO_2-saturated brine, ρ_d, we use the following formula [8, 60]:

$$\rho_d = \frac{\rho_w}{1 - \chi_m(1 - V_\phi \rho_w^*/M_g)},$$

where M_g is the molar mass of CO_2, ρ_w^* is the density of pure water at aquifer conditions, and

V_ϕ is the apparent molar volume of CO_2 in the brine, given by the following correlation [60]:

$$V_\phi = 37.51 \times 10^{-6} - (9.585 \times 10^{-8})T_{aq} + (8.740 \times 10^{-10})T_{aq}^2 - (5.044 \times 10^{-13})T_{aq}^3,$$

where T_{aq} is in degrees Celsius and V_ϕ is in m^3/mol.

When there is insufficient data to determine the required parameters, we estimate them. Since little or no data was available for the compressibility of the aquifers and caprocks in this study, we set the average compressibility for every basin to $c = 10^{-10}$ Pa^{-1}, as has been done in other basin-scale studies [170]. We do not pursue a more rigorous approach because published compressibility data for many types of aquifers and caprocks are equal to within the variability and uncertainty of the data, and also similar to the compressibility of water at the pressure and temperature conditions of deep aquifers. For example, published values for sandstones and limestones generally range from 1×10^{-11} to 1×10^{-10} Pa^{-1} [160, 26], while published values for low-porosity shales and mudstones ($\phi < 0.2$) generally range from 1×10^{-11} to 1×10^{-9} Pa^{-1} [89, 32, 50, 115]. Similarly, we set the Poisson ratio of the aquifers or caprocks to 0.3 in every basin, which is a value characteristic of many sedimentary rocks [160].

When data on caprock permeability is unavailable, we estimate it to be 0.01 mD [124, 153, 37]. While rocks deeper than about 3 km can exhibit much lower permeability [122], we use this value for all confining units under the assumption that small fractures that are likely widespread at the basin scale will produce effective permeabilities of this order or higher.

Since aquifer-specific data on the multiphase-flow characteristics of CO_2 and brine was also unavailable, we estimate the connate water saturation, residual CO_2 saturation, and the endpoint relative permeability to CO_2. Based on published data, we take $S_{wc} = 0.4$, $S_{gr} = 0.3$, and $k_{gr}^* = 0.6$ [18]. These values correspond to $\Gamma = 0.5$.

2.6.5 Aquifer data

Mt. Simon Sandstone

The Mt. Simon Sandstone is widespread in the Midwestern United States, as shown in Figure 2-10. It is a transgressive sandstone that consists dominantly of quartz arenite [162, 169]. Near its base, the formation tends to be conglomeratic with igneous pebbles [164, 76].

43

a. depth to top of the aquifer

b. thickness
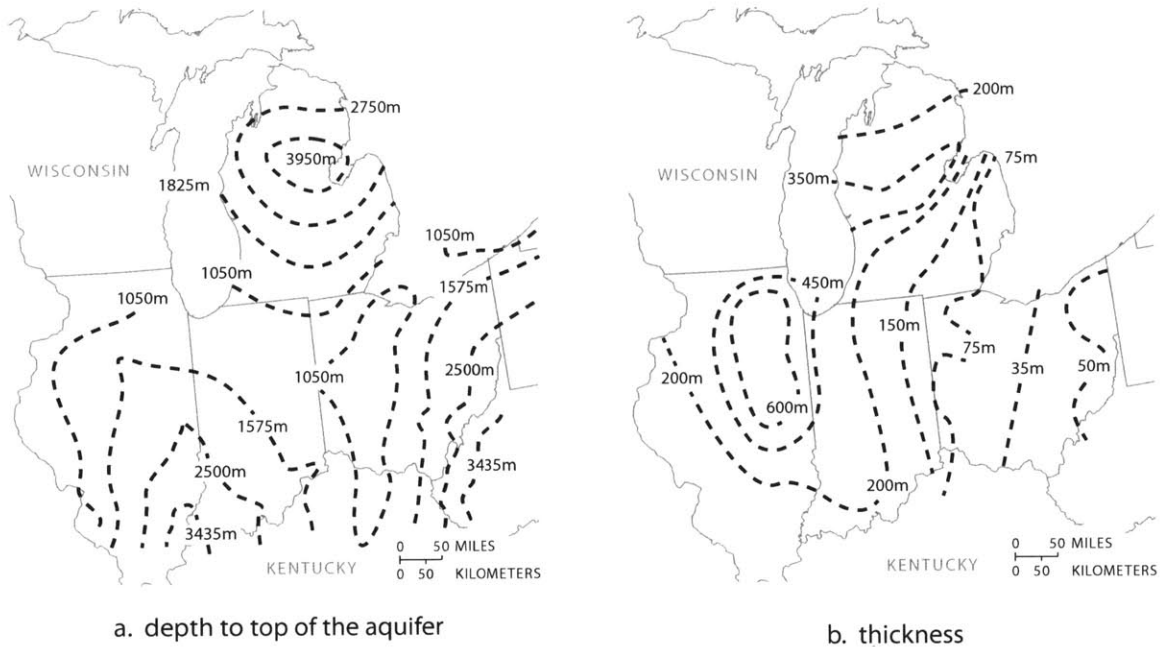
Figure 2-10: The Mt. Simon Sandstone is widespread in the Midwest. It is deepest and thickest in the centers of the Illinois, Michigan, and Appalachian Basins. (a) Modified from [162, Fig.A2-3],[74, Map c1mtsimong], and [15, Fig.3]. (b) Modified from [162, Fig.A2-2],[99, Fig.2], and [15, Fig.4].

Lenses of sandy to silty shale are interbedded in the lower part of the formation in Illinois, and in the upper part of the formation throughout the Midwest [169, p.B13].

The Mt. Simon Sandstone is overlain by the Eau Claire Formation, which is composed of silty dolomites, dolomitic sandstones, and shale [162]. This formation has been identified as a regional confining unit by a number of authors [102, 169, 108]. The Mt. Simon unconformably overlies Precambrian igneous and metamorphic rocks, which we take as an aquiclude [164, 76].

In this study, we model sequestration in deep parts of the formation that lie in the Michigan Basin, Illinois Basin, and the Indiana-Ohio Platform. Within each region, we identify a single model domain, as shown in Figure 2-11. The data for each domain are shown in Tables 2.2, 2.3, and 2.4.
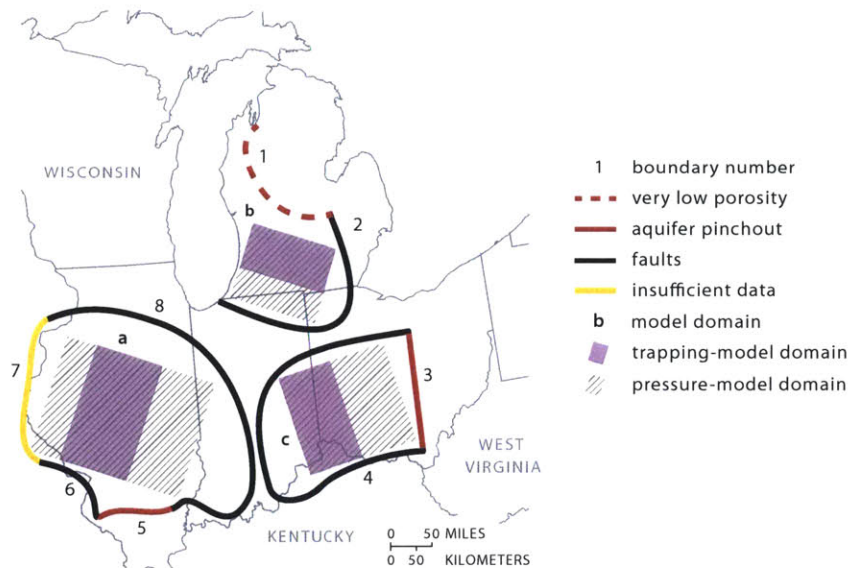
Figure 2-11: We divide the Mt. Simon Sandstone into regions a, b, and c using eight boundaries. Boundary 1 corresponds to where the porosity becomes very low due to diagenesis ($\phi < 0.1$) [15]. Boundary 3 corresponds to where the Mt. Simon Sandstone pinches out into thinner sandstones [99, Fig.2], and Boundary 5 corresponds to where it pinches out between the Precambrian basement and the caprock [99, Fig.2]. Boundary 7 corresponds to the edge of available depth and thickness maps [74, Map c1mtsimonag]. Boundaries 2, 4, 6 and 8 correspond to basin-scale faults[162, 86]. Within each region, we set the extent and orientation of the model domains based on the aquifer's topography since upslope migration is the dominant transport mechanism.

45

Table 2.2: Parameters for Region a of the Mt. Simon Sandstone.

Parameter	Symbol	Value	Data Source	Reference
Residual CO_2 saturation	S_{rg}	0.3	estimated	[18, 130]
Connate water saturation	S_{wc}	0.4	estimated	[18, 130]
Endpoint relative permeability to CO_2	k_{rg}^*	0.6	estimated	[18, 130]
Coefficient of CO_2-saturated-brine flux	α	0.01	estimated	[87, 138]
Compressibility (GPa^{-1})	c	0.1	estimated	[160, Table C1]
Undrained Poisson ratio	ν	0.3	estimated	[160, Table C1]
Geothermal gradient (°C/km)	G_T	20	aquifer data	[91, 119]
Surface temperature (°C)	T_s	10	aquifer data	[3]
Depth to top of aquifer (m)	D	2000	aquifer data	[74, Map c1mtsimong]
Depth from aquifer to bedrock (m)	B	0	aquifer data	[162]
Net aquifer thickness (m)	H	400	aquifer data	[99, Fig.2]
Length of model domain (km)	L_{aq}	100	aquifer data	Fig. 2-11
Length of pressure domain (km)	L_{pres}	300	aquifer data	Fig. 2-11
Width of well array (km)	W	200	aquifer data	Fig. 2-11
Porosity	ϕ	0.2	aquifer data	[99]
Caprock slope (degrees)	ϑ	0.5	calculated	[74, Map c1mtsimong]
Darcy velocity (cm/yr)	U	1	calculated	[63, Fig.43]
Aquifer permeability (mD)	k_{aq}	100	aquifer data	[162, p.57]
Mean vertical permeability (mD)	k_{cap}	0.01	estimated	[124, 153, 37]
Lateral overburden permeability (mD)	$\bar{k}_x$	50	calculated	Fig. 2-8
Vertical overburden permeability (mD)	$\bar{k}_z$	0.02	calculated	Fig. 2-8
Salinity (ppm)	s	100000	aquifer data	[1]
CO_2 solubility (volume fraction)	χ_v	0.05	calculated	[42]
Brine density (kg/m^3)	ρ_w	1000	calculated	[16]
CO_2 density (kg/m^3)	ρ_g	700	calculated	[25]
Brine density change from diss. (kg/m^3)	$\Delta\rho_d$	6	calculated	[60, 9]
Brine viscosity (mPa s)	μ_w	0.8	calculated	[16]
CO_2 viscosity (mPa s)	μ_g	0.06	calculated	[25]
Fracture (MPa)	P_{frac}	40	calculated	Eq. 2.29,2.28; [173]

Table 2.3: Parameters for Region b of the Mt. Simon Sandstone.

Parameter	Symbol	Value	Data Source	Reference
Residual CO_2 saturation	S_{rg}	0.3	estimated	[18, 130]
Connate water saturation	S_{wc}	0.4	estimated	[18, 130]
Endpoint relative permeability to CO_2	k_{rg}^*	0.6	estimated	[18, 130]
Coefficient of CO_2-saturated-brine flux	α	0.01	estimated	[87]
Compressibility (GPa^{-1})	c	0.1	estimated	[160, 26, 89, 32, 50, 115]
Undrained Poisson ratio	ν	0.3	estimated	[160, Table C1]
Geothermal gradient (°C/km)	G_T	20	aquifer data	[91, 119]
Surface temperature (°C)	T_s	9	aquifer data	[3]
Depth to top of aquifer (m)	D	2000	aquifer data	[15, Fig.4]
Depth from aquifer to bedrock (m)	B	0	aquifer data	[162]
Net aquifer thickness (m)	H	200	aquifer data	[15, Fig.4]
Length of model domain (km)	L_t	200	aquifer data	Fig. 2-11
Length of pressure domain (km)	L_{pres}	200	aquifer data	Fig. 2-11
Width of well array (km)	W	200	aquifer data	Fig. 2-11
Porosity	ϕ	0.2	aquifer data	[15]
Caprock slope (degree)	ϑ	0.7	calculated	[15, Fig.4]
Darcy velocity (cm/yr)	U	1	calculated	[63, Fig.43]
Aquifer permeability (mD)	k_{aq}	100	aquifer data	[162, p.57]
Caprock permeability (mD)	k_c	0.01	estimated	[124, 153, 37]
Lateral overburden permeability (mD)	$\bar{k}_x$	50	calculated	Fig. 2-8
Vertical overburden permeability (mD)	$\bar{k}_z$	0.02	calculated	Fig. 2-8
Salinity (g/L)	s	200	aquifer data	[95, Fig.37]
CO_2 solubility (volume fraction)	χ_v	0.04	calculated	[107, 42]
Brine density (kg/m^3)	ρ_w	1000	calculated	[16]
CO_2 density (kg/m^3)	ρ_g	800	calculated	[25]
Brine density change from diss. (kg/m^3)	$\Delta\rho_d$	8	calculated	[60, 9]
Brine viscosity (mPa s)	μ_w	1	calculated	[16]
CO_2 viscosity (mPa s)	μ_g	0.07	calculated	[25]
Fracture pressure (MPa)	P_{frac}	40	calculated	Eq. 2.29,2.28; [173]

Black Warrior River Aquifer

Following previous studies, we model a number of Cretaceous rocks in the southeastern Coastal Plain as a single aquifer called the Black Warrior River Aquifer [114, 137, 7, 146]. This aquifer begins in central Alabama and Georgia, where it either outcrops or pinches out, and from there it deepens and thickens toward the Gulf of Mexico. In Alabama and northwestern Florida, in consists of rocks in the Eutaw and McShan Formations and the Tuscaloosa Group. In Georgia and northeastern Florida, it consists of rocks in the Eutaw Formation, Tuscaloosa Formation, and the Atkinson Formation [114, Fig.72]. These rocks are mostly sandstone interbedded with siltstone, shale, and mudstone [114, 137, 146]. They where deposited in a variety of settings, including fluvial, deltaic, and marine environments.

A variety of rocks underlie the aquifer. These rocks include Precambrian crystalline rocks, Paleozoic and Mesozoic sedimentary rocks, and Lower Mesozoic redbeds and diabase [114, Fig.76]. While some of these rocks are porous and permeable, we do not model them because they are very poorly characterized. The aquifer is overlain by the Selma Group, which consists mostly of chalk and is recognized by many authors as a regional aquitard [114, 137, 146].

A variety of geologic features constrain the region of the Black Warrior River Aquifer that is suitable for sequestration, as shown in Figure 2-12. Within this region, we identify four model domains, also shown in Figure 2-12. The data for each domain are shown in Tables 2.5, 2.6, 2.7, and 2.8.
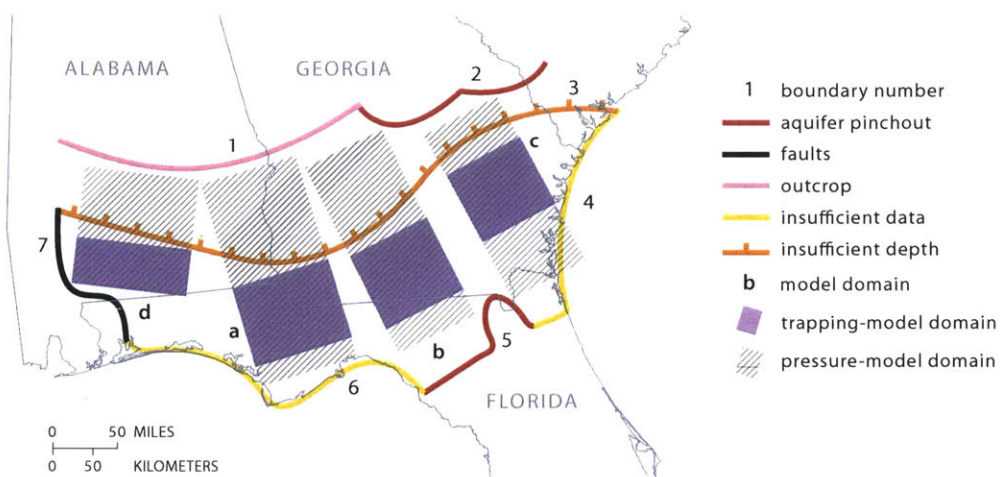
Figure 2-12: We identify seven boundaries that constrain the portion of the Black Warrior River Aquifer that is suitable for sequestration. Boundary 1 corresponds to where the aquifer crops out in central Alabama and Georgia [114, Fig.79]. Boundary 2 corresponds to where it pinches out between the overlying Chattahoochee River Aquifer and underlying low-permeability rocks [114]. Boundary 3 marks where the aquifer becomes shallower than 800m [114, Fig.79]. Boundaries 4 and 6 correspond to edge of available depth maps [114, 137, 5]. Boundary 5 shows where the aquifer pinches out or becomes very thin [5, Plate 3A]. Finally, Boundary 7 corresponds to where the aquifer becomes offset by a fault system by up to hundreds of meters. Within these boundaries, we identify four regions in which to apply our models (Regions a, b, c, and d).

Table 2.4: Parameters for Region c of the Mt. Simon Sandstone.

Parameter	Symbol	Value	Data Source	Reference
Residual CO_2 saturation	S_{rg}	0.3	estimated	[18, 130]
Connate water saturation	S_{wc}	0.4	estimated	[18, 130]
Endpoint relative permeability to CO_2	k_{rg}^*	0.6	estimated	[18, 130]
Coefficient of CO_2-saturated-brine flux	α	0.01	estimated	[87]
Compressibility (GPa^{-1})	c	0.1	estimated	[160, 26, 89, 32, 50, 115]
Undrained Poisson ratio	ν	0.3	estimated	[160, Table C1]
Geothermal gradient (°C/km)	G_T	20	aquifer data	[91, 119]
Surface temperature (°C)	T_s	10	aquifer data	[3]
Depth to top of aquifer (m)	D	1000	aquifer data	[74, Map c1simong]
Depth from aquifer to bedrock (m)	B	0	aquifer data	[162]
Net aquifer thickness (m)	H	100	aquifer data	[15, Fig.4]
Length of model domain (km)	L_t	300	aquifer data	Fig. 2-11
Length of pressure domain (km)	L_{pres}	200	aquifer data	Fig. 2-11
Width of well array (km)	W	200	aquifer data	Fig. 2-11
Porosity	ϕ	0.2	estimated	[55]
Caprock slope (degree)	ϑ	0.001	calculated	[74, Map c1simong]
Darcy velocity (cm/yr)	U	1	calculated	[63, Fig.43]
Aquifer permeability (mD)	k_{aq}	100	aquifer data	[162, p.57]
Caprock permeability (mD)	k_c	0.01	estimated	[124, 153, 37]
Lateral overburden permeability (mD)	$\bar{k}_x$	50	calculated	Fig. 2-8
Vertical overburden permeability (mD)	$\bar{k}_z$	0.02	calculated	Fig. 2-8
Salinity (g/L)	s	200	aquifer data	[95, Fig.37]
CO_2 solubility (volume fraction)	χ_v	0.04	calculated	[107, 42]
Brine density (kg/m^3)	ρ_w	1000	calculated	[16]
CO_2 density (kg/m^3)	ρ_g	700	calculated	[25]
Brine density change from diss. (kg/m^3)	$\Delta\rho_d$	7	calculated	[60, 9]
Brine viscosity (mPa s)	μ_w	1	calculated	[16]
CO_2 viscosity (mPa s)	μ_g	0.06	calculated	[25]
Fracture pressure (MPa)	P_{frac}	20	calculated	Eq. 2.29,2.28; [173]

Table 2.5: Parameters for Region a of the Black Warrior River Aquifer.

Parameter	Symbol	Value	Data Source	Reference
Residual CO_2 saturation	S_{rg}	0.3	estimated	[18, 130]
Connate water saturation	S_{wc}	0.4	estimated	[18, 130]
Endpoint relative permeability to CO_2	k_{rg}^*	0.6	estimated	[18, 130]
Coefficient of CO_2-saturated-brine flux	α	0.01	estimated	[87, 138]
Compressibility (GPa^{-1})	c	0.1	estimated	[160, Table C1]
Undrained Poisson ratio	ν	0.3	estimated	[160, Table C1]
Geothermal gradient (°C/km)	G_T	30	aquifer data	[91, 119]
Surface temperature (°C)	T_s	20	aquifer data	[3]
Depth to top of aquifer (m)	D	1000	aquifer data	[137, Plate41],[121]
Depth from aquifer to bedrock (m)	B	0	aquifer data	[114, Fig.76]
Net aquifer thickness (m)	H	1000	aquifer data	[137, Plate 42]
Length of model domain (km)	L_T	100	aquifer data	Fig. 2-12
Length of pressure domain (km)	L_{pres}	300	aquifer data	Fig. 2-12
Width of well array (km)	W	100	aquifer data	Fig. 2-12
Porosity	ϕ	0.2	estimated	[55]
Caprock slope (degrees)	ϑ	0.5	calculated	[137, Plate41]
Darcy velocity (cm/yr)	U	1	calculated	[98, p.D68]
Aquifer permeability (mD)	k_{aq}	100[a]	aquifer data	[14, Fig.30C][137, Plate 42]
Mean vertical permeability (mD)	k_{cap}	0.01	aquifer data	[141]
Lateral overburden permeability (mD)	$\overline{k}_x$	50	calculated	Fig. 2-8
Vertical overburden permeability (mD)	$\overline{k}_z$	0.02	calculated	Fig. 2-8
Salinity (g/L)	s	100	aquifer data	[97, Plate 2]
CO_2 solubility (volume fraction)	χ_v	0.05	calculated	[42]
Brine density (kg/m^3)	ρ_w	1000	calculated	[16]
CO_2 density (kg/m^3)	ρ_g	700	calculated	[25]
Brine density change from diss. (kg/m^3)	$\Delta \rho_d$	8	calculated	[60, 9]
Brine viscosity (mPa s)	μ_w	0.8	calculated	[16]
CO_2 viscosity (mPa s)	μ_g	0.05	calculated	[25]
Fracture pressure (MPa)	P_{frac}	20	calculated	Eq. 2.29,2.28; [173]

[a] Calculated from mapped values of transmissivity between 80 and 399 m^2/day [14, Fig.30C] and aquifer thickness [137, Plate 42].

Table 2.6: Parameters for Region b of the Black Warrior River Aquifer.

Parameter	Symbol	Value	Data Source	Reference
Residual CO_2 saturation	S_{rg}	0.3	estimated	[18, 130]
Connate water saturation	S_{wc}	0.4	estimated	[18, 130]
Endpoint relative permeability to CO_2	k_{rg}^*	0.6	estimated	[18, 130]
Coefficient of CO_2-saturated-brine flux	α	0.01	estimated	[87, 138]
Compressibility (GPa^{-1})	c	0.1	estimated	[160, Table C1]
Undrained Poisson ratio	ν	0.3	estimated	[160, Table C1]
Geothermal gradient (°C/km)	G_T	20	aquifer data	[91, 119]
Surface temperature (°C)	T_s	20	aquifer data	[3]
Depth to top of aquifer (m)	D	100	aquifer data	[137, Plate41],[121]
Depth from aquifer to bedrock (m)	B	0	aquifer data	[114, Fig.76]
Net aquifer thickness (m)	H	300	aquifer data	[137, Plate 42]
Length of model domain (km)	L_T	100	aquifer data	Fig. 2-12
Length of pressure domain (km)	L_{pres}	300	aquifer data	Fig. 2-12
Width of well array (km)	W	100	aquifer data	Fig. 2-12
Porosity	ϕ	0.2	estimated	[55]
Caprock slope (degrees)	ϑ	0.2	calculated	[137, Plate41]
Darcy velocity (cm/yr)	U	1	calculated	[98, p.D68]
Aquifer permeability (mD)	k_{aq}	400[a]	aquifer data	[14, Fig.30C][137, Plate 42]
Mean vertical permeability (mD)	k_{cap}	0.01	aquifer data	[141]
Lateral overburden permeability (mD)	$\overline{k}_x$	200	calculated	Fig. 2-8
Vertical overburden permeability (mD)	$\overline{k}_z$	0.02	calculated	Fig. 2-8
Salinity (g/L)	s	10	aquifer data	[97, Plate 2]
CO_2 solubility (volume fraction)	χ_v	0.07	calculated	[42]
Brine density (kg/m^3)	ρ_w	1000	calculated	[16]
CO_2 density (kg/m^3)	ρ_g	700	calculated	[25]
Brine density change from diss. (kg/m^3)	$\Delta\rho_d$	10	calculated	[60, 9]
Brine viscosity (mPa s)	μ_w	0.7	calculated	[16]
CO_2 viscosity (mPa s)	μ_g	0.06	calculated	[25]
Fracture pressure (MPa)	P_{frac}	10	calculated	Eq. 2.29,2.28; [173]

[a] Calculated from mapped values of transmissivity between 80 and 399 m^2/day [14, Fig.30C] and aquifer thickness [137, Plate 42].

Table 2.7: Parameters for Region c of the Black Warrior River Aquifer.

Parameter	Symbol	Value	Data Source	Reference
Residual CO_2 saturation	S_{rg}	0.3	estimated	[18, 130]
Connate water saturation	S_{wc}	0.4	estimated	[18, 130]
Endpoint relative permeability to CO_2	k_{rg}^*	0.6	estimated	[18, 130]
Coefficient of CO_2-saturated-brine flux	α	0.01	estimated	[87, 138]
Compressibility (GPa^{-1})	c	0.1	estimated	[160, Table C1]
Undrained Poisson ratio	ν	0.3	estimated	[160, Table C1]
Geothermal gradient (°C/km)	G_T	20	aquifer data	[91, 119]
Surface temperature (°C)	T_s	20	aquifer data	[3]
Depth to top of aquifer (m)	D	1000	aquifer data	[137, Plate41],[121]
Depth from aquifer to bedrock (m)	B	0	aquifer data	[114, Fig.76]
Net aquifer thickness (m)	H	200	aquifer data	[137, Plate 42]
Length of model domain (km)	L_T	90	aquifer data	Fig. 2-12
Length of pressure domain (km)	L_{pres}	200	aquifer data	Fig. 2-12
Width of well array (km)	W	100	aquifer data	Fig. 2-12
Porosity	ϕ	0.2	estimated	[55]
Caprock slope (degrees)	ϑ	0.2	calculated	[137, Plate41]
Darcy velocity (cm/yr)	U	1	calculated	[98, p.D68]
Aquifer permeability (mD)	k_{aq}	900[a]	aquifer data	[14, Fig.30C][137, Plate 42]
Mean vertical permeability (mD)	k_{cap}	0.01	aquifer data	[141]
Lateral overburden permeability (mD)	$\bar{k}_x$	500	calculated	Fig. 2-8
Vertical overburden permeability (mD)	$\bar{k}_z$	0.02	calculated	Fig. 2-8
Salinity (g/L)	s	10	aquifer data	[97, Plate 2]
CO_2 solubility (volume fraction)	χ_v	0.07	calculated	[42]
Brine density (kg/m^3)	ρ_w	1000	calculated	[16]
CO_2 density (kg/m^3)	ρ_g	700	calculated	[25]
Brine density change from diss. (kg/m^3)	$\Delta\rho_d$	10	calculated	[60, 9]
Brine viscosity (mPa s)	μ_w	0.7	calculated	[16]
CO_2 viscosity (mPa s)	μ_g	0.06	calculated	[25]
Fracture pressure (MPa)	P_{frac}	20	calculated	Eq. 2.29,2.28; [173]

[a] Calculated from mapped values of transmissivity between 80 and 399 m^2/day [14, Fig.30C] and aquifer thickness [137, Plate 42].

Table 2.8: Parameters for Region d of the Black Warrior River Aquifer.

Parameter	Symbol	Value	Data Source	Reference
Residual CO_2 saturation	S_{rg}	0.3	estimated	[18, 130]
Connate water saturation	S_{wc}	0.4	estimated	[18, 130]
Endpoint relative permeability to CO_2	k_{rg}^*	0.6	estimated	[18, 130]
Coefficient of CO_2-saturated-brine flux	α	0.01	estimated	[87, 138]
Compressibility (GPa^{-1})	c	0.1	estimated	[160, Table C1]
Undrained Poisson ratio	ν	0.3	estimated	[160, Table C1]
Geothermal gradient (°C/km)	G_T	30	aquifer data	[91, 119]
Surface temperature (°C)	T_s	20	aquifer data	[3]
Depth to top of aquifer (m)	D	1000	aquifer data	[137, Plate41],[121]
Depth from aquifer to bedrock (m)	B	0	aquifer data	[114, Fig.76]
Net aquifer thickness (m)	H	2000	aquifer data	[137, Plate 42]
Length of model domain (km)	L_T	60	aquifer data	Fig. 2-12
Length of pressure domain (km)	L_{pres}	100	aquifer data	Fig. 2-12
Width of well array (km)	W	100	aquifer data	Fig. 2-12
Porosity	ϕ	0.2	estimated	[55]
Caprock slope (degrees)	ϑ	0.6	calculated	[137, Plate41]
Darcy velocity (cm/yr)	U	1	calculated	[98, p.D68]
Aquifer permeability (mD)	k_{aq}	60[a]	aquifer data	[14, Fig.30C][137, Plate 42]
Mean vertical permeability (mD)	k_{cap}	0.01	aquifer data	[141]
Lateral overburden permeability (mD)	$\bar{k}_x$	30	calculated	Fig. 2-8
Vertical overburden permeability (mD)	$\bar{k}_z$	0.02	calculated	Fig. 2-8
Salinity (g/L)	s	80	aquifer data	[97, Plate 2]
CO_2 solubility (volume fraction)	χ_v	0.06	calculated	[42]
Brine density (kg/m^3)	ρ_w	1000	calculated	[16]
CO_2 density (kg/m^3)	ρ_g	700	calculated	[25]
Brine density change from diss. (kg/m^3)	$\Delta\rho_d$	9	calculated	[60, 9]
Brine viscosity (mPa s)	μ_w	0.7	calculated	[16]
CO_2 viscosity (mPa s)	μ_g	0.05	calculated	[25]
Fracture pressure (MPa)	P_{frac}	20	calculated	Eq. 2.29,2.28; [173]

[a] Calculated from mapped values of transmissivity between 80 and 399 m^2/day [14, Fig.30C] and aquifer thickness [137, Plate 42].

a. depth to top of the aquifer   b. thickness

Figure 2-13: The Frio Formation is located on the east coast of Texas. It dips and thickens toward the coast. (a) Modified from [74, Map c1friog1]. (b) Modified from [74, Map c4friog].

Frio Formation

The Frio Formation occurs in the Gulf Basin in Texas. Starting at outcrops about 150km inland from the coast, it dips and thickens uniformly toward the coast as shown in Figure 2-13, reaching depths of more than 3000m below sea level [72, p.21].

The Frio Formation is highly heterogeneous, consisting of interfingering marine and nonmarine sands and shales [59]. These sediments occur in a variety of facies such as deltaic and fluvial facies [73]. The Frio Formation is overlain by the Anuhac Formation and underlain by the Vicksburg Group and Jackson Group. These units are composed dominantly of clay and form an effective aquitard and aquiclude [140].

We model sequestration in a broad region of the Frio Formation along the Texas coast, as shown in Figure 2-14. Within this region, we identify three regions in which to apply our models (Regions a, b, and c). The data for each region are shown in Tables 2.9, 2.10, and 2.11.
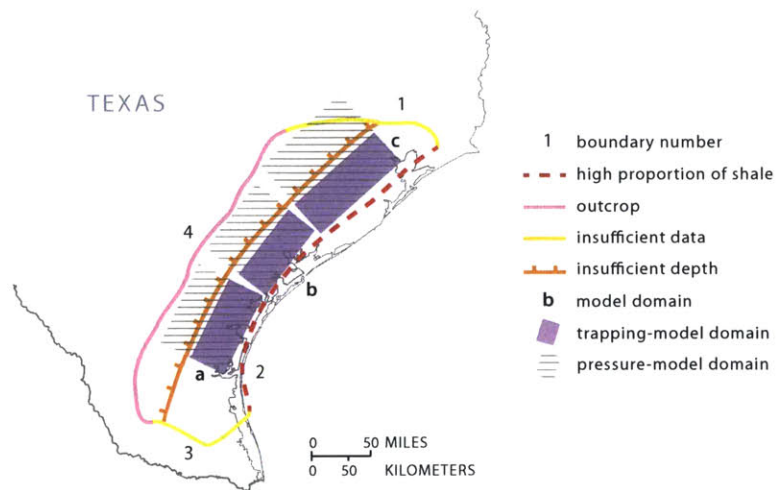
Figure 2-14: We identify four boundaries that constrain the portion of the Frio Formation that is suitable for sequestration. Boundaries 1 and 3 correspond to the edges of available depth and thickness maps [74]. Boundary 2 corresponds to where the proportion of shale in the formation becomes greater than 80% [74, Map 5frio]. Boundary 4 corresponds to outcrops [74]. Within these boundaries, we identify three regions in which to apply our models (Regions a, b, and c).

Table 2.9: Parameters for Region a of the Frio Formation.

Parameter	Symbol	Value	Data Source	Reference
Residual CO_2 saturation	S_{rg}	0.3	estimated	[18, 130]
Connate water saturation	S_{wc}	0.4	estimated	[18, 130]
Endpoint relative permeability to CO_2	k_{rg}^*	0.6	estimated	[18, 130]
Coefficient of CO_2-saturated-brine flux	α	0.01	estimated	[87, 138]
Compressibility (GPa^{-1})	c	0.1	estimated	[160, Table C1]
Undrained Poisson ratio	ν	0.3	estimated	[160, Table C1]
Geothermal gradient (°C/km)	G_T	30	aquifer data	[91, 119]
Surface temperature (°C)	T_s	20	aquifer data	[3]
Depth to top of aquifer (m)	D	1000	aquifer data	[74, Map c1friog1]
Depth from aquifer to bedrock (m)	B	10000	aquifer data	[56]
Net aquifer thickness (m)	H	2000	aquifer data	[74, Map c3friog]
Length of model domain (km)	L_T	50	aquifer data	Fig. 2-14
Length of pressure domain (km)	L_{pres}	100	aquifer data	Fig. 2-14
Width of well array (km)	W	100	aquifer data	Fig. 2-14
Porosity	ϕ	0.2	aquifer data	[103, Fig.10]
Caprock slope (degrees)	ϑ	2	calculated	[59, Fig.2]
Darcy velocity (cm/yr)	U	10[a]	calculated	[90]
Aquifer permeability (mD)	k_{aq}	400	aquifer data	[103, Fig.8]
Mean vertical permeability (mD)	k_{cap}	0.01	estimated	[124, 153, 37]
Lateral overburden permeability (mD)	$\bar{k}_x$	200	calculated	Fig. 2-8
Vertical overburden permeability (mD)	$\bar{k}_z$	0.02	calculated	Fig. 2-8
Salinity (g/L)	s	50	aquifer data	[118, Fig.2A]
CO_2 solubility (volume fraction)	χ_v	0.07	calculated	[42]
Brine density (kg/m^3)	ρ_w	1000	calculated	[16]
CO_2 density (kg/m^3)	ρ_g	500	calculated	[25]
Brine density change from diss. (kg/m^3)	$\Delta\rho_d$	8	calculated	[60, 9]
Brine viscosity (mPa s)	μ_w	0.8	calculated	[16]
CO_2 viscosity (mPa s)	μ_g	0.04	calculated	[25]
Fracture pressure (MPa)	P_{frac}	20	calculated	Eq. 2.29,2.28; [173]

[a] We set the Darcy velocity to 10 cm/yr based on reported ranges for the velocity [90] and values in other deep saline aquifers.

Table 2.10: Parameters for Region b of the Frio Formation.

Parameter	Symbol	Value	Data Source	Reference
Residual CO_2 saturation	S_{rg}	0.3	estimated	[18, 130]
Connate water saturation	S_{wc}	0.4	estimated	[18, 130]
Endpoint relative permeability to CO_2	k_{rg}^*	0.6	estimated	[18, 130]
Coefficient of CO_2-saturated-brine flux	α	0.01	estimated	[87, 138]
Compressibility (GPa^{-1})	c	0.1	estimated	[160, Table C1]
Undrained Poisson ratio	ν	0.3	estimated	[160, Table C1]
Geothermal gradient ($^\circ$C/km)	G_T	30	aquifer data	[91, 119]
Surface temperature ($^\circ$C)	T_s	20	aquifer data	[3]
Depth to top of aquifer (m)	D	1000	aquifer data	[74, Map c1friog1]
Depth from aquifer to bedrock (m)	B	10000	aquifer data	[56]
Net aquifer thickness (m)	H	900	aquifer data	[74, Map c3friog]
Length of model domain (km)	L_T	40	aquifer data	Fig. 2-14
Length of pressure domain (km)	L_{pres}	100	aquifer data	Fig. 2-14
Width of well array (km)	W	100	aquifer data	Fig. 2-14
Porosity	ϕ	0.2	aquifer data	[103, Fig.10]
Caprock slope (degrees)	ϑ	2	calculated	[59, Fig.2]
Darcy velocity (cm/yr)	U	10[a]	calculated	[90]
Aquifer permeability (mD)	k_{aq}	400	aquifer data	[103, Fig.8]
Mean vertical permeability (mD)	k_{cap}	0.01	estimated	[124, 153, 37]
Lateral overburden permeability (mD)	$\overline{k}_x$	200	calculated	Fig. 2-8
Vertical overburden permeability (mD)	$\overline{k}_z$	0.02	calculated	Fig. 2-8
Salinity (g/L)	s	50	aquifer data	[118, Fig.2A]
CO_2 solubility (volume fraction)	χ_v	0.08	calculated	[42]
Brine density (kg/m^3)	ρ_w	1000	calculated	[16]
CO_2 density (kg/m^3)	ρ_g	500	calculated	[25]
Brine density change from diss. (kg/m^3)	$\Delta \rho_d$	8	calculated	[60, 9]
Brine viscosity (mPa s)	μ_w	0.6	calculated	[16]
CO_2 viscosity (mPa s)	μ_g	0.04	calculated	[25]
Fracture pressure (MPa)	P_{frac}	20	calculated	Eq. 2.29,2.28; [173]

[a] We set the Darcy velocity to 10 cm/yr based on reported ranges for the velocity [90] and values in other deep saline aquifers.

Table 2.11: Parameters for Region c of the Frio Formation.

Parameter	Symbol	Value	Data Source	Reference
Residual CO_2 saturation	S_{rg}	0.3	estimated	[18, 130]
Connate water saturation	S_{wc}	0.4	estimated	[18, 130]
Endpoint relative permeability to CO_2	k_{rg}^*	0.6	estimated	[18, 130]
Coefficient of CO_2-saturated-brine flux	α	0.01	estimated	[87, 138]
Compressibility (GPa^{-1})	c	0.1	estimated	[160, Table C1]
Undrained Poisson ratio	ν	0.3	estimated	[160, Table C1]
Geothermal gradient (°C/km)	G_T	30	aquifer data	[91, 119]
Surface temperature (°C)	T_s	20	aquifer data	[3]
Depth to top of aquifer (m)	D	1000	aquifer data	[74, Map c1friog1]
Depth from aquifer to bedrock (m)	B	10000	aquifer data	[56]
Net aquifer thickness (m)	H	700	aquifer data	[74, Map c3friog]
Length of model domain (km)	L_T	50	aquifer data	Fig. 2-14
Length of pressure domain (km)	L_{pres}	100	aquifer data	Fig. 2-14
Width of well array (km)	W	100	aquifer data	Fig. 2-14
Porosity	ϕ	0.2	aquifer data	[103, Fig.10]
Caprock slope (degrees)	ϑ	6	calculated	[59, Fig.2]
Darcy velocity (cm/yr)	U	10^a	calculated	[90]
Aquifer permeability (mD)	k_{aq}	400	aquifer data	[103, Fig.8]
Mean vertical permeability (mD)	k_{cap}	0.01	estimated	[124, 153, 37]
Lateral overburden permeability (mD)	$\overline{k}_x$	200	calculated	Fig. 2-8
Vertical overburden permeability (mD)	$\overline{k}_z$	0.02	calculated	Fig. 2-8
Salinity (g/L)	s	100	aquifer data	[118, Fig.2A]
CO_2 solubility (volume fraction)	χ_v	0.08	calculated	[42]
Brine density (kg/m^3)	ρ_w	1000	calculated	[16]
CO_2 density (kg/m^3)	ρ_g	500	calculated	[25]
Brine density change from diss. (kg/m^3)	$\Delta\rho_d$	8	calculated	[60, 9]
Brine viscosity (mPa s)	μ_w	0.6	calculated	[16]
CO_2 viscosity (mPa s)	μ_g	0.04	calculated	[25]
Fracture pressure (MPa)	P_{frac}	20	calculated	Eq. 2.29,2.28; [173]

[a] We set the Darcy velocity to 10 cm/yr based on reported ranges for the velocity [90] and values in other deep saline aquifers.

a. depth to top of the aquifer   b. thickness

Figure 2-15: The Madison Limestone is located in Williston Basin in North Dakota, South Dakota, and Montana. The basin is roughly bowl-shaped, with the center and deepest part of the bowl located in western North Dakota. (a) Modified from [74, Map c1madisong]. (b) Modified from [40, Fig.11].

Madison Limestone

The Madison Limestone occurs in the Williston Basin [161]. In general, it dips and thickens towards the center of the basin in western North Dakota, as shown Figure 2-15.

The Madison Limestone consists of a sequence of carbonates and evaporates that are divided into three formations [40]. From oldest to youngest, these are the Lodgepole Limestone, the Mission Canyon Limestone, and the Charles Formation. The Lodgepole Limestone consists mainly of argillaceous, thin-bedded limestone and dolomite. The Mission Canyon Limestone consists mainly of limestone that is coarsely crystalline at its base and finer at its top. The Charles Formation consists of anhydrite and halite with interbedded dolomite and limestone.

In the Williston Basin, the Madison Limestone is overlain by the Big Snowy Group [40]. This group consists mostly of shale and sandstone, with minor limestone. We model it together with the Charles Formation as an aquitard. The aquifer is underlain by the Bakken Formation in the Williston Basin, which consists of more than 30 meters of shale and siltstone [40]. We model this formation as an aquiclude.

We model sequestration in two regions of the Madison Limestone, as shown in Figure 2-16. Within each region, we identify one model domain. The data for each domain are shown in Tables 2.12 and 2.13.
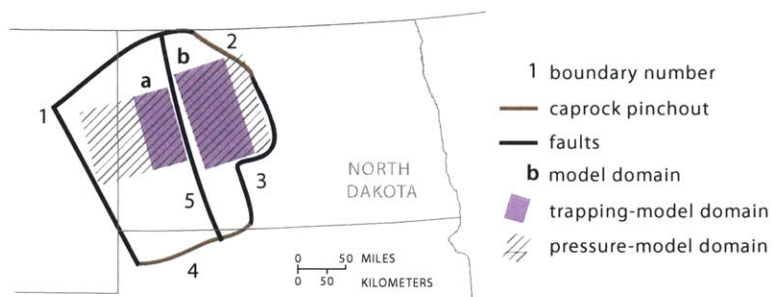
Figure 2-16: We identify five boundaries that constrain the portion of the Frio Formation that is suitable for sequestration. Boundaries 1, 3, and 5 correspond to basin-scale faults and lineaments [40, Fig.16]. Boundaries 2 and 4 correspond to where the caprock pinches out [40, Fig.12]. Within these boundaries, we identify two regions in which to apply our models (Regions a and b).

Table 2.12: Parameters for Region a of the Madison Limestone.

Parameter	Symbol	Value	Data Source	Reference
Residual CO_2 saturation	S_{rg}	0.3	estimated	[18, 130]
Connate water saturation	S_{wc}	0.4	estimated	[18, 130]
Endpoint relative permeability to CO_2	k_{rg}^*	0.6	estimated	[18, 130]
Coefficient of CO_2-saturated-brine flux	α	0.01	estimated	[87, 138]
Compressibility (GPa^{-1})	c	0.1	estimated	[160, Table C1]
Undrained Poisson ratio	ν	0.3	estimated	[160, Table C1]
Geothermal gradient (°C/km)	G_T	40	aquifer data	[91, 119]
Surface temperature (°C)	T_s	6	aquifer data	[3]
Depth to top of aquifer (m)	D	3000	aquifer data	[147]
Depth from aquifer to bedrock (m)	B	2000	aquifer data	[56]
Net aquifer thickness (m)	H	600	aquifer data	[147]
Length of model domain (km)	L_T	60	aquifer data	Fig. 2-16
Length of pressure domain (km)	L_{pres}	200	aquifer data	Fig. 2-16
Width of well array (km)	W	100	aquifer data	Fig. 2-16
Porosity	ϕ	0.08	estimated	[147]
Caprock slope (degrees)	ϑ	0.4	calculated	[147]
Darcy velocity (cm/yr)	U	8	calculated	[147]
Aquifer permeability (mD)	k_{aq}	60	aquifer data	[147]
Mean vertical permeability (mD)	k_{cap}	0.01	estimated	[124, 153, 37]
Lateral overburden permeability (mD)	$\overline{k}_x$	30	calculated	Fig. 2-8
Vertical overburden permeability (mD)	$\overline{k}_z$	0.02	calculated	Fig. 2-8
Salinity (g/L)	s	200	aquifer data	[161, Fig.61]
CO_2 solubility (volume fraction)	χ_v	0.05	calculated	[42]
Brine density (kg/m^3)	ρ_w	1000	calculated	[16]
CO_2 density (kg/m^3)	ρ_g	500	calculated	[25]
Brine density change from diss. (kg/m^3)	$\Delta\rho_d$	5	calculated	[60, 9]
Brine viscosity (mPa s)	μ_w	0.4	calculated	[16]
CO_2 viscosity (mPa s)	μ_g	0.04	calculated	[25]
Fracture pressure (MPa)	P_{frac}	30	calculated	Eq. 2.29,2.28; [173]

Table 2.13: Parameters for Region b of the Madison Limestone.

| Parameter	Symbol	Value	Data Source	Reference
Residual CO_2 saturation	S_{rg}	0.3	estimated	[18, 130]
Connate water saturation	S_{wc}	0.4	estimated	[18, 130]
Endpoint relative permeability to CO_2	k_{rg}^*	0.6	estimated	[18, 130]
Coefficient of CO_2-saturated-brine flux	α	0.01	estimated	[87, 138]
Compressibility (GPa^{-1})	c	0.1	estimated	[160, Table C1]
Undrained Poisson ratio	ν	0.3	estimated	[160, Table C1]
Geothermal gradient (°C/km)	G_T	40	aquifer data	[91, 119]
Surface temperature (°C)	T_s	6	aquifer data	[3]
Depth to top of aquifer (m)	D	2000	aquifer data	[147]
Depth from aquifer to bedrock (m)	B	1000	aquifer data	[56]
Net aquifer thickness (m)	H	500	aquifer data	[147]
Length of model domain (km)	L_T	90	aquifer data	Fig. 2-16
Length of pressure domain (km)	L_{pres}	100	aquifer data	Fig. 2-16
Width of well array (km)	W	200	aquifer data	Fig. 2-16
Porosity	ϕ	0.08	estimated	[147]
Caprock slope (degrees)	ϑ	0.5	calculated	[147]
Darcy velocity (cm/yr)	U	5	calculated	[147]
Aquifer permeability (mD)	k_{aq}	60	aquifer data	[147]
Mean vertical permeability (mD)	k_{cap}	0.01	estimated	[124, 153, 37]
Lateral overburden permeability (mD)	$\overline{k}_x$	30	calculated	Fig. 2-8
Vertical overburden permeability (mD)	$\overline{k}_z$	0.02	calculated	Fig. 2-8
Salinity (g/L)	s	300	aquifer data	[161, Fig.61]
CO_2 solubility (volume fraction)	χ_v	0.03	calculated	[42]
Brine density (kg/m^3)	ρ_w	1000	calculated	[16]
CO_2 density (kg/m^3)	ρ_g	500	calculated	[25]
Brine density change from diss. (kg/m^3)	$\Delta\rho_d$	11	calculated	[60, 9]
Brine viscosity (mPa s)	μ_w	0.6	calculated	[16]
CO_2 viscosity (mPa s)	μ_g	0.04	calculated	[25]
Fracture pressure (MPa)	P_{frac}	30	calculated	Eq. 2.29,2.28; [173]

Figure 2-17: We identify ten boundaries that constrain the portion of the Navajo-Nugget Aquifer that is suitable for sequestration. Boundaries 1, 6, and 10 correspond to basin-scale faults in Mesozoic rocks [53, Fig.6]. Boundaries 2, 4, and 8 mark where the Navajo-Nugget Aquifer is absent [54, Fig.14]. Boundaries 3 and 5 correspond to where the aquifer becomes more than 4000 m deep, which we consider to be too deep for a cost-effective sequestration project [121, 54]. Boundary 7 corresponds to the farthest extent of the Carmel-Twin Creek Confining Unit [53, Plate 2B]. Lastly, Boundary 9 corresponds to where the Navajo-Nugget Aquifer crops out [54, Fig.14]

Navajo-Nugget Aquifer

The Navajo-Nugget Aquifer is sufficiently deep for sequestration in the eastern Uinta Basin in northeastern Utah and the Green River Basin in southwest Wyoming [53, Figure 10]. In the eastern Uinta Basin, it consists of the Glen Canyon Sandstone. In the Green River Basin, it consists of the Nugget Sandstone [53, Plate 1]. These rocks were deposited primarily in an eolian environment, but contain minor fluvial components. They typically consist of massive, crossbedded sandstone that has well-sorted, very fine to medium grains [53, p.C17].

The Navajo-Nugget Aquifer is overlain by the Carmel-Twin Creek Confining Unit. This unit consists mostly of siltstone and shale with some interbedded gypsum. The aquifer is underlain by the Chinle-Moenkopi Confining Unit. This unit consists mostly of siltstone, claystone, and limestone [53, Table 1].

We model sequestration from one well array in both the Uinta Basin and the Green River Basin, as shown in Figure 2-17. The data for these regions are shown in Tables 2.14 and 2.15.

Table 2.14: Parameters for Region a of the Navajo-Nugget Aquifer.

Parameter	Symbol	Value	Data Source	Reference
Residual CO_2 saturation	S_{rg}	0.3	estimated	[18, 130]
Connate water saturation	S_{wc}	0.4	estimated	[18, 130]
Endpoint relative permeability to CO_2	k_{rg}^*	0.6	estimated	[18, 130]
Coefficient of CO_2-saturated-brine flux	α	0.01	estimated	[87, 138]
Compressibility (GPa^{-1})	c	0.1	estimated	[160, Table C1]
Undrained Poisson ratio	ν	0.3	estimated	[160, Table C1]
Geothermal gradient (°C/km)	G_T	30	aquifer data	[91, 119]
Surface temperature (°C)	T_s	6	aquifer data	[3]
Depth to top of aquifer (m)	D	3000	aquifer data	[121, 54]
Depth from aquifer to bedrock (m)	B	500	aquifer data	[56, 54, 53]
Net aquifer thickness (m)	H	200	aquifer data	[53, Plate 3A]
Length of trapping-model domain (km)	L_T	30	aquifer data	Fig. 2-17
Length of pressure-model domain (km)	L_{pres}	90	aquifer data	Fig. 2-17
Width of well array (km)	W	200	aquifer data	Fig. 2-17
Porosity	ϕ	0.2	estimated	[53, Fig.30]
Caprock slope (degrees)	ϑ	2	calculated	[54]
Darcy velocity (cm/yr)	U	10	calculated	[54, Fig.15]
Aquifer permeability (mD)	k_{aq}	100	calculated	[53, Figs.33,46]
Mean vertical permeability (mD)	k_{cap}	0.01	estimated	[124, 153, 37]
Lateral overburden permeability (mD)	$\bar{k}_x$	50	calculated	Fig. 2-8
Vertical overburden permeability (mD)	$\bar{k}_z$	0.02	calculated	Fig. 2-8
Salinity (g/L)	s	35	aquifer data	[54, Fig.19]
CO_2 solubility (volume fraction)	χ_v	0.07	calculated	[107, 42]
Brine density (kg/m^3)	ρ_w	1000	calculated	[16]
CO_2 density (kg/m^3)	ρ_g	600	calculated	[25]
Brine density change from diss. (kg/m^3)	$\Delta \rho_d$	9	calculated	[60, 9]
Brine viscosity (mPa s)	μ_w	0.4	calculated	[16]
CO_2 viscosity (mPa s)	μ_g	0.05	calculated	[25]
Fracture pressure (MPa)	P_{frac}	70	calculated	Eq. 2.29,2.28; [173]

Table 2.15: Parameters for Region b of the Navajo-Nugget Aquifer.

Parameter	Symbol	Value	Data Source	Reference
Residual CO_2 saturation	S_{rg}	0.3	estimated	[18, 130]
Connate water saturation	S_{wc}	0.4	estimated	[18, 130]
Endpoint relative permeability to CO_2	k_{rg}^*	0.6	estimated	[18, 130]
Coefficient of CO_2-saturated-brine flux	α	0.01	estimated	[87, 138]
Compressibility (GPa^{-1})	c	0.1	estimated	[160, Table C1]
Undrained Poisson ratio	ν	0.3	estimated	[160, Table C1]
Geothermal gradient (°C/km)	G_T	30	aquifer data	[91, 119]
Surface temperature (°C)	T_s	10	aquifer data	[3]
Depth to top of aquifer (m)	D	3000	aquifer data	[121, 54]
Depth from aquifer to bedrock (m)	B	5000	aquifer data	[56, 54, 53]
Net aquifer thickness (m)	H	200	aquifer data	[53, Plate 3A]
Length of trapping-model domain (km)	L_T	50	aquifer data	Fig. 2-17
Length of pressure-model domain (km)	L_{pres}	200	aquifer data	Fig. 2-17
Width of well array (km)	W	100	aquifer data	Fig. 2-17
Porosity	ϕ	0.2	estimated	[53, Fig.30]
Caprock slope (degrees)	ϑ	2	calculated	[54]
Darcy velocity (cm/yr)	U	10	calculated	[54, Fig.15]
Aquifer permeability (mD)	k_{aq}	100	calculated	[53, Figs.33,46]
Mean vertical permeability (mD)	k_{cap}	0.01	estimated	[124, 153, 37]
Lateral overburden permeability (mD)	$\bar{k}_x$	50	calculated	Fig. 2-8
Vertical overburden permeability (mD)	$\bar{k}_z$	0.02	calculated	Fig. 2-8
Salinity (g/L)	s	35	aquifer data	[54, Fig.19]
CO_2 solubility (volume fraction)	χ_v	0.07	calculated	[107, 42]
Brine density (kg/m^3)	ρ_w	1000	calculated	[16]
CO_2 density (kg/m^3)	ρ_g	600	calculated	[25]
Brine density change from diss. (kg/m^3)	$\Delta\rho_d$	10	calculated	[60, 9]
Brine viscosity (mPa s)	μ_w	0.4	calculated	[16]
CO_2 viscosity (mPa s)	μ_g	0.05	calculated	[25]
Fracture pressure (MPa)	P_{frac}	60	calculated	Eq. 2.29,2.28; [173]

a. depth to top of the aquifer   b. thickness
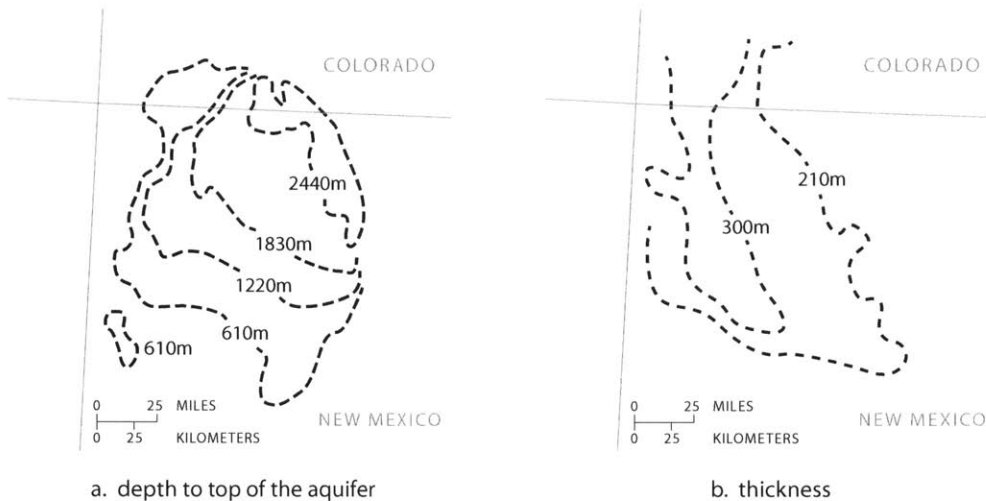
Figure 2-18: (a) The Morrison Formation deepens toward a northwest-southeast axis in the north-eastern part of the San Juan Basin. Modified from [33, Fig.6]. (b) It thickens toward a north-south axis in the western part of the basin. Modified from [33, Fig.5].

Morrison Formation

The Morrison Formation occurs in the northwestern corner of New Mexico in the San Juan Basin, as shown in Figure 2-18. It consists of five members that have varying extents [84, p.48]. The bottom three members are the Salt Wash Member, the Recapture Member, and the Westwater Canyon Member. These members consist mainly of interbedded sandstone and claystone, and are the target members for sequestration in our study [30, p.135-155]. They are overlain by the Brushy Basin Member and the Jackpile Sandstone Member. The Brushy Basin member consists predominantly of claystone that contains varying amounts of silt and sand [30, p.135-156]. We take it to be the caprock in our study.

The Morrison Formation is underlain by the Wanakah Formation in the San Juan Basin. The uppermost member of this formation is the Todilto Member, which consists of limestone overlain by gypsum and anhydrite. The Wanakah Formation has been identified in previous hydrologic studies as a confining unit, and we take it to be the aquiclude in our study [84, p.54].

We model sequestration in the center of the San Juan Basin, as shown in Figure 2-19. The data for this region are shown in Table 2.16.
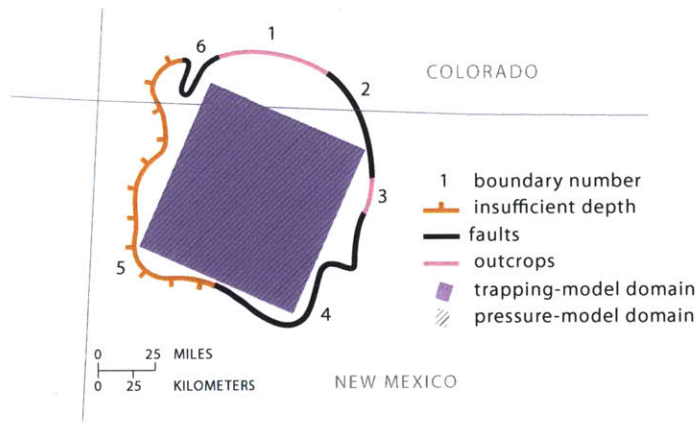
Figure 2-19: We identify six boundaries that constrain the portion of the Morrison Formation that is suitable for sequestration. Boundaries 1 and 3 correspond to outcrops, and Boundary 5 corresponds to where the depth to the top of the formation becomes less than 800 m [33, Fig.6]. Boundaries 2, 4, and 6 exclude major faults or fault systems in the San Juan Basin from the study area [84, Fig.7].

Table 2.16: Parameters for the Morrison Formation.

| Parameter	Symbol	Value	Data Source	Reference
Residual CO_2 saturation	S_{rg}	0.3	estimated	[18, 130]
Connate water saturation	S_{wc}	0.4	estimated	[18, 130]
Endpoint relative permeability to CO_2	k_{rg}^*	0.6	estimated	[18, 130]
Coefficient of CO_2-saturated-brine flux	α	0.01	estimated	[87, 138]
Compressibility (GPa^{-1})	c	0.1	estimated	[160, Table C1]
Undrained Poisson ratio	ν	0.3	estimated	[160, Table C1]
Geothermal gradient (°C/km)	G_T	30	aquifer data	[91, 119]
Surface temperature (°C)	T_s	10	aquifer data	[3]
Depth to top of aquifer (m)	D	2000	aquifer data	[33, Fig.6][30, Fig.29]
Depth from aquifer to bedrock (m)	B	1000	aquifer data	[56]
Net aquifer thickness (m)	H	200	aquifer data	[33, Fig.5][30, Fig.29]
Length of trapping-model domain (km)	L_T	100	aquifer data	Fig. 2-19
Length of pressure-model domain (km)	L_{pres}	100	aquifer data	Fig. 2-19
Width of well array (km)	W	100	aquifer data	Fig. 2-19
Porosity	ϕ	0.2	estimated	
Caprock slope (degrees)	ϑ	0.9	calculated	[33, Fig.7]
Darcy velocity (cm/yr)	U	8	calculated	[84, Fig.52][33, Fig.8]
Aquifer permeability (mD)	k_{aq}	70	calculated	[33, Fig.9]
Mean vertical permeability (mD)	k_{cap}	0.01	estimated	[124, 153, 37]
Lateral overburden permeability (mD)	$\bar{k}_x$	40	calculated	Fig. 2-8
Vertical overburden permeability (mD)	$\bar{k}_z$	0.02	calculated	Fig. 2-8
Salinity (g/L)	s	5	aquifer data	[33, Fig.15]
CO_2 solubility (volume fraction)	χ_v	0.09	calculated	[42]
Brine density (kg/m^3)	ρ_w	1000	calculated	[16]
CO_2 density (kg/m^3)	ρ_g	600	calculated	[25]
Brine density change from diss. (kg/m^3)	$\Delta\rho_d$	10	calculated	[60, 9]
Brine viscosity (mPa s)	μ_w	0.4	calculated	[16]
CO_2 viscosity (mPa s)	μ_g	0.04	calculated	[25]
Fracture pressure (MPa)	P_{frac}	50	calculated	Eq. 2.29,2.28; [173]
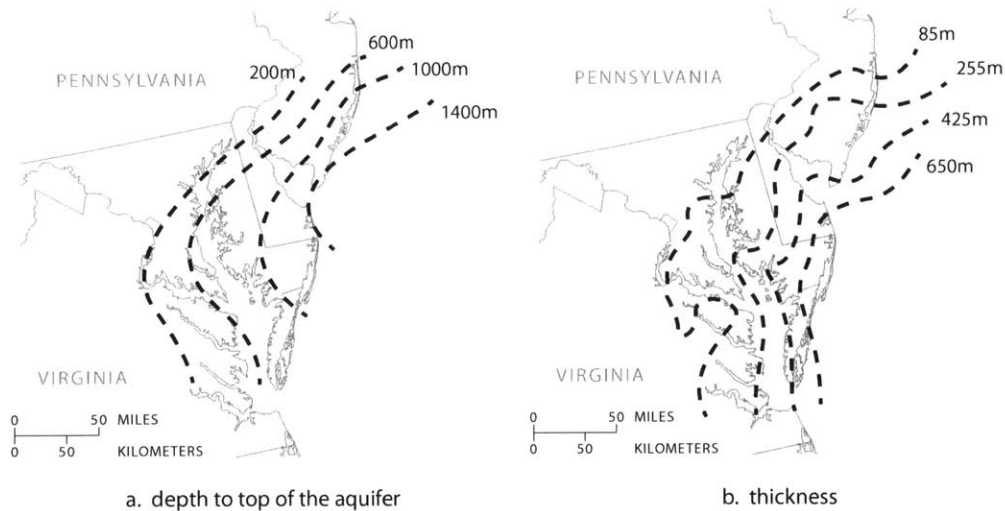
Figure 2-20: (a) The western limit of the aquifer is the Fall Line, where it pinches out against crystalline rock [155]. From the Fall Line, it dips and thickens seaward. (a) Modified from [74, Map c1potomac]. (b) Modified from [74, Map c3potomac].

Lower Potomac Aquifer

While the Lower Potomac Aquifer underlies almost the entire North Atlantic Coastal Plain, we study sequestration in Maryland and Delaware. Here it consists mostly of sediments deposited in fluvial or deltaic environments: it contains lenses of sand and gravel with interstitial clay [154, p.G30]. These lenses constitute between 20 and 60% of the aquifer thickness, and are interbedded with clayey and silty layers.

The aquifer is bounded above by a confining unit composed mostly of clay and sandy clay beds. It is bounded below by crystalline bedrock [154, 155].

While the Lower Potomac Aquifer extends under the Chesapeake Bay and the Atlantic Ocean, we study CO_2 storage only under the Delmarva Peninsula, as shown in Figure 2-21. The data for this region is shown in Table 2.17.

70
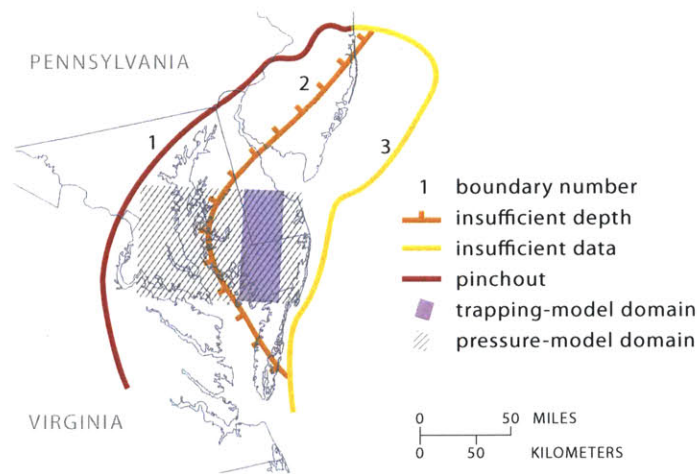
Figure 2-21: We identify 3 boundaries that constrain the portion of the Lower Potomac Aquifer that is suitable for sequestration. Boundary 1 corresponds to the Fall Line, where Coastal Plain sediments crop out or pinch out against the crystalline basement [154, Plate 1A,1B]. Since it is unclear whether the Lower Potomac pinches out or crops out in the study area, we choose this boundary to be a pinchout boundary to make our capacity estimates conservative. Boundary 2 corresponds to where the top of the aquifer becomes less than 800 m deep [74, Map c1potomac]. Boundary 3 corresponds to the limits of the aquifer depth and thickness maps [74, Maps c1potomac, c3potomac].

Table 2.17: Parameters for the Lower Potomac Aquifer.

Parameter	Symbol	Value	Data Source	Reference
Residual CO_2 saturation	S_{rg}	0.3	estimated	[18, 130]
Connate water saturation	S_{wc}	0.4	estimated	[18, 130]
Endpoint relative permeability to CO_2	k_{rg}^*	0.6	estimated	[18, 130]
Coefficient of CO_2-saturated-brine flux	α	0.01	estimated	[87, 138]
Compressibility (GPa^{-1})	c	0.1	estimated	[160, Table C1]
Undrained Poisson ratio	ν	0.3	estimated	[160, Table C1]
Geothermal gradient (°C/km)	G_T	30	aquifer data	[91, 119]
Surface temperature (°C)	T_s	10	aquifer data	[3]
Depth to top of aquifer (m)	D	1000	aquifer data	[74, Map c1potomac]
Depth from aquifer to bedrock (m)	B	0	aquifer data	[155, Fig.19,20]
Net aquifer thickness (m)	H	400	aquifer data	[74, Map c4potomac]
Length of trapping-model domain (km)	L_T	40	aquifer data	Fig. 2-21
Length of pressure-model domain (km)	L_{pres}	100	aquifer data	Fig. 2-21
Width of well array (km)	W	100	aquifer data	Fig. 2-21
Porosity	ϕ	0.2	estimated	
Caprock slope (degrees)	ϑ	0.3	calculated	[154, Plate 7B]
Darcy velocity (cm/yr)	U	10	calculated	[147, Table A.1]
Aquifer permeability (mD)	k_{aq}	3000	calculated	[147, Table A.1]
Mean vertical permeability (mD)	k_{cap}	0.1	estimated	[124, 153, 37]
Lateral overburden permeability (mD)	$\bar{k}_x$	2000	calculated	Fig. 2-8
Vertical overburden permeability (mD)	$\bar{k}_z$	0.2	calculated	Fig. 2-8
Salinity (g/L)	s	5	aquifer data	[155, Fig.57]
CO_2 solubility (volume fraction)	χ_v	0.1	calculated	[42]
Brine density (kg/m^3)	ρ_w	1000	calculated	[16]
CO_2 density (kg/m^3)	ρ_g	500	calculated	[25]
Brine density change from diss. (kg/m^3)	$\Delta\rho_d$	10	calculated	[60, 9]
Brine viscosity (mPa s)	μ_w	0.7	calculated	[16]
CO_2 viscosity (mPa s)	μ_g	0.04	calculated	[25]
Fracture pressure (MPa)	P_{frac}	20	calculated	Eq. 2.29,2.28; [173]

MONTANA

870m

290m

1740m

WYOMING

0   50 MILES

0   50   KILOMETERS

a. depth to top of the aquifer

MONTANA

200m

330m

WYOMING

580m

0   50 MILES

0   50   KILOMETERS

b. thickness

Figure 2-22: The Fox Hills Sandstone deepens along the axis of the Powder River Basin, which runs northwest to southeast. It thickens toward the southeast. (a) Modified from [74, Map c1foxhillsg]. (b) Modified from [74, Map c3foxhillsg].

Fox Hills Sandstone

The Fox Hills Sandstone occurs in the Powder River Basin, which is located in northeastern Wyoming. In general, it consists of massive, fine- to medium-grained sandstone with siltstone and minor shale, which are sometimes interbedded [112, p.T68]. The depth to the top of these rocks and their thickness are shown in Figure 2-22.

The Fox Hills Sandstone is conformably overlain by and intertongued with the Lance Formation in Wyoming, which provides an extensive top seal [76, p.82]. It is conformably underlain by marine shale and siltstone in the Lewis Shale or Pierre Shale, which forms an aquiclude [41, Plate II].

We model sequestration in the center of the Powder River Basin, as shown in Figure 2-23. The data for this region is shown in Table 2.18.
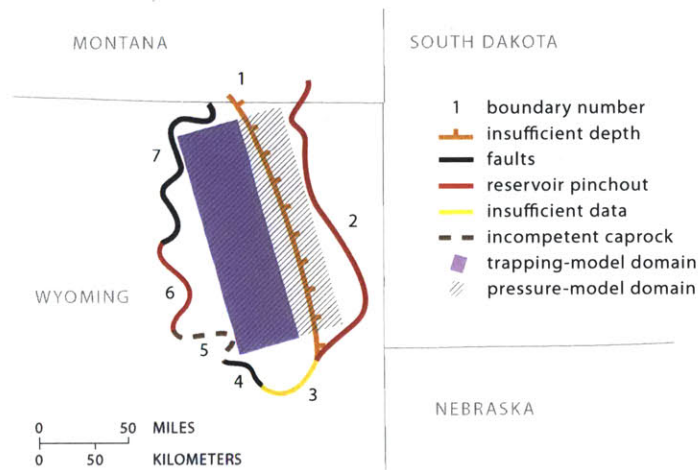
Figure 2-23: We identify 7 boundaries that constrain the portion of the Fox Hills Sandstone that is suitable for sequestration. Boundary 1 corresponds to where the top of the reservoir becomes less than 800 m deep [74, Map c1foxhillsg]. Boundaries 2 and 6 correspond to where we interpret the reservoir to pinch out. While we found no cross sections of the reservoir at these locations, we base this interpretation on the observation that the caprock and rocks stratigraphically below the reservoir crop out contiguously there [161, Fig.56]. Boundary 3 corresponds to the limit of the reservoir depth and thickness maps [74, Maps c1foxhillsg, c3foxhillsg]. Boundaries 4 and 7 correspond to basin-scale faults [161, Fig.56]. Lastly, Boundary 5 corresponds to where the caprock contains more than 50% sand [74, Map 81foxhillsg].

Table 2.18: Parameters for the Fox Hills Sandstone.

Parameter	Symbol	Value	Data Source	Reference
Residual CO_2 saturation	S_{rg}	0.3	estimated	[18, 130]
Connate water saturation	S_{wc}	0.4	estimated	[18, 130]
Endpoint relative permeability to CO_2	k_{rg}^*	0.6	estimated	[18, 130]
Coefficient of CO_2-saturated-brine flux	α	0.01	estimated	[87, 138]
Compressibility (GPa^{-1})	c	0.1	estimated	[160, Table C1]
Undrained Poisson ratio	ν	0.3	estimated	[160, Table C1]
Geothermal gradient (°C/km)	G_T	30	aquifer data	[91, 119]
Surface temperature (°C)	T_s	10	aquifer data	[3]
Depth to top of aquifer (m)	D	1000	aquifer data	[74, Map c1foxhillsg]
Depth from aquifer to bedrock (m)	B	4000	aquifer data	[56]
Net aquifer thickness (m)	H	200	aquifer data	[74, Map 4foxhills]
Length of trapping-model domain (km)	L_T	100	aquifer data	Fig. 2-23
Length of pressure-model domain (km)	L_{pres}	100	aquifer data	Fig. 2-23
Width of well array (km)	W	200	aquifer data	Fig. 2-23
Porosity	ϕ	0.2	estimated	
Caprock slope (degrees)	ϑ	1	calculated	[74, Map c1foxhillsg]
Darcy velocity (cm/yr)	U	10[a]	calculated	[161, Fig.56], [110]
Aquifer permeability (mD)	k_{aq}	100	calculated	[110]
Mean vertical permeability (mD)	k_{cap}	.01	estimated	[124, 153, 37]
Lateral overburden permeability (mD)	$\bar{k}_x$	50	calculated	Fig. 2-8
Vertical overburden permeability (mD)	$\bar{k}_z$	0.02	calculated	Fig. 2-8
Salinity (g/L)	s	2	aquifer data	[161, Fig.57]
CO_2 solubility (volume fraction)	χ_v	0.1	calculated	[42]
Brine density (kg/m^3)	ρ_w	1000	calculated	[16]
CO_2 density (kg/m^3)	ρ_g	500	calculated	[25]
Brine density change from diss. (kg/m^3)	$\Delta\rho_d$	11	calculated	[60, 9]
Brine viscosity (mPa s)	μ_w	0.7	calculated	[16]
CO_2 viscosity (mPa s)	μ_g	0.04	calculated	[25]
Fracture pressure (MPa)	P_{frac}	10	calculated	Eq. 2.29,2.28; [173]

[a] We calculate the Darcy velocity with Darcy's law, using a head gradient of 0.003 [161, Fig.56].

a. depth to top of the aquifer   b. thickness
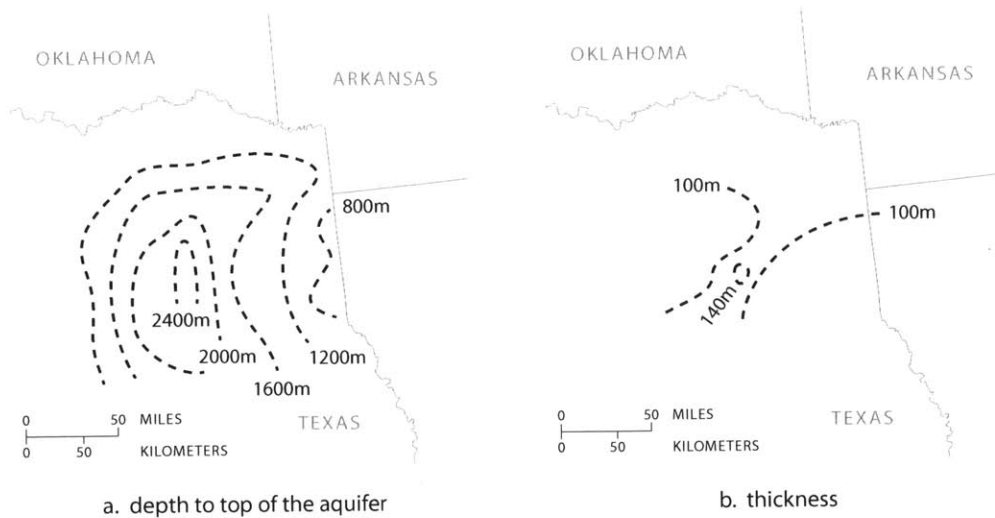
Figure 2-24: The Paluxy Formation deepens and thickens toward the center of the East Texas Basin. (a) Modified from [74, Map c1paluxyg]. (b) Modified from [74, Map c3paluxyg].

Paluxy Sandstone

While the Paluxy Formation is widespread throughout the Gulf Coastal Plain, we focus on deep parts of the formation in the East Texas Basin, which lies in northeastern Texas [52]. The depth to the top of the formation and its thickness is shown in Figure 2-24.

In the East Texas Basin, the Paluxy Formation is a quartz arenite, but in some areas can contain up to fifty percent clay [76, p.163]. It is overlain by the Goodland Limestone, which can be fairly porous and is likely a poor caprock. This limestone, however, is overlain by the Kiamichi Shale. We model this shale as the aquitard in our study and ignore the intervening Goodland Limestone since it is thin compared to the Paluxy Formation. The Paluxy is underlain by interbedded shale and limestone in the Glen Rose Formation, which we model as the aquiclude [52].

We model sequestration in the center of the East Texas Basin, as shown in Figure 2-25. The data for this region is shown in Table 2.19.
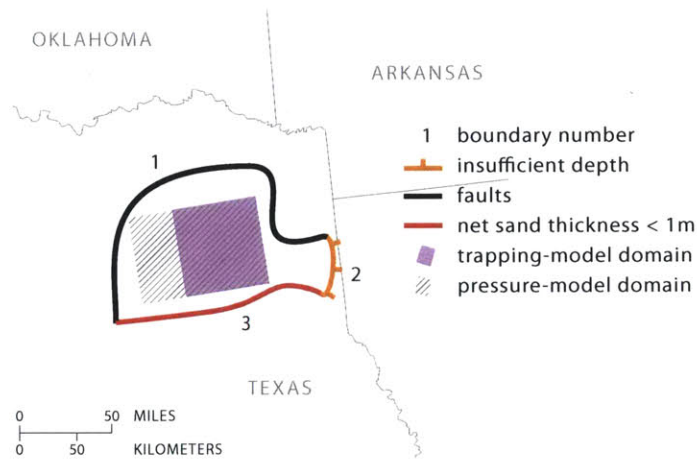
Figure 2-25: We identify three boundaries that constrain the portion of the Paluxy Sandstone that is suitable for sequestration. Boundary 1 corresponds to the edges of four major fault zones: the Mexia Fault Zone, the Talco Fault Zone, and the South Arkansas Fault Zone [52, Fig.3]. Boundary 2 corresponds to where the top of the formation becomes less than 800m deep [74, Map c1paluxyg]. Boundary 3 marks where the net sand thickness in the formation becomes less than 1m [74, Map c4paluxyg].

Table 2.19: Parameters for the Paluxy Sandstone.

Parameter	Symbol	Value	Data Source	Reference
Residual CO_2 saturation	S_{rg}	0.3	estimated	[18, 130]
Connate water saturation	S_{wc}	0.4	estimated	[18, 130]
Endpoint relative permeability to CO_2	k_{rg}^*	0.6	estimated	[18, 130]
Coefficient of CO_2-saturated-brine flux	α	0.01	estimated	[87, 138]
Compressibility (GPa^{-1})	c	0.1	estimated	[160, Table C1]
Undrained Poisson ratio	ν	0.3	estimated	[160, Table C1]
Geothermal gradient (°C/km)	G_T	30	aquifer data	[91, 119]
Surface temperature (°C)	T_s	20	aquifer data	[3]
Depth to top of aquifer (m)	D	2000	aquifer data	[74, Map c1paluxyg]
Depth from aquifer to bedrock (m)	B	6000	aquifer data	[56][74, Map c1paluxyg]
Net aquifer thickness (m)	H	15	aquifer data	[74, Map c3paluxyg]
Length of trapping-model domain (km)	L_T	70	aquifer data	Fig. 2-25
Length of pressure-model domain (km)	L_{pres}	100	aquifer data	Fig. 2-25
Width of well array (km)	W	80	aquifer data	Fig. 2-25
Porosity	ϕ	0.2	aquifer data	[74, Map 14paluxy]
Caprock slope (degrees)	ϑ	1	calculated	[74, Map c1paluxyg]
Darcy velocity (cm/yr)	U	5.0	estimated	
Aquifer permeability (mD)	k_{aq}	300	aquifer data	[74, Map 2paluxy]
Mean vertical permeability (mD)	k_{cap}	0.01	estimated	[124, 153, 37]
Lateral overburden permeability (mD)	$\overline{k}_x$	100	calculated	Fig. 2-8
Vertical overburden permeability (mD)	$\overline{k}_z$	0.02	calculated	Fig. 2-8
Salinity (ppm)	s	100000	aquifer data	[74, Map 12cpaluxy]
CO_2 solubility (volume fraction)	χ_v	0.05	calculated	[42]
Brine density (kg/m^3)	ρ_w	1000	calculated	[16]
CO_2 density (kg/m^3)	ρ_g	600	calculated	[25]
Brine density change from diss. (kg/m^3)	$\Delta\rho_d$	7	calculated	[60, 9]
Brine viscosity (mPa s)	μ_w	0.5	calculated	[16]
CO_2 viscosity (mPa s)	μ_g	0.04	calculated	[25]
Fracture pressure (MPa)	P_{frac}	30	calculated	Eq. 2.29,2.28; [173]

St. Peter Sandstone

While the St. Peter Sandstone is widespread in the Mississippi River Valley, we model sequestration only in the Illinois Basin where it is sufficiently deep and well characterized. The structure of the formation in this basin is shown in Figure 2-26.

The stratigraphy of the St. Peter Sandstone is complicated. It consists of three members whose occurrence and size vary with location: the Kress Member, the Tonti Member, and the Starved Rock Sandstone Member. The Kress Member is the lowermost unit and is present only in central and northern Illinois Basin. It is composed of poorly-sorted, cherty conglomerate, clayey sandstone, and shale. The Tonti Member is the middle member and is generally the most widespread and thickest unit in the St. Peter. It is a fine-grained, very pure quartz arenite. The Starved Rock Sandstone is the uppermost member and is mostly present in the northern and central Illinois Basin. It is a quartz sandstone like the Tonti Member, but is medium-grained and more cross-bedded [169, 164].

The St. Peter Sandstone is overlain by at least four different formations or groups in different parts of the Illinois Basin: the Dutchtown Limestone [88, Fig.5-10], the Joachim Dolomite [88, Fig.5-11], the Platteville Group, and the Glenwood Formation [164, p.63]. While these rocks exhibit a variety of different lithologies, we take them as a group to be an aquitard because all of the rocks contain low-permeability layers. For example, the Dutchtown Limestone contains beds of shale; the Joachim Dolomite contains beds of shale, gypsum, and anhydrite; the Platteville Group contains beds of chert and shale; and the uppermost layer in the Glenwood Formation is composed of shale. Other authors have also suggested that at least some of these rocks will act as a caprock [169, 76]. If this assumption is wrong, the overlying Maquoketa Shale is a well-recognized caprock [169, 108].

The St. Peter Sandstone is underlain by a variety of rocks since its base is a major regional unconformity [164, Fig.O-13]. In the southernmost part of the Illinois Basin, it is underlain by the Everton Dolomite. In the northernmost part of the basin, it is underlain by the Cambrian Potosi Dolomite, Franconia Formation, and Eminance Formation. In most of the remaining parts of the region, the St. Peter is underlain by Ordovician rocks in the Prairie du Chien Group: the Shakopee Dolomite, the New Richmond Sandstone, the Oneota Dolomite, and the Gunter Sandstone [164, p.45-60]. Although we do not identify these rocks as a regional aquiclude, we do not consider them for sequestration since their

a. depth to top of the aquifer   b. thickness
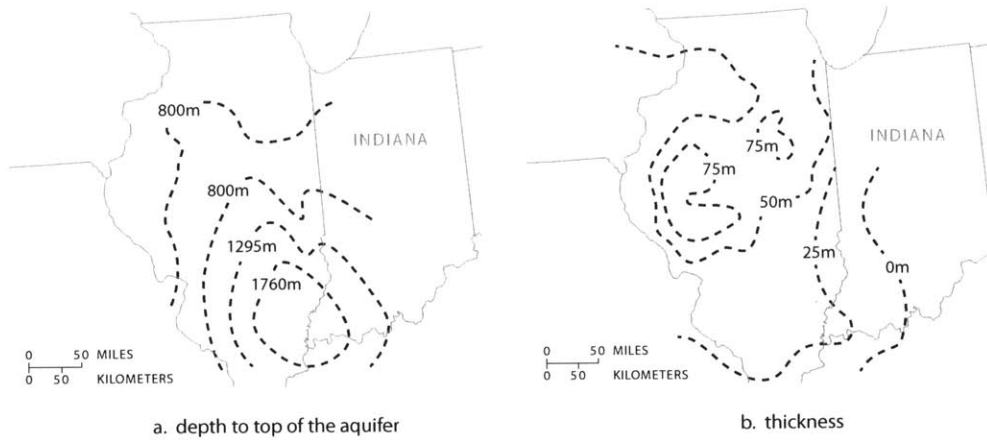
Figure 2-26: (a) The St. Peter Sandstone dips toward the center of the Illinois Basin in southern Illinois. Modified from [74, Map c1stpeter]. (b) Its thickness is highly variable due to irregularities in an unconformity at the base of the formation and post-depositional erosion [164, p.62]. In some areas, this erosion has completely removed the St. Peter. Modified from [74, Map c3stpeter].

geology is complex and can be very different from the overlying St. Peter Sandstone.

We model sequestration in southern Illinois, as shown in Figure 2-27. The data for this region are shown in Table 2.20.

Figure 2-27: We identify two boundaries that constrain the portion of the St. Peter Sandstone in the Illinois Basin that is suitable for sequestration. Boundary 1 corresponds to the end of the available depth and formation thickness maps [74, Maps c1stpeter, c3stpeter]. Boundary 2 corresponds to basin-scale faults [86].

Table 2.20: Parameters for the St. Peter Sandstone.

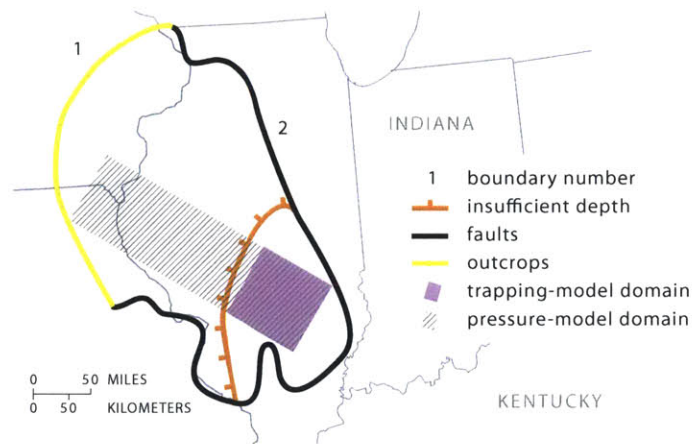| Parameter	Symbol	Value	Data Source	Reference
Residual CO_2 saturation	S_{rg}	0.3	estimated	[18, 130]
Connate water saturation	S_{wc}	0.4	estimated	[18, 130]
Endpoint relative permeability to CO_2	k_{rg}^*	0.6	estimated	[18, 130]
Coefficient of CO_2-saturated-brine flux	α	0.01	estimated	[87, 138]
Compressibility (GPa^{-1})	c	0.1	estimated	[160, Table C1]
Undrained Poisson ratio	ν	0.3	estimated	[160, Table C1]
Geothermal gradient (°C/km)	G_T	20	aquifer data	[91, 119]
Surface temperature (°C)	T_s	10	aquifer data	[3]
Depth to top of aquifer (m)	D	2000	aquifer data	[74, Map c1stpeter]
Depth from aquifer to bedrock (m)	B	1000	aquifer data	[74, Map c1stpeter][56]
Net aquifer thickness (m)	H	40	aquifer data	[74, Map c1stpeter]
Length of trapping-model domain (km)	L_T	100	aquifer data	Fig. 2-27
Length of pressure-model domain (km)	L_{pres}	400	aquifer data	Fig. 2-27
Width of well array (km)	W	100	aquifer data	Fig. 2-27
Porosity	ϕ	0.06	calculated	[71]
Caprock slope (degrees)	ϑ	0.5	calculated	[74, Map c1stpeter]
Darcy velocity (cm/yr)	U	1	calculated	[108, Fig.27C]
Aquifer permeability (mD)	k_{aq}	50[a]	aquifer data	[108, Fig.19C]
Mean vertical permeability (mD)	k_{cap}	0.01	estimated	[124, 153, 37]
Lateral overburden permeability (mD)	$\bar{k}_x$	30	calculated	Fig. 2-8
Vertical overburden permeability (mD)	$\bar{k}_z$	0.02	calculated	Fig. 2-8
Salinity (ppm)	s	100000	aquifer data	[111, Fig.13]
CO_2 solubility (volume fraction)	χ_v	0.05	calculated	[107, 42]
Brine density (kg/m^3)	ρ_w	1000	calculated	[16]
CO_2 density (kg/m^3)	ρ_g	800	calculated	[25]
Brine density change from diss. (kg/m^3)	$\Delta\rho_d$	8	calculated	[60, 9]
Brine viscosity (mPa s)	μ_w	1	calculated	[16]
CO_2 viscosity (mPa s)	μ_g	0.07	calculated	[25]
Fracture pressure (MPa)	P_{frac}	30	calculated	Eq. 2.29,2.28; [173]

[a] We calculate permeability from mapped values of hydraulic conductivity (40 to 190 m/yr [108, Fig.19C]). To convert to permeability, we assume a density of 1000 kg/m^3 and a viscosity of 0.5 mPa s.

| a. depth to top of the aquifer | b. thickness |
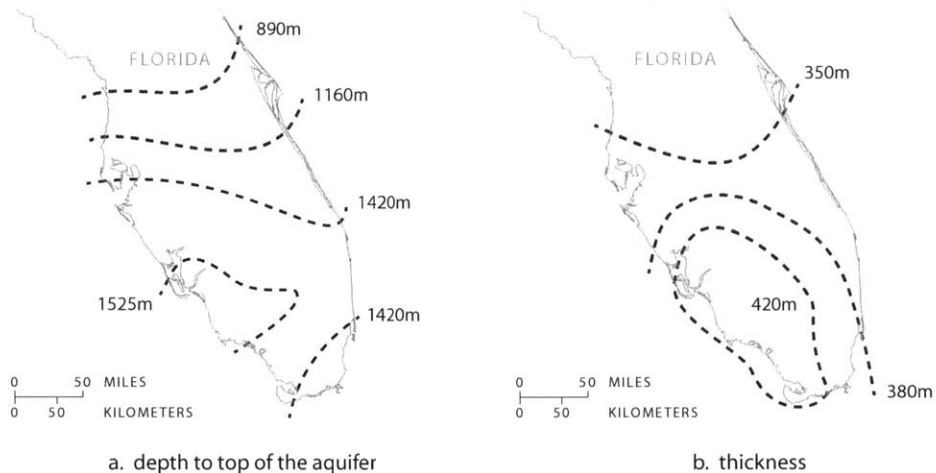
Figure 2-28: The Cedar Keys and Lawson Dolomites deepen and thicken toward the southwestern part of the Florida peninsula. (a) Modified from [74, Map c1cedarkey]. (b) Modified from [74, Map c3cedarkeyg].

Cedar Keys and Lawson Dolomites

The Lawson Formation and lower Cedar Keys Formation occur in Florida in the South Florida Basin. The depth to the top of these rocks and their thickness is shown in Figure 2-28.

The Lawson Formation consists of two members [4, Table 1]. Its lower member is mostly white chalk that is irregularly interbedded with chalky dolomite or dolomitic chalk. Its upper member is finely to coarsely crystalline dolomite that contains gypsum and anhydrite [5, p.G26-G27]. The Lawson Formation overlies unnamed carbonate beds of Taylor age. Over the Florida peninsula, these beds consist mostly of chalky dolomite interbedded with few beds of shale or marlstone [4]. We choose these beds to be the bottom boundary in our model since we found almost no information about them.

The Lawson Formation is unconformably overlain by the lower Cedar Keys Formation, which consists of limestone [5]. It is overlain by the middle Cedar Keys Formation, which consists of massively bedded anhydrite [76, p.72]. These anhydrite beds are nearly impermeable and are the caprock in our study [114].

We model sequestration in the center of the Florida peninsula, as shown in Figure S25. The data for this region is shown in Table 2.21.

83
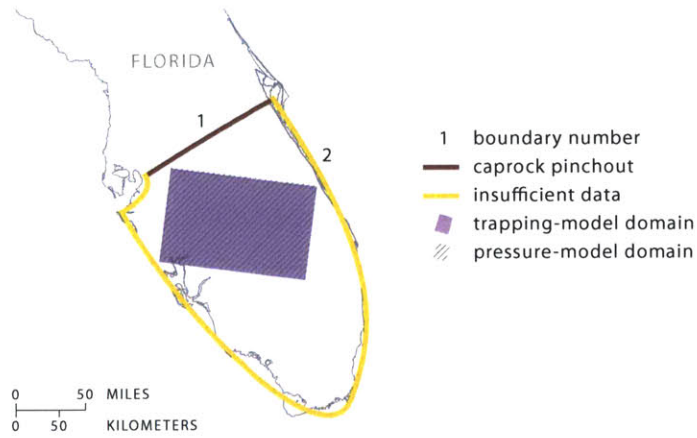
Figure 2-29: We identify 2 boundaries that constrain the portion of the Cedar Keys and Lawson Dolomites that is suitable for sequestration. Boundary 1 corresponds to the limit of the caprock for the overlying Floridan Aquifer. While maps show that the middle Cedar Keys Formation, which we take as the caprock in this study, does not pinchout here, we put a boundary for safety since the maps are likely very inaccurate [75]. Boundary 2 corresponds to the edges of the reservoir depth and thickness maps [74, Maps c1cedarkey, c3cedarkeyg].

Table 2.21: Parameters for the Cedar Keys and Lawson Dolomites.

Parameter	Symbol	Value	Data Source	Reference
Residual CO_2 saturation	S_{rg}	0.3	estimated	[18, 130]
Connate water saturation	S_{wc}	0.4	estimated	[18, 130]
Endpoint relative permeability to CO_2	k_{rg}^*	0.6	estimated	[18, 130]
Coefficient of CO_2-saturated-brine flux	α	0.01	estimated	[87, 138]
Compressibility (GPa^{-1})	c	0.1	estimated	[160, Table C1]
Undrained Poisson ratio	ν	0.3	estimated	[160, Table C1]
Geothermal gradient (°C/km)	G_T	20	aquifer data	[91, 119]
Surface temperature (°C)	T_s	20	aquifer data	[3]
Depth to top of aquifer (m)	D	2000	aquifer data	[74, Map c1cedarkey]
Depth from aquifer to bedrock (m)	B	2000	aquifer data	[56][74]
Net aquifer thickness (m)	H	400	aquifer data	[74, Map c3cedarkeyg]
Length of trapping-model domain (km)	L_T	100	aquifer data	Fig. S25
Length of pressure-model domain (km)	L_{pres}	100	aquifer data	Fig. S25
Width of well array (km)	W	200	aquifer data	Fig. S25
Porosity	ϕ	0.2	aquifer data	[76]
Caprock slope (degrees)	ϑ	0.2	calculated	[74, Map c1cedarkey]
Darcy velocity (cm/yr)	U	0	estimated	
Aquifer permeability (mD)	k_{aq}	10	aquifer data	[76]
Mean vertical permeability (mD)	k_{cap}	0.01	estimated	[124, 153, 37]
Lateral overburden permeability (mD)	$\overline{k}_x$	5	calculated	Fig. 2-8
Vertical overburden permeability (mD)	$\overline{k}_z$	0.02	calculated	Fig. 2-8
Salinity (g/L)	s	100	aquifer data	[76]
CO_2 solubility (volume fraction)	χ_v	0.05	calculated	[42]
Brine density (kg/m^3)	ρ_w	1000	calculated	[16]
CO_2 density (kg/m^3)	ρ_g	800	calculated	[25]
Brine density change from diss. (kg/m^3)	$\Delta\rho_d$	8	calculated	[60, 9]
Brine viscosity (mPa s)	μ_w	0.7	calculated	[16]
CO_2 viscosity (mPa s)	μ_g	0.07	calculated	[25]
Fracture pressure (MPa)	P_{frac}	30	calculated	Eq. 2.29,2.28; [173]

2.6.6 Sensitivity analysis

Because hydrogeologic data for saline aquifers are highly uncertain, we analyze the sensitivity of both the migration model and the pressure model to variations in their input parameters. We calculate the relative sensitivity of the capacity of an aquifer C to a parameter $\mathcal{P}$ as:

$$\widetilde{S} = \frac{\mathcal{P}_0}{C_0} \frac{\partial C}{\partial \mathcal{P}}\bigg|_{\mathcal{P}_0},\tag{2.30}$$

where $\mathcal{P}_0$ is the baseline value of the parameter and C_0 is the baseline capacity. The baseline for each aquifer is the set of parameter values given in the appropriate preceding section (*e.g.*, Table S22) and the corresponding capacity (Table S23). For the pressure model, the baseline values and the sensitivities depend on the injection time. We assess the sensitivity for each aquifer at three different injection times—$T = 50, 100,$ and 150 years—to define three baselines. These injection times bracket the key time horizon in our study, 100 years.

For both the migration model and the pressure model, the relative sensitivities vary between -1 and 2 within individual aquifers, indicating the relative importance of some parameters over others. For example, the migration model is highly sensitive to the width of the well array, W, the length of the model domain, L, and the aquifer thickness thickness, H—key parameters for calculating an aquifer's pore volume—but is relatively insensitive to the aquifer permeability, k_{aq}. The pressure model is highly sensitive to the aquifer depth, D, and the average density of the overburden, $\overline{\rho_o}$—two key parameters for calculating the fracture pressure—but is relatively insensitive to salinity, s. All sensitivities for the migration model are listed in Table 2.22; all sensitivities for the pressure model are listed in Table 2.23.

2.6.7 Uncertainty analysis

Uncertainty in input parameters

To quantify uncertainty in the hydrogeologic properties of an aquifer, we estimate a low and high value for each input parameter using one of three methods. This is a simplification of hydrogeologic uncertainty, since in reality each parameter would be associated with a probability density function (PDF) of possible values. We use this simplified approach here because detailed PDFs are not available.

We estimate the low and high values of each parameter using one of three methods.

For some parameters, such as surface temperature and geothermal gradient, we estimate an absolute uncertainty $\Delta\mathcal{P}$ and apply it symmetrically about the baseline value, so that the low and high values of a parameter $\mathcal{P}$ with baseline value $\mathcal{P}_0$ will be $\mathcal{P}_{\text{low}} = \mathcal{P}_0 - \Delta\mathcal{P}/2$ and $\mathcal{P}_{\text{high}} = \mathcal{P}_0 + \Delta\mathcal{P}/2$, respectively (Table 2.25). For other parameters, such as aquifer depth and thickness, we estimate a relative uncertainty ψ and apply it symmetrically about the baseline value, so that the low and high values will be $\mathcal{P}_{\text{low}} = (1 - \psi/2)\mathcal{P}_0$ and $\mathcal{P}_{\text{high}} = (1 + \psi/2)\mathcal{P}_0$, respectively (Table 2.26). The remaining parameters—the groundwater velocity, compressibility, and permeability of the aquifer and caprock—are often assumed to be log-normally distributed, so we estimate a relative uncertainty Ψ in the log of the parameter. The corresponding low and high values will then be $\mathcal{P}_{\text{low}} = \mathcal{P}_0^{1+\Psi/2}$ and $\mathcal{P}_{\text{high}} = \mathcal{P}_0^{1-\Psi/2}$. We take the relative uncertainty in the log to be $\Psi = 0.03$ for all of these log-normally distributed parameters.

Uncertainty in capacity

Uncertainty in the hydrogeologic properties of an aquifer leads to uncertainty in its storage capacity. We using the low, baseline, and high values of each parameter estimated in the previous section to calculate the uncertainty in each aquifer's storage capacity with two different methods.

In the Extrema Method, we calculate low and high values of the capacity by choosing the set of parameter values that will give the lowest capacity and the set that will give the highest capacity. To do so, we choose either the low or high value of each parameter as driven by the sensitivity analysis: to calculate the high capacity, for example, we take the high value of all parameters to which the capacity has a positive sensitivity, and the low value of all parameters to which the capacity has a negative sensitivity.

In the PDF Method, we generate a PDF for the capacity by estimating the capacity for every possible combination of the low, baseline, and high values of the parameters. The uncertainty in the capacity is then the standard deviation of this PDF. Since using the migration and pressure models to calculate the capacity for every parameter combination is computationally infeasible, we instead extrapolate the capacity for each combination using the sensitivity analysis:

$$C = C_0 + \widetilde{S}_{\mathcal{P}1}\Delta\mathcal{P}_1 + \widetilde{S}_{\mathcal{P}2}\Delta\mathcal{P}_2 + \widetilde{S}_{\mathcal{P}3}\Delta\mathcal{P}_3 + \ldots, \tag{2.31}$$
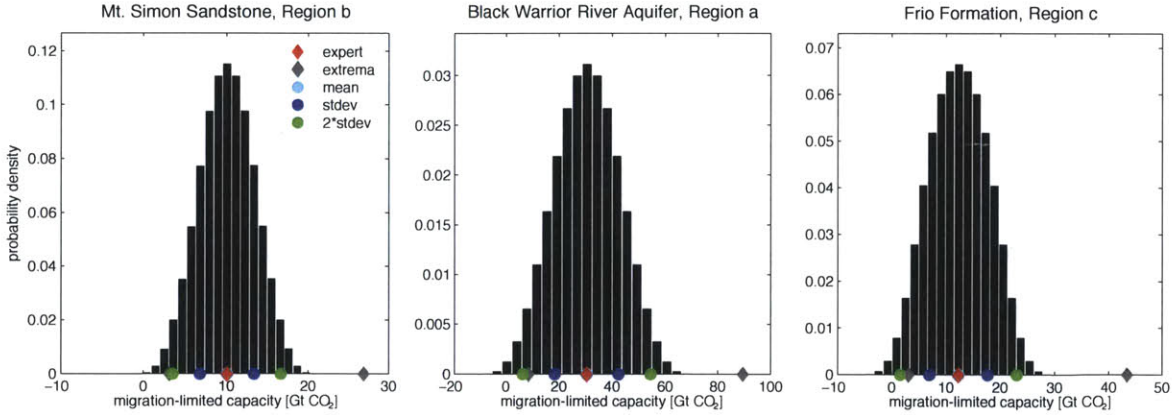
Figure 2-30: Approximate probability density functions for the migration-limited capacity of three well arrays.

where the $\Delta \mathcal{P}_i = \mathcal{P}_i - \mathcal{P}_{i,0}$, $i = 1 \ldots N$, are the uncertainties in the N input parameters and $\widetilde{S}_{\mathcal{P}i}$ are the associated sensitivities. Using Eq. (2.31), we calculate a capacity for every possible combination of the low, baseline, and high values of each parameter for all $N = 16$ input parameters, generating $3^{16} \approx 43 \times 10^6$ values of capacity that compose the approximate PDF of capacity.

We calculate the uncertainties in the migration-limited capacity and the pressure-limited capacity independently. For the migration-limited capacity, the low capacities derived from the Extrema Method, C_l, are about 20–40% of the baseline capacity, and the high capacities, C_h, are about 200–350% of the baseline capacity (Table 2.27). From the PDF Method, the probability density functions are symmetric because the uncertainties in most of the input parameters are symmetric, and those with asymmetric uncertainties (Darcy velocity and permeability) exhibit low sensitivities (Figure 2-30). As a result, the mean capacities from these distributions, $\overline{C}$, are nearly the same as the baseline capacities, C_0. One standard deviation, σ_C, is about $30 - 45\%$ of the baseline capacity, and the upper end of the uncertainty window calculated from one standard deviation—$\overline{C} + \sigma_C$—is then about 130 to 145% of the baseline capacity (Table 2.27).

We use one standard deviation as the appropriate measure of uncertainty from the PDF Method for both migration-limited and pressure-limited capacities. We do not use two standard deviations because the uncertainty window derived from two standard deviations is typically large to the point of being meaningless: for most of the well arrays, the lower end of the uncertainty window is below the low capacity from the Extrema Method, and in at least one case goes to zero (Figures 2-31 & 2-33). Indeed, the approximate probability density
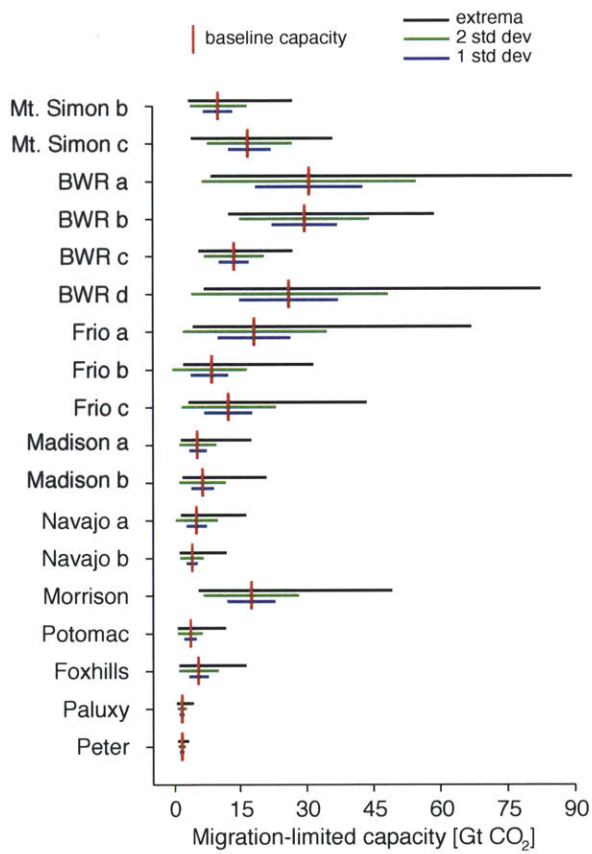
Figure 2-31: The baseline migration-limited capacity and three measures of uncertainty for nearly all the well arrays in the study. We do not show Mt. Simon, Region a or Cedar Keys because their baseline capacities and uncertainties are so large that the data for other aquifers becomes obscured.

functions from which they are calculated often reach into negative capacities, indicating that the lower ends of the uncertainty windows derived from them are also too low (Figures 2-30 & 2-32). The upper ends of the uncertainty windows are likely also too low, since the high capacity from the Extrema Method suggests that the true probability density function is skewed to the right.

For the pressure-limited capacity, the low capacities derived from the Extrema Method are generally 30% of the baseline capacity, and the high capacities are generally 300 to 400% of the baseline capacity (Table 2.28). Compared with the migration-limited capacity, the high capacities are typically a larger fraction of the baseline capacity because the pressure model has more input parameters with large uncertainty, such as the compressibility and caprock permeability, and is more sensitive to the shared parameters with large uncertainties, such as the aquifer permeability. These parameters with large-uncertainties also have asymmetric uncertainties, and cause the capacity distributions obtained from the PDF Method to be asymmetric and often multi-peaked (Figure 2-32). As a result, the mean capacities from these distributions, $\overline{C}$, are different from the baseline capacities, C_0 (Figure 2-33). One standard deviation, σ_C, is about 50 – 60% of the baseline capacity, leading to error windows that are about 100 – 120% of the baseline capacity (Table 2.28).

We extend the uncertainty results from one injection time to all injection times by prorating. We calculate the high and low capacities from the Extrema Method at all injection times as:

$$C_l(T) = C_0(T)\frac{C_l(100 \text{ yrs})}{C_0(100 \text{ yrs})}, \qquad C_h(T) = C_0(T)\frac{C_h(100 \text{ yrs})}{C_0(100 \text{ yrs})}, \qquad (2.32)$$

where $C_l(T)$ and $C_h(T)$ are the low and high capacities at any injection time, T, respectively; $C_l(100 \text{ yrs})$ and $C_h(100 \text{ yrs})$ are the low and high capacities for an injection time of 100 years, respectively; and $C_0(100 \text{ yrs})$ is the baseline capacity for an injection time of 100 years. We choose to prorate based on the results at 100 years because that is the important time horizon in our study; the results obtained by prorating from an average of the results at 50, 100, and 150 years are extremely similar. We calculate the uncertainty window from the PDF Method at all injection times as:

$$C_{\mp\sigma}(T) = C_0(T)\frac{\overline{C}(100 \text{ yrs}) \mp \sigma_C(100 \text{ yrs})}{C_0(100 \text{ yrs})}, \qquad (2.33)$$

90
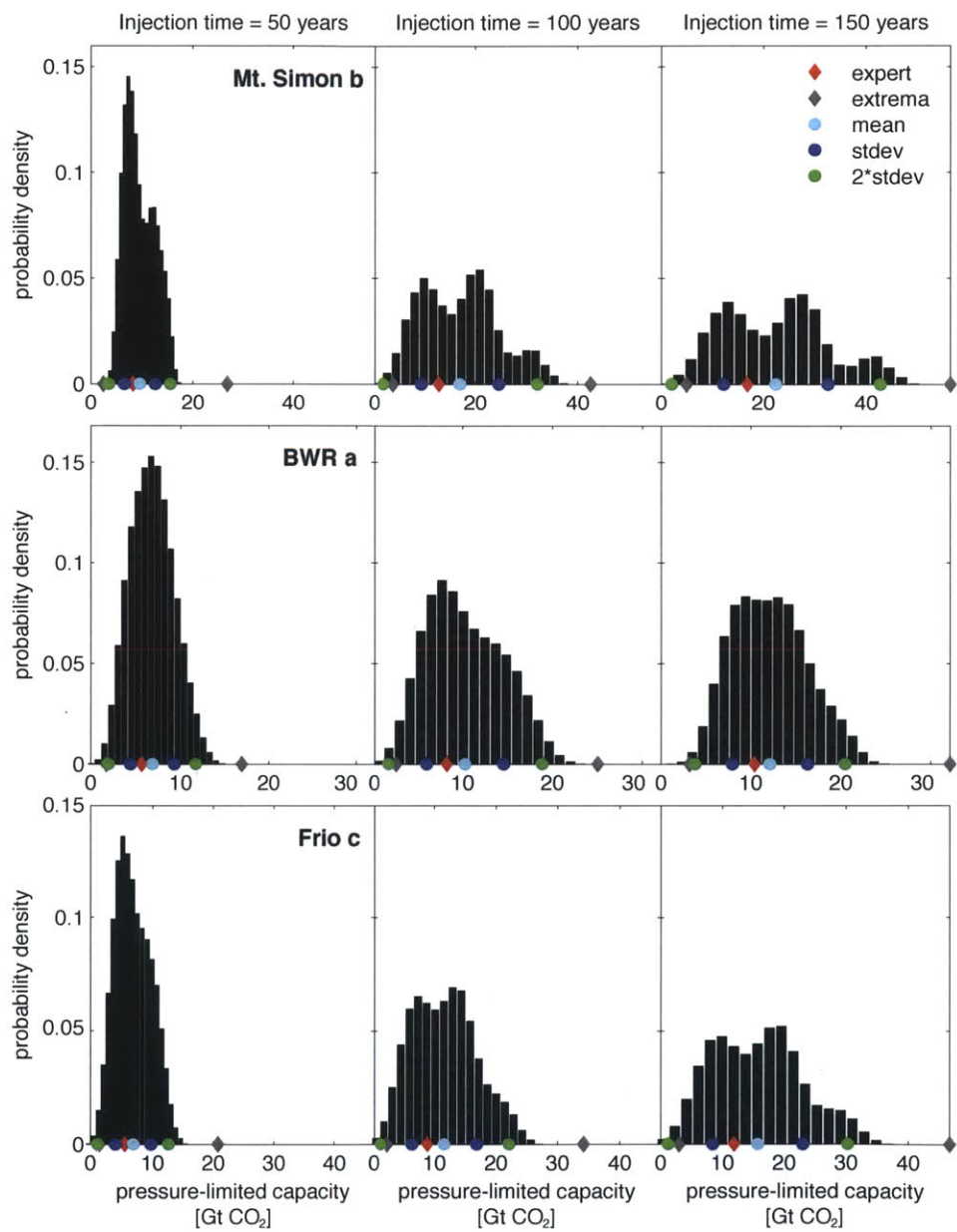
Figure 2-32: Approximate probability density functions for the pressure-limited capacity of three well arrays.
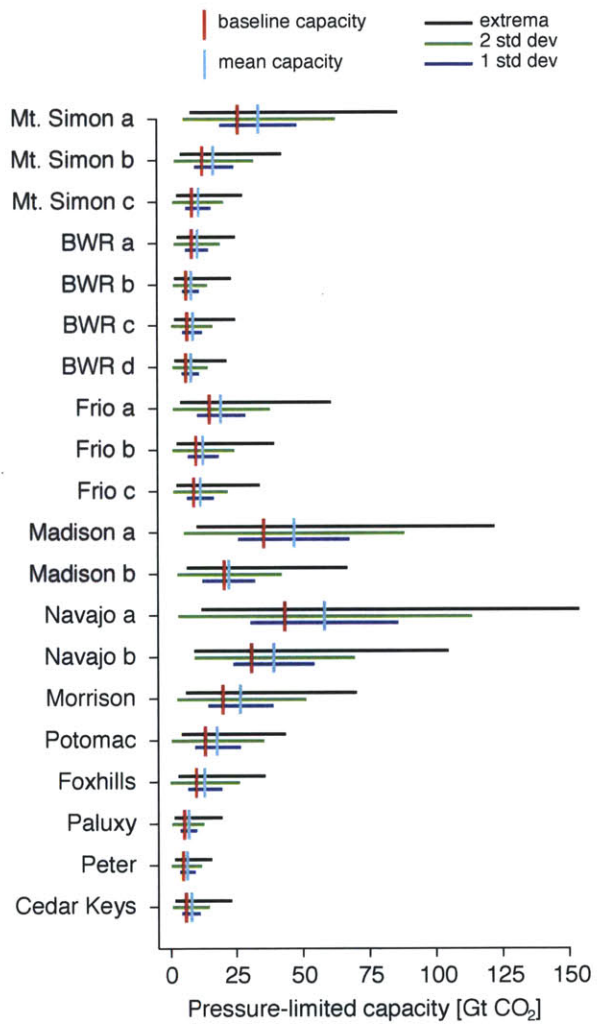
Figure 2-33: The baseline and mean pressure-limited capacity with three measures of uncertainty for all well arrays.
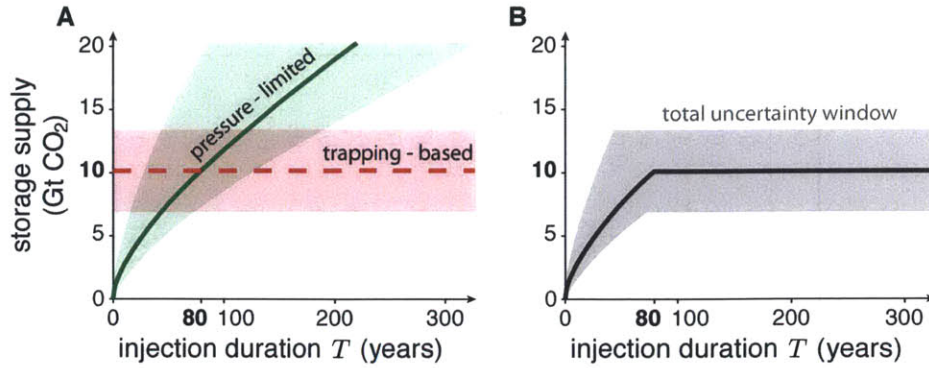
Figure 2-34: (**A**) The migration-limited and pressure-limited capacity for Region b of the Mt. Simon Sandstone, with uncertainty windows based on one standard deviation of the approximate PDF. (**B**) The total uncertainty window combines the uncertainties from both types of capacity. The upper boundary of the window corresponds to the lowermost of the two upper boundaries, and the lower boundary corresponds to the lowermost of the two lower boundaries.

where $C_{-\sigma}(T)$ and $C_{+\sigma}(T)$ are, respectively, the lower and upper ends of the uncertainty window based on one standard deviation at all injection times, T; $\overline{C}(100 \text{ yrs})$ is the mean capacity at an injection time of 100 years; and $\sigma_C(100 \text{ yrs})$ is the standard deviation at an injection time of 100 years.

To construct the complete uncertainty window for a particular aquifer, we combine the uncertainties from the migration-limited and pressure-limited capacities, as shown in Figure 2-34. To construct the complete uncertainty window for the entire US storage supply, we combine the uncertainties from all the aquifers.

Table 2.22: Sensitivity of the migration model to its input parameters.

Reservoir		W	H	D	T_s	G	$\overline{\rho_w}$	s	k_{aq}	ϕ	S_{wc}	S_{gr}	k^*_{gr}	α	θ	U	L_T
Mt. Simon	a	1	0.49	0.71	0.1	-0.75	0.19	-0.73	0	1	-0.097	0.87	-0.85	0.54	-0.46	0	1.6
Mt. Simon	b	1	0.64	0.72	0.094	-0.53	0.17	-0.78	0.021	1	0.12	1.2	-0.82	0.37	-0.31	-0.021	1.4
Mt. Simon	c	1	1	0.74	0.17	-0.51	0.0052	-0.15	0.0071	1	-0.49	0.0086	-0.93	0	0.0071	0.17	1
BWR	a	1	0.77	0.77	0.19	-2.1	0.054	-0.34	0	1	0.44	1.7	-0.89	0.2	-0.2	0	1.2
BWR	b	1	0.88	0.56	0.14	-0.73	0.061	-0.069	0	1	-0.51	0.068	-0.76	0.069	-0.1	-0.013	1.1
BWR	c	1	0.91	0.46	0.14	-0.7	0.034	-0.028	0	1	-0.64	0.031	-0.92	-0.018	-0.078	0	0.98
BWR	d	1	0.94	0.73	0.22	-1.6	0.032	-0.18	0	1	0.65	2	-0.86	0.084	-0.056	0	1.1
Frio	a	1	0.99	1.7	0.27	-1.1	-0.0058	-0.14	0.0044	1	0.71	2.1	-0.77	0.014	-0.031	0	1
Frio	b	1	0.94	1.7	0.23	-1.2	0.025	-0.15	0	1	0.69	2.1	-0.76	0.038	-0.059	0	1
Frio	c	1	1	1.2	0.22	-1	0.011	-0.15	0.0012	1	0.72	2.1	-0.84	0.015	0.0091	0.0013	1
Madison	a	1	0.92	1.2	0.047	-0.59	0.064	-0.25	0.0067	1	0.6	1.9	-0.82	0.075	-0.067	-0.0013	1.1
Madison	b	1	0.78	1.5	-0.012	-0.75	0.15	-0.44	-0.017	1	0.53	1.7	-1	0.14	-0.16	-0.086	1.1
Nav.-Nug.	a	1	0.78	0.98	-0.035	-0.48	-0.034	-0.15	0	1	0.61	1.9	-0.83	0.13	-0.2	0	1.1
Nav.-Nug.	b	1	0.67	1.1	0.077	-0.54	0.22	-0.21	0	1	0.28	1.4	-0.76	0.36	-0.3	0	1.4
Morrison		1	0.56	1	0.085	-0.83	0.18	-0.056	0	1	0.1	1.2	-0.81	0.43	-0.4	0	1.5
Potomac		1	0.53	2.6	0.11	-2.3	0.17	-0.039	-0.0082	1	0.0031	1	-0.89	0.47	-0.44	0.011	1.5
Fox Hills		1	0.54	2.6	0.11	-2.3	0.16	-0.012	0	1	0.011	1	-0.88	0.46	-0.42	0	1.5
Paluxy		1	0.39	1.3	0.089	-1	0.52	-0.72	0	1	-0.31	0.54	-0.84	0.62	-0.55	0	1.7
St. Peter		1	0.89	0.26	0.073	-0.39	0.053	-0.29	0	1	-0.12	0.37	-0.66	0.036	-0.1	0	1
Cedar Keys		1	0.64	0.64	0.13	-0.5	0.17	-0.43	0	1	-0.36	0.31	-0.69	0.25	-0.33	0	1.3

Table 2.23: Sensitivity of the pressure model to its input parameters for three different injection times. Reservoirs: Mt. Simon through Frio.

Reservoir	Region	T (years)	W	H	D	T_s	G	$\overline{\rho_w}$	s	k_{aq}	k_{cap}	c	ν	$\overline{\rho_o}$	B	L_{Pmin}	L_{Pmax}
Mt. Simon	a	50	1	0.64	1.4	0.11	-0.027	-0.77	-0.16	0.5	0.18	0.32	0	1.8	0	0	0
		100	1	0.58	1.4	0.11	-0.013	-0.77	-0.17	0.5	0.21	0.29	0	1.8	0	0	0
		150	1	0.55	1.4	0.12	-0.0025	-0.77	-0.18	0.5	0.23	0.26	0	1.8	0	0	0
Mt. Simon	b	50	1	0.48	1.5	0.099	0.085	-0.77	-0.24	0.5	0.26	0.24	0	1.8	0	0	0
		100	1	0.41	1.5	0.1	0.092	-0.77	-0.25	0.5	0.3	0.2	0	1.8	0	0	0
		150	1	0.38	1.5	0.11	0.1	-0.77	-0.26	0.5	0.32	0.18	0	1.8	0	0	0
Mt. Simon	c	50	1	0.48	1.4	0.12	-0.049	-0.77	-0.26	0.5	0.26	0.24	0	1.8	0	0.00071	0
		100	1	0.43	1.4	0.12	-0.037	-0.77	-0.27	0.5	0.29	0.22	0	1.8	0	0.0075	0
		150	1	0.41	1.4	0.13	-0.027	-0.77	-0.26	0.5	0.32	0.21	0	1.8	0	0.025	0
Black Warrior River	a	50	1	0.77	1.3	0.17	-0.79	-0.77	-0.1	0.32	0.12	0.38	1.4	1.8	0	0	0
		100	1	0.73	1.1	0.12	-0.84	-0.77	-0.11	0.5	0.18	0.31	1.4	1.8	0	0	0
		150	1	0.68	0.87	0.081	-1.3	-0.77	-0.12	0.6	0.24	0.25	1.4	1.8	0	0	0
Black Warrior River	b	50	1	0.57	1.4	0.26	-0.18	-0.77	-0.032	0.46	0.23	0.27	1.4	1.8	0	0.038	0
		100	1	0.48	1.3	0.28	-0.15	-0.77	-0.035	0.4	0.3	0.2	1.4	1.8	0	0.097	-0.00087
		150	1	0.43	1.3	0.3	-0.13	-0.77	-0.038	0.37	0.36	0.14	1.4	1.8	0	0.13	-0.0033
Black Warrior River	c	50	1	0.46	1.4	0.26	-0.16	-0.77	-0.0061	0.49	0.28	0.23	1.4	1.8	0	0.023	0.027
		100	1	0.42	1.3	0.26	-0.17	-0.77	-0.0066	0.46	0.36	0.17	1.4	1.8	0	0.067	0.06
		150	1	0.39	1.2	0.26	-0.16	-0.77	-0.0072	0.45	0.43	0.12	1.4	1.8	0	0.097	0.079
Black Warrior River	d	50	1	0.79	1.4	0.16	-0.61	-0.77	-0.086	0.5	0.11	0.39	1.4	1.8	0	0	0
		100	1	0.73	1.4	0.17	-0.59	-0.77	-0.092	0.5	0.15	0.35	1.4	1.8	0	0	0
		150	1	0.68	1.4	0.18	-0.57	-0.77	-0.098	0.5	0.19	0.31	1.4	1.8	0	0	0
Frio	a	50	1	0.7	2.1	0.18	-0.52	-0.77	-0.092	0.56	0.15	0.29	1.4	1.8	0	0	-0.18
		100	1	0.67	2.1	0.18	-0.45	-0.77	-0.094	0.62	0.17	0.21	1.4	1.8	0	0	-0.36
		150	1	0.66	2.2	0.19	-0.41	-0.77	-0.095	0.66	0.17	0.17	1.4	1.8	0	0	-0.47
Frio	b	50	1	0.59	2.1	0.19	-0.51	-0.77	-0.099	0.54	0.2	0.26	1.4	1.8	0	0	-0.12
		100	1	0.55	2.1	0.2	-0.45	-0.77	-0.1	0.59	0.22	0.18	1.4	1.8	0	0	-0.27
		150	1	0.54	2.1	0.2	-0.41	-0.77	-0.1	0.62	0.23	0.15	1.4	1.8	0	0	-0.36
Frio	c	50	1	0.51	1.8	0.19	-0.4	-0.77	-0.14	0.5	0.14	0.25	1.4	1.8	0	0	-0.00064
		100	1	0.47	1.8	0.19	-0.38	-0.77	-0.14	0.5	0.28	0.22	1.4	1.8	0	0	-0.011
		150	1	0.45	1.8	0.2	-0.36	-0.77	-0.15	0.51	0.31	0.18	1.4	1.8	0.00048	0	-0.032

Table 2.24: Sensitivity of the pressure model to its input parameters for three different injection times. Reservoirs: Madison through Cedar Keys.

Reservoir	Region	T (years)	W	H	D	T_s	G	$\overline{\rho_w}$	s	k_{aq}	k_{cap}	c	ν	$\overline{\rho_o}$	B	L_{Pmin}	L_{Pmax}
Madison	a	50	1	0.53	1.8	0.041	-0.031	-0.77	-0.13	0.49	0.23	0.27	0	1.8	0.0013	0	0.0042
		100	1	0.45	1.8	0.042	-0.0052	-0.77	-0.14	0.5	0.26	0.24	0	1.8	0.015	0	0.031
		150	1	0.4	1.8	0.043	-0.00027	-0.77	-0.14	0.5	0.26	0.24	0	1.8	0.036	0.00064	0.061
Madison	b	50	1	0.46	1.1	0.056	-0.93	-0.77	-0.15	-0.35	0.26	0.23	0	1.8	0.011	0	0
		100	1	0.39	1.1	0.057	-0.89	-0.77	-0.15	-0.32	0.27	0.22	0	1.8	0.06	0	0
		150	1	0.36	1.1	0.057	-0.86	-0.77	-0.15	-0.29	0.27	0.22	0	1.8	0.1	0	0
Navajo-Nugget	a	50	1	0.32	1.9	0.056	0.26	-0.77	-0.13	0.5	0.34	0.16	0	1.8	0	0	0.00044
		100	1	0.28	1.9	0.057	0.27	-0.77	-0.13	0.5	0.36	0.14	0	1.8	0	0	0.0093
		150	1	0.27	1.9	0.058	0.27	-0.77	-0.13	0.49	0.37	0.14	0	1.8	0	0	0.028
Navajo-Nugget	b	50	1	0.43	1.6	0.087	0.005	-0.77	-0.12	0.33	0.29	0.21	0	1.8	0.14	0	0
		100	1	0.43	1.6	0.087	0.0047	-0.77	-0.12	0.33	0.28	0.22	0	1.8	0.22	0	0
		150	1	0.43	1.6	0.087	0.0044	-0.77	-0.12	0.34	0.29	0.21	0	1.8	0.26	0.00028	0.00055
Morrison		50	1	0.36	1.8	0.11	0.063	-0.77	-0.031	0.5	0.3	0.2	0	1.8	0.041	0.16	0
		100	1	0.31	1.9	0.11	0.061	-0.77	-0.03	0.5	0.3	0.2	0	1.8	0.11	0.26	0
		150	1	0.27	1.9	0.11	0.065	-0.77	-0.031	0.5	0.3	0.2	0	1.8	0.15	0.32	0.00067
Potomac		50	1	0.43	2.4	0.15	-1.3	-0.77	-0.022	0.29	0.32	0.39	0	1.8	0	0.2	0.4
		100	1	0.31	2.2	0.17	-1.3	-0.77	-0.026	0.26	0.47	0.27	0	1.8	0	0.24	0.48
		150	1	0.24	2.1	0.19	-1.3	-0.77	-0.029	0.25	0.57	0.18	0	1.8	0	0.25	0.49
Fox Hills		50	1	0.36	2.6	0.15	-1.1	-0.77	-0.011	0.5	0.34	0.16	0	1.8	0	0.67	0
		100	1	0.36	2.7	0.16	-1.1	-0.77	-0.012	0.5	0.39	0.11	0	1.8	0	0.65	0.00075
		150	1	0.37	2.7	0.17	-1.1	-0.77	-0.012	0.5	0.42	0.08	0	1.8	0	0.63	0.0036
Paluxy		50	1	0.27	1.7	0.16	-0.13	-0.77	-0.21	0.47	0.36	0.15	1.4	1.8	0	0.025	0.028
		100	1	0.24	1.7	0.17	-0.14	-0.77	-0.23	0.44	0.38	0.15	1.4	1.8	0	0.072	0.06
		150	1	0.23	1.7	0.17	-0.15	-0.77	-0.23	0.42	0.4	0.16	1.4	1.8	0.00051	0.11	0.081
St. Peter		50	1	0.27	1.4	0.15	0.046	-0.77	-0.16	0.5	0.36	0.14	0	1.8	0.0022	0	0
		100	1	0.24	1.4	0.15	0.049	-0.77	-0.16	0.5	0.37	0.13	0	1.8	0.017	0.00012	0
		150	1	0.23	1.4	0.15	0.049	-0.77	-0.16	0.5	0.37	0.13	0	1.8	0.035	0.0015	0
Cedar Keys		50	1	0.5	1.4	0.19	0.051	-0.77	-0.13	0.5	0.25	0.25	1.4	1.8	0	0	0
		100	1	0.45	1.4	0.2	0.063	-0.77	-0.13	0.5	0.27	0.23	1.4	1.8	0.00079	0	0
		150	1	0.43	1.4	0.2	0.069	-0.77	-0.14	0.5	0.28	0.22	1.4	1.8	0.0037	0	0

Table 2.25: Parameters for which we estimate an absolute uncertainty, and corresponding absolute uncertainties $\Delta\mathcal{P}$.

Parameter	Symbol	$\Delta\mathcal{P}$
Connate water saturation [−]	S_{wc}	0.2
Residual CO_2 saturation [−]	S_{gr}	0.2
Endpoint relative permeability to CO_2 [−]	k_{gr}^*	0.2
Coefficient of CO_2-saturated-brine flux [−]	α	0.002
Average density of water in overburden [kg/m^3]	$\overline{\rho_w}$	20
Average density of overburden [kg/m^3]	$\overline{\rho_o}$	230
Surface temperature [°C]	T_s	1
Geothermal gradient [°C/km]	G	2

Table 2.26: Parameters for which we estimate a relative uncertainty, and corresponding relative uncertainties $\psi = \Delta\mathcal{P}/\mathcal{P}$.

Parameter	Symbol	ψ
Depth to top of aquifer	D	0.2
Depth from aquifer to bedrock	B	0.2
Net aquifer thickness	H	0.2
Width of well array	W	0.1
Length of model domain	L_t	0.1
Distance from well array to closest pressure boundary	L_{Pmin}	0.1
Distance from well array to farthest pressure boundary	L_{Pmax}	0.1
Porosity	ϕ	0.4
Caprock slope	ϑ	0.2
Salinity	s	0.1

Table 2.27: Uncertainty in migration-limited capacity.

Reservoir	Region	C_0	$\overline{C}$	$\frac{\overline{C}-C_0}{C_0}$	σC	$\frac{\sigma_C}{C_0}$	C_l	$\frac{C_l-C_0}{C_0}$	C_h	$\frac{C_h-C_0}{C_0}$
Mt. Simon	a	88	88	0	27	0.31	29	-0.67	250	1.8
Mt. Simon	b	10	10	0	3.3	0.32	3.1	-0.69	27	1.7
Mt. Simon	c	17	17	0.027	4.8	0.28	3.8	-0.77	36	1.1
Black Warrior River	a	31	31	0	12	0.39	8.6	-0.72	89	1.9
Black Warrior River	b	30	30	0	7.3	0.25	12	-0.58	59	0.99
Black Warrior River	c	14	14	0	3.4	0.25	5.7	-0.58	27	0.97
Black Warrior River	d	26	26	0	11	0.43	6.9	-0.73	82	2.2
Frio	a	18	18	0	8.1	0.45	4.3	-0.77	67	2.7
Frio	b	8.6	8	-0.075	4.3	0.5	2	-0.76	32	2.7
Frio	c	12	12	0	5.4	0.44	3.1	-0.75	44	2.5
Madison	a	5.3	5.4	0.015	2.1	0.4	1.4	-0.73	18	2.3
Madison	b	6.6	6.4	-0.016	2.7	0.41	1.8	-0.72	21	2.2
Navajo-Nugget	a	5.1	5.1	0	2.4	0.48	1.4	-0.72	16	2.2
Navajo-Nugget	b	4	4	0	1.4	0.35	1.2	-0.7	12	2
Morrison		17	17	0	5.3	0.31	5.7	-0.68	49	1.8
Potomac		3.6	3.6	0.0038	1.5	0.42	0.74	-0.79	12	2.3
Foxhills		5.5	5.5	0	2.3	0.42	1.1	-0.79	16	2
Paluxy		1.5	1.5	0	0.5	0.32	0.47	-0.7	4.4	1.9
St. Peter		1.6	1.6	0	0.38	0.24	0.72	-0.55	3.1	0.97
Cedar Keys		87	87	0	22	0.25	38	-0.57	180	1.1

Table 2.28: Uncertainty in pressure-limited capacity: Mt. Simon through Navajo-Nugget.

Reservoir		T	C_0	$\overline{C}$	$\frac{\overline{C}-C_0}{C_0}$	σ_C	$\frac{\sigma_C}{C_0}$	C_l	$\frac{C_l-C_0}{C_0}$	C_h	$\frac{C_h-C_0}{C_0}$
Mt. Simon	a	50	16	21	0.29	8.8	0.54	4.9	-0.7	53	2.2
		100	26	34	0.3	14	0.55	7.8	-0.7	86	2.3
		150	35	46	0.3	20	0.56	10	-0.7	120	2.3
Mt. Simon	b	50	8.2	11	0.31	4.7	0.57	2.4	-0.7	27	2.3
		100	13	17	0.32	7.6	0.59	3.8	-0.7	43	2.3
		150	17	22	0.33	10	0.61	5	-0.71	56	2.3
Mt. Simon	c	50	4.9	6.4	0.31	2.8	0.57	1.5	-0.7	16	2.3
		100	8.4	11	0.32	4.9	0.59	2.5	-0.71	28	2.3
		150	12	15	0.33	7	0.61	3.4	-0.71	39	2.4
BWR	a	50	5.6	6.8	0.21	2.4	0.43	1.7	-0.69	17	2
		100	8.2	11	0.28	4.5	0.54	2.6	-0.69	25	2
		150	10	14	0.33	6.6	0.63	3.2	-0.69	32	2.1
BWR	b	50	3.7	4.8	0.28	2	0.53	0.98	-0.74	14	2.7
		100	6.2	8	0.29	3.3	0.53	1.6	-0.74	23	2.8
		150	8.5	11	0.3	4.8	0.57	2.2	-0.75	33	2.9
BWR	c	50	3.8	5	0.3	2.2	0.56	1	-0.74	14	2.8
		100	6.6	8.7	0.32	4	0.61	1.7	-0.74	25	2.8
		150	9.1	12	0.34	6	0.66	2.3	-0.75	35	2.9
BWR	d	50	4.3	5.5	0.27	2.4	0.55	1.2	-0.72	15	2.4
		100	6.1	7.9	0.28	3.4	0.56	1.7	-0.73	22	2.6
		150	7.7	10	0.29	4.4	0.56	2.1	-0.73	28	2.6
Frio	a	50	9.2	12	0.27	5.2	0.56	2.3	-0.75	35	2.8
		100	15	20	0.28	9.2	0.6	3.7	-0.76	61	3
		150	21	28	0.28	13	0.62	5	-0.77	87	3
Frio	b	50	5.9	7.5	0.28	3.3	0.57	1.5	-0.75	23	2.8
		100	9.9	13	0.29	6	0.6	2.4	-0.76	40	3
		150	14	18	0.3	8.6	0.62	3.3	-0.76	56	3.1
Frio	c	50	5.5	6.9	0.25	2.9	0.52	1.4	-0.74	21	2.8
		100	8.8	12	0.31	5.2	0.59	2.3	-0.75	34	2.9
		150	12	16	0.32	7.3	0.61	3	-0.75	47	2.9
Madison	a	50	21	28	0.31	12	0.57	6	-0.72	74	2.5
		100	36	47	0.32	21	0.58	9.9	-0.72	120	2.4
		150	48	63	0.32	28	0.59	13	-0.72	160	2.4
Madison	b	50	13	14	0.065	6.5	0.48	3.9	-0.71	44	2.3
		100	21	22	0.077	9.9	0.48	6.1	-0.71	67	2.2
		150	27	29	0.086	12	0.46	7.9	-0.71	86	2.2
Nav.-Nug.	a	50	25	34	0.34	16	0.63	7.1	-0.72	90	2.5
		100	43	58	0.34	28	0.64	12	-0.72	150	2.6
		150	59	80	0.35	38	0.64	16	-0.73	210	2.6
Nav.-Nug.	b	50	18	23	0.27	9.1	0.49	5.2	-0.72	64	2.4
		100	31	39	0.27	15	0.49	8.8	-0.72	100	2.4
		150	41	53	0.27	21	0.5	12	-0.71	140	2.4

Table 2.29: Uncertainty in pressure-limited capacity: Morrison through Cedar Keys.

Reservoir	T	C_0	$\overline{C}$	$\frac{\overline{C}-C_0}{C_0}$	σ_C	$\frac{\sigma_C}{C_0}$	C_l	$\frac{C_l-C_0}{C_0}$	C_h	$\frac{C_h-C_0}{C_0}$
	50	12	16	0.33	7.3	0.6	3.4	-0.72	42	2.5
Morrison	100	20	27	0.33	12	0.6	5.7	-0.72	70	2.5
	150	27	36	0.33	16	0.61	7.6	-0.72	94	2.5
	50	9.5	12	0.29	5.2	0.55	2.9	-0.7	29	2.1
Potomac	100	13	18	0.33	8.8	0.65	4	-0.71	44	2.2
	150	17	24	0.37	13	0.75	4.9	-0.71	58	2.3
	50	5.8	7.8	0.34	3.8	0.65	1.6	-0.72	21	2.6
Fox Hills	100	9.7	13	0.35	6.6	0.68	2.7	-0.73	36	2.7
	150	13	18	0.36	9.4	0.71	3.6	-0.73	50	2.8
	50	2.9	3.8	0.33	1.8	0.62	0.7	-0.76	11	2.9
Paluxy	100	5	6.7	0.33	3.2	0.62	1.2	-0.75	20	2.9
	150	7	9.3	0.33	4.4	0.63	1.7	-0.75	27	2.9
	50	2.5	3.4	0.35	1.6	0.64	0.7	-0.72	8.6	2.5
St. Peter	100	4.5	6.2	0.35	3	0.65	1.3	-0.72	16	2.5
	150	6.5	8.8	0.36	4.2	0.65	1.8	-0.72	22	2.5
	50	3.4	4.5	0.33	2.1	0.61	0.84	-0.75	14	3
Cedar Keys	100	5.8	7.7	0.34	3.6	0.62	1.4	-0.76	23	3
	150	7.9	11	0.34	5	0.63	1.9	-0.76	32	3.1

2.6.8 Synopsis of aquifer data and storage capacities

Tables 2.30 and 2.31 provide a synopsis of aquifer properties and storage capacities.

Table 2.30: General ranges in the input parameters for both the pressure model and the trapping model. For errors in input parameters, see Tables 2.26 & 2.25.

Parameter	Symbol	Value	Data Source	Reference
Residual CO_2 saturation	S_{rg}	0.2 – 0.4	experiments	[18, 130]
Connate water saturation	S_{wc}	0.3 – 0.5	experiments	[18, 130]
Endpoint relative permeability to CO_2	k_{rg}^*	0.5 – 0.7	experiments	[18, 130]
Coefficient of CO_2-saturated-brine flux	α	0.01	estimated	[87, 138]
Compressibility (GPa^{-1})	c	4e-11 – 3e-10	experiments	[160, Table C1]
Undrained Poisson ratio	ν	0.28 – 0.33	experiments	[160, Table C1]
Geothermal gradient (°C/km)	G_T	15 – 40	nationwide data	[91, 119]
Surface temperature (°C)	T_s	0 – 21	nationwide data	[3]
Depth to top of aquifer (m)	D	800 – 3000	nationwide data	see text
Depth from aquifer to bedrock (m)	B	0 – 13,000	nationwide data	[56]
Net aquifer thickness (m)	H	≤ 500	nationwide data	see text
Length of trapping-model domain (km)	L_T	50 – 500	aquifer data	[57]
Length of pressure-model domain (km)	L_{pres}	50 – 500	nationwide data	[57]
Width of well array (km)	W	50 – 500	nationwide data	[57]
Porosity	ϕ	0 – 0.3	nationwide data	[55]
Caprock slope (degrees)	ϑ	0 – 2	nationwide data	see text
Darcy velocity (cm/yr)	U	0 – 10	nationwide data	[23, p.145]
Aquifer permeability (mD)	k_{aq}	10 – 1000	nationwide data	[132, 55]
Mean vertical permeability (mD)	k_{cap}	1e-8 – 1	experiments	[124, 153, 37]
Salinity (g/L)	s	0 – 450	nationwide data	[76]
CO_2 solubility (volume fraction)	χ_v	0.01 – 0.14	$f(T, P, s)$	[42]
Brine density (kg/m^3)	ρ_w	959 – 1130	$f(T, P, s)$	[16]
CO_2 density (kg/m^3)	ρ_g	200 – 800	$f(T, P)$	[25]
CO_2-saturated-brine density (kg/m^3)	ρ_s	969 – 1133	$f(T, P, s, \chi_v)$	[60]
Brine viscosity (mPa s)	μ_w	0.2 – 1.2	$f(T, P, s)$	[16]
CO_2 viscosity (mPa s)	μ_g	0.03 – 0.07	$f(T, P)$	[25]
Fracture pressure (MPa)	P_{frac}	10 – 70	$f(\rho_o, \rho_w, D, \phi)$	Eq. 2.29,2.28; [173]

Table 2.31: Storage capacities for every aquifer we study at different injection times, T. Capacities written in bold are pressure limited; otherwise, they are migration limited.

Reservoir	Region	Storage capacity (Gt CO$_2$) at different injection times, T (years)										
		$T = 25$	50	75	100	150	200	250	300	400	500	600
Mt. Simon	a	$\mathbf{9.4^{+7.9}_{-2.4}}$	$\mathbf{15^{+12}_{-3.7}}$	$\mathbf{19^{+16}_{-4.8}}$	$\mathbf{23^{+20}_{-5.9}}$	$\mathbf{31^{+26}_{-7.8}}$	$\mathbf{37^{+32}_{-9.5}}$	$\mathbf{44^{+37}_{-11}}$	$\mathbf{50^{+42}_{-13}}$	$\mathbf{61^{+52}_{-16}}$	$\mathbf{73^{+43}_{-18}}$	$\mathbf{84^{+32}_{-23}}$
Mt. Simon	b	$\mathbf{4.8^{+4.4}_{-1.3}}$	$7.5^{+5.8}_{-2}$	$9.8^{+3.6}_{-3}$	$10^{+3.3}_{-3.3}$	$10^{+3.3}_{-3.3}$	$10^{+3.3}_{-3.3}$	$10^{+3.3}_{-3.3}$	$10^{+3.3}_{-3.3}$	$10^{+3.3}_{-3.3}$	$10^{+3.3}_{-3.3}$	$10^{+3.3}_{-3.3}$
Mt. Simon	c	$\mathbf{2.7^{+2.5}_{-0.72}}$	$4.5^{+4.1}_{-1.2}$	$6.1^{+5.6}_{-1.6}$	$\mathbf{7.7^{+7}_{-2}}$	$11^{+9.7}_{-2.8}$	$13^{+8.6}_{-3.6}$	$16^{+5.9}_{-4.3}$	$17^{+5.2}_{-4.3}$	$17^{+5.2}_{-4.3}$	$17^{+5.2}_{-4.3}$	$17^{+5.2}_{-4.3}$
Black Warrior River	a	$\mathbf{3.8^{+3.2}_{-1}}$	$5.6^{+4.6}_{-1.5}$	$7^{+5.8}_{-1.9}$	$8.2^{+6.8}_{-2.2}$	$10^{+8.6}_{-2.7}$	$12^{+10}_{-3.3}$	$14^{+12}_{-3.8}$	$16^{+13}_{-4.3}$	$20^{+17}_{-5.3}$	$24^{+19}_{-6.3}$	$28^{+15}_{-9.2}$
Black Warrior River	b	$\mathbf{2.3^{+1.9}_{-0.58}}$	$\mathbf{3.7^{+3.1}_{-0.93}}$	$5.0^{+4.1}_{-1.3}$	$6.2^{+5.1}_{-1.6}$	$8.6^{+7}_{-2.1}$	$11^{+9}_{-2.7}$	$13^{+11}_{-3.3}$	$16^{+13}_{-3.9}$	20^{+17}_{-5}	$25^{+12}_{-6.2}$	$29^{+7.3}_{-7.3}$
Black Warrior River	c	$\mathbf{2.3^{+2.1}_{-0.65}}$	$3.8^{+3.5}_{-1.1}$	$5.2^{+4.8}_{-1.5}$	$6.5^{+6}_{-1.8}$	$8.9^{+8.1}_{-2.5}$	$11^{+5.7}_{-3.2}$	$14^{+3.4}_{-3.4}$	$14^{+3.4}_{-3.4}$	$14^{+3.4}_{-3.4}$	$14^{+3.4}_{-3.4}$	$14^{+3.4}_{-3.4}$
Black Warrior River	d	$\mathbf{3.2^{+2.7}_{-0.87}}$	$4.3^{+3.6}_{-1.2}$	$5.3^{+4.4}_{-1.5}$	$6.1^{+5.1}_{-1.7}$	$7.7^{+6.4}_{-2.1}$	$9.1^{+7.6}_{-2.5}$	$10^{+8.7}_{-2.9}$	$12^{+9.8}_{-3.2}$	$14^{+12}_{-3.9}$	$17^{+14}_{-4.6}$	$19^{+16}_{-5.2}$
Frio	a	$\mathbf{5.9^{+5.2}_{-1.9}}$	$9.2^{+8.1}_{-3}$	12^{+11}_{-4}	$15^{+11}_{-5.3}$	$18^{+8.2}_{-8.1}$	$18^{+8.2}_{-8.1}$	$18^{+8.2}_{-8.1}$	$18^{+8.2}_{-8.1}$	$18^{+8.2}_{-8.1}$	$18^{+8.2}_{-8.1}$	$18^{+8.2}_{-8.1}$
Frio	b	$\mathbf{3.7^{+3.3}_{-1.1}}$	$5.9^{+5.3}_{-2.2}$	$8^{+4.3}_{-4.3}$	$8.6^{+3.7}_{-4.9}$	$8.6^{+3.7}_{-4.9}$	$8.6^{+3.7}_{-4.9}$	$8.6^{+3.7}_{-4.9}$	$8.6^{+3.7}_{-4.9}$	$8.6^{+3.7}_{-4.9}$	$8.6^{+3.7}_{-4.9}$	$8.6^{+3.7}_{-4.9}$
Frio	c	$\mathbf{3.6^{+3.2}_{-1}}$	$5.5^{+5}_{-1.6}$	$7.3^{+6.6}_{-2}$	$8.9^{+8}_{-2.5}$	$12^{+5.7}_{-5}$	$12^{+5.4}_{-5.4}$	$12^{+5.4}_{-5.4}$	$12^{+5.4}_{-5.4}$	$12^{+5.4}_{-5.4}$	$12^{+5.4}_{-5.4}$	$12^{+5.4}_{-5.4}$
Madison	a	$5.3^{+2.2}_{-2}$	$5.3^{+2.2}_{-2}$	$5.3^{+2.2}_{-2}$	$5.3^{+2.2}_{-2}$	$5.3^{+2.2}_{-2}$	$5.3^{+2.2}_{-2}$	$5.3^{+2.2}_{-2}$	$5.3^{+2.2}_{-2}$	$5.3^{+2.2}_{-2}$	$5.3^{+2.2}_{-2}$	$5.3^{+2.2}_{-2}$
Madison	b	$6.6^{+2.6}_{-2.8}$	$6.6^{+2.6}_{-2.8}$	$6.6^{+2.6}_{-2.8}$	$6.6^{+2.6}_{-2.8}$	$6.6^{+2.6}_{-2.8}$	$6.6^{+2.6}_{-2.8}$	$6.6^{+2.6}_{-2.8}$	$6.6^{+2.6}_{-2.8}$	$6.6^{+2.6}_{-2.8}$	$6.6^{+2.6}_{-2.8}$	$6.6^{+2.6}_{-2.8}$
Navajo-Nugget	a	$5.1^{+2.4}_{-2.4}$	$5.1^{+2.4}_{-2.4}$	$5.1^{+2.4}_{-2.4}$	$5.1^{+2.4}_{-2.4}$	$5.1^{+2.4}_{-2.4}$	$5.1^{+2.4}_{-2.4}$	$5.1^{+2.4}_{-2.4}$	$5.1^{+2.4}_{-2.4}$	$5.1^{+2.4}_{-2.4}$	$5.1^{+2.4}_{-2.4}$	$5.1^{+2.4}_{-2.4}$
Navajo-Nugget	b	$4.0^{+1.4}_{-1.4}$	$4.0^{+1.4}_{-1.4}$	$4.0^{+1.4}_{-1.4}$	$4.0^{+1.4}_{-1.4}$	$4.0^{+1.4}_{-1.4}$	$4.0^{+1.4}_{-1.4}$	$4.0^{+1.4}_{-1.4}$	$4.0^{+1.4}_{-1.4}$	$4.0^{+1.4}_{-1.4}$	$4.0^{+1.4}_{-1.4}$	$4.0^{+1.4}_{-1.4}$
Morrison		$\mathbf{7.0^{+6.5}_{-1.9}}$	$\mathbf{12^{+11}_{-3.3}}$	$\mathbf{16^{+6.8}_{-4.4}}$	$17^{+5.3}_{-5.3}$	$17^{+5.3}_{-5.3}$	$17^{+5.3}_{-5.3}$	$17^{+5.3}_{-5.3}$	$17^{+5.3}_{-5.3}$	$17^{+5.3}_{-5.3}$	$17^{+5.3}_{-5.3}$	$17^{+5.3}_{-5.3}$
Potomac		$3.6^{+1.5}_{-1.5}$	$3.6^{+1.5}_{-1.5}$	$3.6^{+1.5}_{-1.5}$	$3.6^{+1.5}_{-1.5}$	$3.6^{+1.5}_{-1.5}$	$3.6^{+1.5}_{-1.5}$	$3.6^{+1.5}_{-1.5}$	$3.6^{+1.5}_{-1.5}$	$3.6^{+1.5}_{-1.5}$	$3.6^{+1.5}_{-1.5}$	$3.6^{+1.5}_{-1.5}$
Fox Hills		$\mathbf{3.0^{+3.1}_{-0.98}}$	$\mathbf{4.7^{+3.1}_{-1.5}}$	$5.5^{+2.3}_{-2.3}$	$5.5^{+2.3}_{-2.3}$	$5.5^{+2.3}_{-2.3}$	$5.5^{+2.3}_{-2.3}$	$5.5^{+2.3}_{-2.3}$	$5.5^{+2.3}_{-2.3}$	$5.5^{+2.3}_{-2.3}$	$5.5^{+2.3}_{-2.3}$	$5.5^{+2.3}_{-2.3}$
Paluxy		$1.5^{+0.5}_{-0.5}$	$1.5^{+0.5}_{-0.5}$	$1.5^{+0.5}_{-0.5}$	$1.5^{+0.5}_{-0.5}$	$1.5^{+0.5}_{-0.5}$	$1.5^{+0.5}_{-0.5}$	$1.5^{+0.5}_{-0.5}$	$1.5^{+0.5}_{-0.5}$	$1.5^{+0.5}_{-0.5}$	$1.5^{+0.5}_{-0.5}$	$1.5^{+0.5}_{-0.5}$
St. Peter		$\mathbf{1.4^{+0.55}_{-0.41}}$	$1.6^{+0.38}_{-0.38}$	$1.6^{+0.38}_{-0.38}$	$1.6^{+0.38}_{-0.38}$	$1.6^{+0.38}_{-0.38}$	$1.6^{+0.38}_{-0.38}$	$1.6^{+0.38}_{-0.38}$	$1.6^{+0.38}_{-0.38}$	$1.6^{+0.38}_{-0.38}$	$1.6^{+0.38}_{-0.38}$	$1.6^{+0.38}_{-0.38}$
Cedar Keys		$\mathbf{2.1^{+2}_{-0.58}}$	$\mathbf{3.4^{+3.3}_{-0.97}}$	$\mathbf{4.7^{+4.5}_{-1.3}}$	$\mathbf{5.8^{+5.6}_{-1.6}}$	$\mathbf{8^{+7.7}_{-2.3}}$	$\mathbf{9.9^{+9.5}_{-2.8}}$	$\mathbf{12^{+11}_{-3.3}}$	$\mathbf{14^{+13}_{-3.9}}$	$\mathbf{17^{+17}_{-4.9}}$	$\mathbf{21^{+20}_{-5.8}}$	$\mathbf{24^{+23}_{-6.8}}$

Chapter 3

The evolution of miscible gravity currents in horizontal porous layers

3.1 Summary

Gravity currents of miscible fluids in porous media are important to understand because they occur in important engineering projects, such as enhanced oil recovery and geologic CO_2 sequestration. These flows are often modeled based on two simplifying assumptions: vertical velocities are negligible compared to horizontal velocities, and diffusion is negligible compared to advection. In many cases, however, these assumptions limit the validity of the models to a finite, intermediate time interval during the flow, making prediction of the flow at early and late times difficult. Here, we consider the effects of vertical flow and diffusion to develop a set of models for the entire evolution of a miscible gravity current. To gain physical insight, we study a simple system: lock exchange of equal-viscosity fluids in a horizontal, vertically-confined layer of permeable rock. We show that the flow exhibits five regimes: 1. an early-diffusion regime, in which the fluids diffuse across the initially sharp fluid-fluid interface; 2. an S-slumping regime, in which the fluid-fluid interface tilts in an S-shape; 3. a straight-line slumping regime, in which the fluid-fluid interface tilts as a straight line; 4. a Taylor-slumping regime, in which Taylor dispersion at the aquifer scale enhances mixing between the fluids and causes the flow to continuously decelerate; and 5.

a late-diffusion regime, in which the flow becomes so slow that mass transfer again occurs dominantly though diffusion.

3.2 Introduction

Gravity currents involving miscible fluids in porous layers occur in important engineering systems. For example, during the drilling of an oil well, miscible drilling fluids penetrate into the reservoir as a gravity current [43]. Later in the life of some reservoirs, oil production is enhanced by injecting a miscible fluid such as CO_2 or a mixture of refined hydrocarbons, which migrates though the reservoir as a gravity current [93]. Along the coastline, seawater can infiltrate freshwater aquifers as a gravity current [65]. In deep saline aquifers, miscible gravity currents can occur during CO_2 sequestration when the CO_2 dissolves into the groundwater. Since groundwater with dissolved CO_2 is more dense than the ambient groundwater, it will migrate away from the free-phase CO_2 as a gravity current.

Many models of gravity currents in porous media have been derived under several simplifying assumptions. One common assumption is that vertical flow velocities are negligible compared to horizontal velocities [17, 168]. This assumption is often called the Dupuit approximation or vertical-flow equilibrium. While diffusion and dispersion in porous-media flows have been extensively studied, gravity-current models commonly assume that these effects are negligible compared to advection [17]. This assumption is often called the sharp-interface approximation since neglecting diffusion and dispersion causes the fluids to always be separated by a sharp boundary. Under these assumptions, several models of gravity currents have been developed for 2D rectilinear systems [17, 34, 77, 66, 35, 107], 2D axisymmetric systems [12, 43, 104, 128], and 3D systems [159, 35].

Recent work on seawater intrusion into coastal freshwater aquifers has included the effects of both vertical flow and diffusion or dispersion. Tartakovsky et al. [151] incorporate linear dispersion through a perturbation analysis, Dentz et al. [36] incorporate diffusion through a perturbation analysis, and Paster and Dagan [134] incorporate velocity-dependent transverse dispersion though a boundary-layer analysis. In these studies, the geologic setting makes the flow field steady state: the pressure-driven flow of freshwater toward the sea resists the gravity-driven flow of seawater into the aquifer, ultimately freezing the position of the seawater current. As a result, the incorporation of vertical flow and diffusion/dispersion

106

a. Initial condition $(t = 0)$ **b.** Exchange flow $(t > 0)$
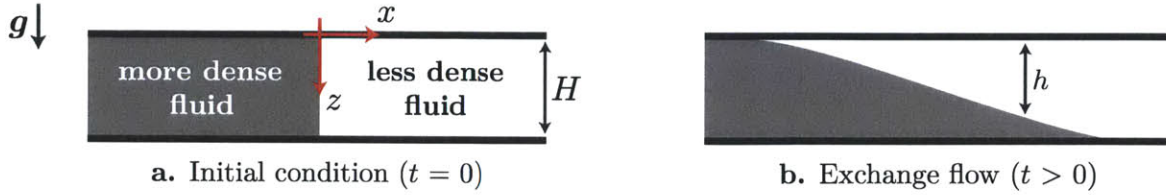
Figure 3-1: We study the lock exchange of two miscible, equal-viscosity fluids in a horizontal porous layer. **a.** The lock gate is initially located at $x = 0$. The fluid on the left of the gate is more dense than the fluid on the right. **b.** After the lock gate is removed, the fluids undergo an exchange flow.

does not affect the dynamics of the gravity-current propagation.

Here, we consider the effects of vertical flow and diffusion on gravity currents that do not exhibit a steady state. We study a simple system to gain physical insight: the lock exchange of equal-viscosity fluids in a horizontal, vertically-confined layer of permeable rock (Figure 4-1). The layer is infinite in the horizontal direction; the top and bottom of the layer are impermeable boundaries. Initially, the more dense fluid occupies the left half of the layer, and is separated by the lock gate from the less dense fluid on the right. When the gate is removed, the fluids undergo an exchange flow, with the more dense fluid flowing to the right along the bottom of the layer and the less dense fluid flowing to the left along the top.

Currently, the model for this system, which we call the straight-line slumping model, is based on both the Dupuit and sharp-interface approximations [17, 77, 34]. While this model provides physical insight and can accurately describe the flow when the approximations hold, it is valid for only a finite, intermediate time interval during the flow. It is not valid at early times after the lock gate is removed because vertical velocities are important in the early slumping. At late times, it is also not valid because diffusion and dispersion will eventually smear the sharp interface between the fluids into a large transition zone.

We find that the lock exchange of miscible fluids exhibits four self-similar regimes in addition to straight-line slumping (Figure 4-2). For each regime, we simplify the governing equations to develop an analytical model of the flow. We find that neglecting vertical flow and diffusion is only valid at intermediate times during the straight-line slumping regime. For all other times, at least one of these effects must be included to capture the physics.

We validate the models of two of the regimes, S-slumping and straight-line slumping, with experiments. The experiments are performed in acrylic Hele-Shaw cells with a 3 mm gap that is packed with glass beads. The fluids are water and dyed salt water. To prepare
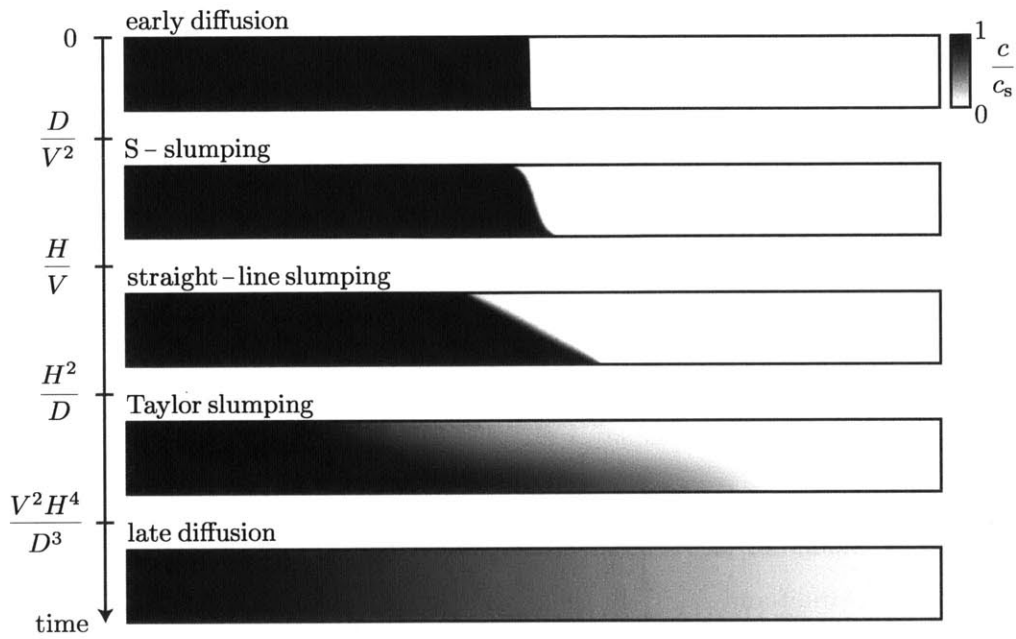
Figure 3-2: The flow evolves through the five self-similar regimes shown here by simulation results. The gray scale represents the concentration of the more dense fluid, c, normalized to the saturated concentration, c_s. The scalings of the transition times between the regimes are shown in terms of the layer thickness, H, the diffusion coefficient, D, and the characteristic velocity, $V = \Delta \rho g k / \mu \phi$. When $HV/D \lesssim 1$, the first and final transition times become equal, the duration of the intermediate regimes becomes zero, and lateral diffusion becomes the dominant mass transfer mechanism for all times.

an experiment, we first turn the cell upright so that the long dimension is vertical, fill it halfway with salt water, and then the rest of the way with fresh water so that the fresh water–salt water interface is horizontal. To begin the experiment, we turn the cell 90 degrees and image the fluid interface with a DSLR camera.

We validate all of the models with numerical simulations of the full governing equations. When comparing the models with simulation results, we consider the vertically averaged concentration of the aquifer, $\bar{c}$. When the interface between the two fluids is sharp, this is directly proportional to the height of the more dense fluid: $\bar{c} \sim H - h$ (Figure 4-1). We also consider the mass flux across the original location of the lock gate, which is a convenient parameter to characterize the system throughout its entire evolution, regardless of whether the fluid-fluid interface remains sharp or a large transition zone develops due to mixing.

3.3 Governing equations

The density-driven flow of two miscible fluids in a horizontal porous medium is described by a coupled system of equations. When the density difference between the fluids is small relative to the density of the fluids, the Boussineq approximation is valid and the equations are [96]:

$$\nabla \cdot \boldsymbol{u} = 0, \tag{3.1}$$

$$\boldsymbol{u} = -\frac{k}{\mu\phi}\left(\nabla p - \rho(c)g\hat{\boldsymbol{z}}\right), \tag{3.2}$$

$$\frac{\partial c}{\partial t} + \boldsymbol{u} \cdot \nabla c - D\nabla^2 c = 0. \tag{3.3}$$

Equation 4.1 expresses conservation of mass for the entire fluid mixture, Equation 4.2 is Darcy's law, and Equation 4.3 is the concentration equation. The concentration, c, may be interpreted in two ways: if the two fluids are both solvents and the more dense fluid contains the dissolved component, such as the case for a water/salt water system, then c is the concentration of the dissolved component; if the two fluids are pure fluids such as water and ethanol, c is the concentration of the denser fluid. For convenience, we assume the former case in the remainder of the text. The density, ρ, is assumed to be a linear function of the concentration: $\rho = \rho_0 + \Delta\rho\frac{c}{c_s}$, where $\Delta\rho$ is the maximum density difference between the fluids and c_s is the saturated concentration ($c_s = 1$ for a system of two pure fluids). The remaining variables are as follows: $\boldsymbol{u} = (u, v)$ is the pore velocity, k is the permeability, μ is

109

the dynamic viscosity, ϕ is the porosity, p is the pressure, g is the gravitational acceleration, and D is the diffusion coefficient. For simplicity, we assume that hydrodynamic dispersion is negligible; we address the implications on this assumption in the conclusions. The initial conditions are that the velocity is zero everywhere, and that the more dense fluid is confined to the left half of the domain:

$$\boldsymbol{u}(x, z, t = 0) = \boldsymbol{0}, \qquad c(x, z, t = 0) = \begin{cases} c_\mathrm{s} & x \leq 0, \\ 0 & x > 0. \end{cases} \tag{3.4}$$

The boundary conditions and conditions at infinity are:

$$v(z = 0, H) = u(x \to \pm\infty) = \frac{\partial c}{\partial z}\bigg|_{z=0,H} = \frac{\partial c}{\partial x}\bigg|_{x\to\pm\infty} = 0. \tag{3.5}$$

When the governing equations (eqs. 4.1–4.3) are made dimensionless, there is only one governing parameter: the Rayleigh number, $Ra = \Delta\rho g k H/\mu\phi D$, which compares the strength of advection to diffusion (see Supplementary Material, §3.6).

We solve the governing equations using two methods. In the first method, we simplify the equations using scaling analyses or perturbation theory and solve the resulting equations analytically. In the second method, we solve the full, 2D system of equations numerically. We integrate in space using finite volumes with linear reconstructions and the MC limiter [101]. We integrate in time using Runge-Kutta methods [94]. For short-time simulations, we use an explicit, two-stage method; for longer simulations, we switch to an implicit-explicit two-stage method to remove the time-step restriction from the diffusion term [6]. The numerical scheme is second-order accurate in both space and time. We have confirmed that the numerical results are converged, grid-independent results.

3.4 Flow regimes

3.4.1 Early diffusion (ed)

Immediately after the lock gate is removed, lateral diffusion across the vertical fluid-fluid interface dominates the mass flux. Diffusion dominates initially because, by Fick's law, the diffusive flux is proportional to the concentration gradient, and therefore goes to infinity in the limit of an initially sharp interface. Since the dynamics involve only diffusion and the

110
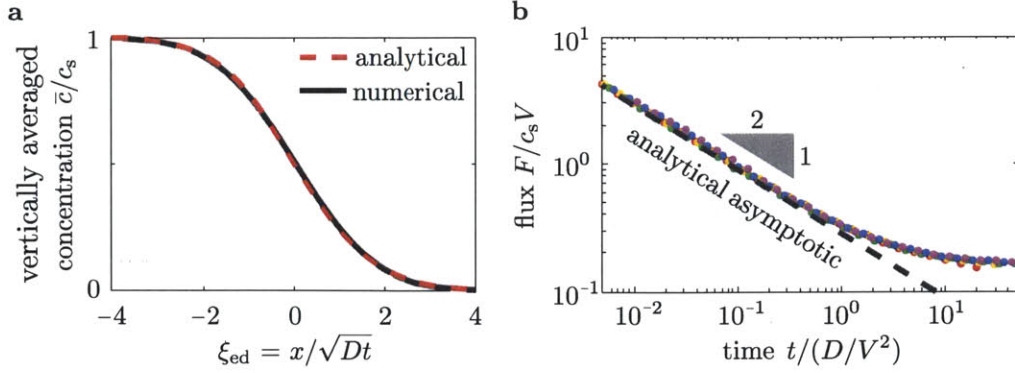
Figure 3-3: **a.** The analytical solution for the vertically averaged concentration (Eq. 3.1) during the first regime, early diffusion, agrees well with the numerical profile (numerical data from $Ra = 500$). **b.** The analytical flux, F, across the original position of the lock gate (dashed, Eq. 3.2) also agrees well with numerical results (circles; $Ra = 100, 200, 500, 700, 1200$), but specifically in the limit that time, t, approaches zero because the regime is an asymptotic. The simultaneous departure of all numerical data from the analytical solution shows that the transition time to the next regime scales as $t_{ss} \sim D/V^2$.

geometry is simple, this regime may be modeled by a similarity solution to a 1D diffusion equation [31]:

$$\frac{c}{c_s} = \frac{1}{2}\left(1 - \mathrm{erf}\left(\frac{x}{2\sqrt{Dt}}\right)\right), \tag{3.6}$$

where the similarity variable is $\xi_{ed} = x/\sqrt{Dt}$. This equation agrees with numerical results for the vertically averaged concentration (Figure 3-3**a**). The mass flux across the initial position of the gate is:

$$F_{ed} = \frac{c_s}{2}\left(\frac{D}{\pi t}\right)^{1/2}, \tag{3.7}$$

which also agrees well with numerical results (Figure 3-3**b**). Both of these expressions are valid in the limit $Ra \to 0$ or, for finite Rayleigh numbers, in the limit $t \to 0$, as shown graphically in Figure 3-3**b** and analytically in the Supplementary Material (§3.6.1). Equating the flux with the flux in the next regime, S-slumping, shows that the transition time to the next regime is $t_{ss} = 2.3D/V^2$, where $V = \Delta\rho g k/\mu\phi$.

3.4.2 S-slumping (ss)

In the second regime, the fluid-fluid interface tilts in an S-shaped curve. While the interface is diffuse for all finite Ra, we model the flow in the limit $Ra \to \infty$ for which the interface is sharp. In this limit, the problem is simplified because diffusion is negligible and the flow self similar in the variable $\xi_{ss} = x/Vt$, as shown by numerical results in Figure 3-4**a**.

111

While there is no exact, analytical model for the flow in this regime, the expression for the similarity variable provides physical insight into the flow. Rearranging the expression for ξ_{ss} to solve for x and differentiating with respect to time yields an expression for the lateral velocity of the interface: $u = \xi_{ss}V$, where ξ_{ss} may now be interpreted as a function of the scaled interface height, h/H. For example, at the leading edge of the current where $h/H = 1$, Figure 3-4a shows that $\xi_{ss} \approx 1.5$, so the velocity of the leading edge is $u \approx 1.5V$. This expression indicates that the interface advances at a constant rate in time. It also indicates that the aquifer height, H, does not affect the dynamics: in other words, the velocity field in two aquifers of different heights is exactly the same when the vertical dimension is scaled by H.

To develop an approximate model of the flow, we integrate the velocity along the interface at $t = 0$, found analytically by De Josselin De Jong [34]. The solution for the height of the interface of the less dense fluid, h, is (see fig. 4-1):

$$\frac{h}{H} = \frac{2}{\pi}\text{arccot}\left(e^{-\pi x/Vt}\right).$$
(3.8)

This solution agrees well with both numerical and experimental results (Figure 3-4b,c). From this equation, we find the mass flux as the time rate of change of the dissolved species mass on the right side of the lock gate:

$$F_{ss} = \frac{1}{H}\frac{d}{dt}\left(c_s \int_0^\infty (H - h)dx\right) = 0.186c_s V.$$
(3.9)

We use the similarity variable to simplify the integral and then evaluate it numerically. Since equations 3.8 and 4.23 were derived in the limit $Ra \to \infty$, they are asymptotics, accurately describing the flow at large Rayleigh numbers but becoming increasingly inaccurate for small Ra (Figure 4d). In the limit $Ra \to \infty$, they are rigorously valid for an infinitesimally small time after $t = 0$ since they are derived using only the velocity field at $t = 0$, but they provide reasonable descriptions of the flow for longer times (Figures 4c,d). For finite Ra, they become valid at the onset of the S-slumping regime at time $t_{ss} = 2.3D/V^2$.

3.4.3 Straight-line slumping (sls)

In the third regime, the fluid-fluid interface tilts as a straight line. As in the previous regime, the interface is diffuse, but we model the flow in the sharp-interface limit. Since the
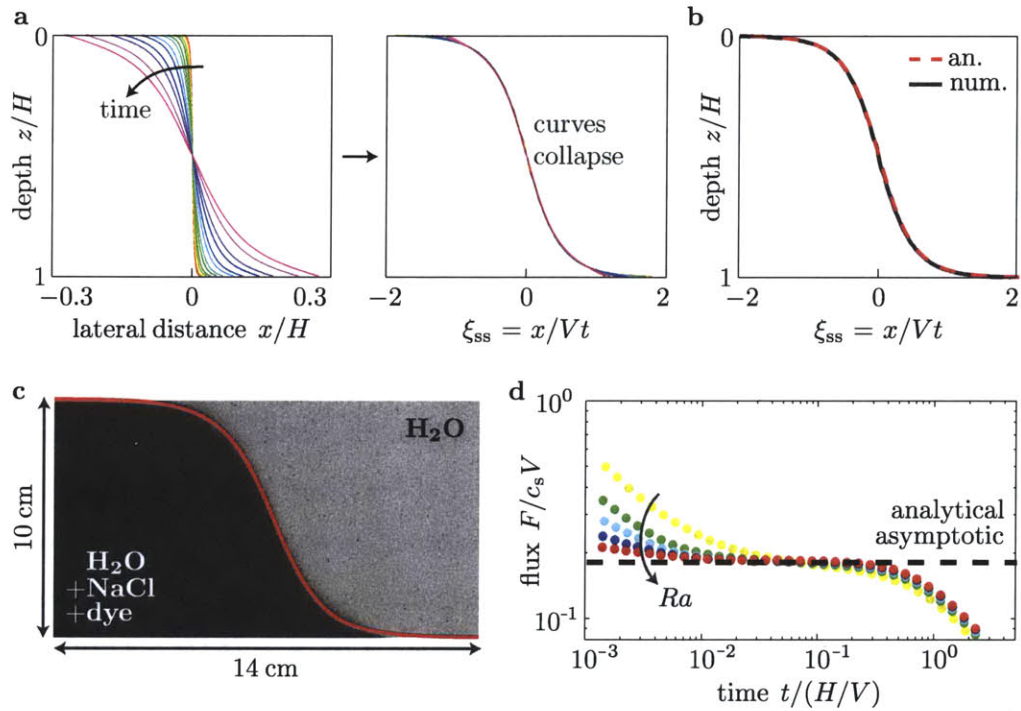
Figure 3-4: **a.** The second regime, S-slumping, is self-similar in $\xi_{ss} = x/Vt$: when numerical solutions for the fluid-fluid interface at several times are plotted versus ξ_{ss}, they all collapse onto a single curve. **b.** The approximate analytical solution for the height of the sharp interface (red dashed; Eq. 3.3) agrees well with numerical results for the problem with no diffusion (black; $Ra = \infty$). **c.** The approximate solution (red) also agrees well with experiments of salt water slumping in a Hele-Shaw cell packed with glass beads ($\Delta\rho = 50\,\mathrm{kg/m^3}$; bead diameter 0.5mm; $t = 3$ min). **d.** The analytical solution is an asymptotic in the limit $Ra \to \infty$: as Ra becomes larger, the mass flux calculated from numerics (circles; $Ra = 300, 1000, 2150, 4650, 10000$) converges to the value from the analytical solution (dashed). The transition time to the next regime scales as $t_{sls} \sim H/V$, as shown by the simultaneous departure of all numerical data from the dashed line.

lateral extent of the flow in this regime is typically large compared to the aquifer thickness, we assume that vertical velocities are negligible compared to horizontal velocities (Dupuit approximation is valid). Under these approximations, Huppert and Woods [77] showed that the flow is self-similar in the variable $\xi_{\text{sls}} = x/\sqrt{VHt}$, and derived the following analytical solution for the interface height, h:

$$\frac{h}{H} = \frac{1}{2}\left(1 + \frac{x}{\sqrt{VHt}}\right).$$

(3.10)

This solution agrees well with both numerical and experimental results (Figure 3-5a,b). Perturbation analysis shows that this solution is accurate to first order in $\varepsilon = H/L$, where L is the horizontal extent of the interface [168].

As in the previous regime, the expression for the similarity variable, $\xi_{\text{sls}} = x/\sqrt{VHt}$, provides physical insight into the flow. Interpreting VH as analogous to a diffusion coefficient, we find that ξ_{sls} exhibits the same form as the similarity variable for Fickian diffusion alone, $\xi_{\text{ed}} = x/\sqrt{Dt}$. This comparison indicates that the fluid interface in this regime spreads diffusively. Specifically, the lateral velocity of the interface, u, decreases in time as $u \sim t^{-1/2}$, just as the velocity of a concentration contour decreases as $t^{-1/2}$ as it propagates away from the initially vertical interface in the early diffusion regime. The exact expression for the flow velocity can be determined from Equation 3.10: $u = (h/H - 1/2)(VH/t)^{1/2}$. This diffusive spreading is different from the S-slumping regime, in which the lateral velocities are constant in time. It is also different because the aquifer thickness, H, now affects the dynamics through the effective diffusion coefficient $D_{\text{sls}} = VH$. Since the spreading is diffusive, the mass flux across the initial lock position is also diffusive:

$$F_{\text{sls}} = \frac{1}{H}\frac{d}{dt}\left(c_{\text{s}}\int_0^{x_n}(H - h)dx\right) = \frac{c_{\text{s}}}{8}\left(\frac{VH}{t}\right)^{1/2},$$

(3.11)

where $x_n = \sqrt{VHt}$ is the location of the rightmost edge of the dense current.

Since the equations for the flux (Eq. 3.11), velocity, and interface height (Eq. 3.10) are based on the sharp-interface approximation, they represent asymptotics of the full problem with diffusion, providing an increasingly accurate description of the flow as $Ra \to \infty$ (Figure 3-5). They become invalid at time $t_{\text{Ts}} \sim H^2/D$, when the regime ends because vertical diffusion creates a broad transition zone between the two fluids.

114
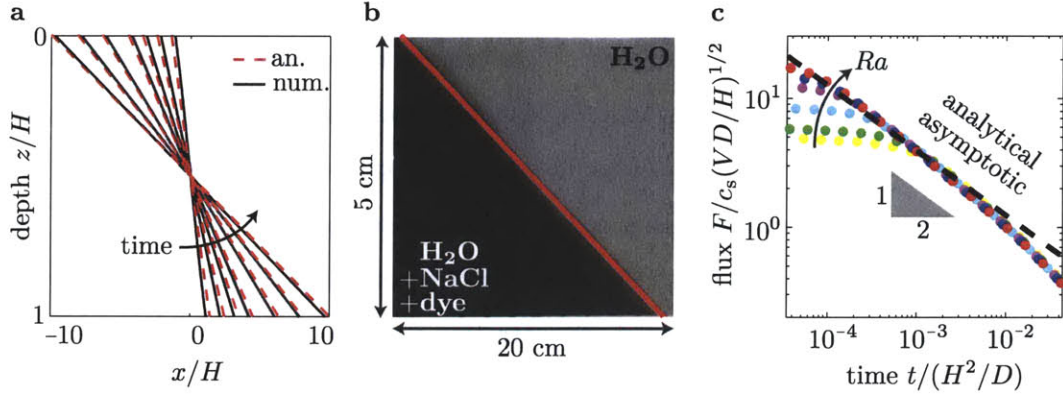
Figure 3-5: **a.** The analytical model in the third regime, straight-line slumping, for the height of the sharp interface (red dashed; Eq. 3.10) matches the numerical solution for the problem with no diffusion (black; $Ra = \infty$; $t/(H/V) = 2, 6, 12, 20, 40, 65, 99$). Since the model is an intermediate asymptotic [13], the disagreement is largest at early times and decreases as $t \to \infty$. **b.** The analytical model (red) also agrees well with experiments of salt water slumping in a Hele-Shaw cell packed with glass beads ($\Delta\rho = 100\,\mathrm{kg/m^3}$; bead diameter 0.5 mm; $t = 10$ min.). **c.** Since the model is based on the sharp-interface approximation, the mass flux, F, calculated from numerics (circles; $Ra = 300, 700, 1000, 2150, 4650, 10000$) approaches the flux from the model (dashed; Eq. 3.5) as $Ra \to \infty$. The departure of all numerical data from the dashed line shows that the transition time to the next regime scales as $t_{\mathrm{Ts}} \sim H^2/D$.

3.4.4 Taylor slumping (Ts)

In the fourth regime, the dynamics are controlled by the coupling between diffusion and gravity-driven advection. Advection impacts diffusion because it increases the interfacial area between the two fluids, which accelerates the diffusive mixing. This process is Taylor dispersion at the aquifer scale, for which the regime is named [152]. Diffusive mixing impacts advection because it reduces the lateral density gradient that drives advection. The relationship between the gradient of vertically averaged density, $\bar{\rho}$, and the lateral velocity, u, is:

$$u(z) = \frac{gkH}{\phi\mu}\frac{\partial\bar{\rho}}{\partial x}\left(\frac{1}{2} - \frac{z}{H}\right) + O(\varepsilon^2),\tag{3.12}$$

where $\varepsilon = H/L$ and L is the horizontal extent of the flow (Eq. 3.25). This equation shows that at long times when $\varepsilon \ll 1$, mixing retards the gravity-driven slumping in direct proportion to the degree to which it reduces $\partial\bar{\rho}/\partial x$.

To model Taylor slumping, we derive an equation for the vertically averaged concentration, $\bar{c}$ (see Supplementary Material, §3.6.2):

$$\frac{\partial\bar{c}}{\partial t} - D\frac{\partial^2\bar{c}}{\partial x^2} - \frac{\partial}{\partial x}\left(\frac{H^4V^2}{120Dc_{\mathrm{s}}^2}\left[\frac{\partial\bar{c}}{\partial x}\right]^2\frac{\partial\bar{c}}{\partial x}\right) = 0.\tag{3.13}$$

The middle term in this equation captures Fickian diffusion in the lateral direction. The rightmost term captures Taylor slumping. This type of term involving the concentration gradient cubed occurs in a variety of models describing the coupling between buoyancy and shear dispersion, including models of pipe flow [49] and open-channel flow [145].

To emphasize the physical meaning of the Taylor slumping term, we compare it to the classical Taylor dispersion term for Poiseuille flow between parallel plates. In this system, the equation for the vertically averaged concentration is:

$$\frac{\partial \overline{c}}{\partial t} + \overline{u}\frac{\partial \overline{c}}{\partial x} - D\frac{\partial^2 \overline{c}}{\partial x^2} - \frac{\partial}{\partial x}\left(\frac{b^2\overline{u}^2}{210D}\frac{\partial \overline{c}}{\partial x}\right) = 0. \tag{3.14}$$

where $\overline{u}$ is the average velocity and b is the distance between the plates [125]. The rightmost term in this equation captures classical Taylor dispersion. It is a linear diffusion term with an effective diffusion coefficient $D_{\mathrm{Td}} = b^2\overline{u}^2/210D$. The Taylor slumping term in Equation 3.13 can also be interpreted as a diffusion term, but it is nonlinear with an effective diffusion coefficient $D_{\mathrm{Ts}} = (H^4V^2/120Dc_{\mathrm{s}}^2)(\partial \overline{c}/\partial x)^2$. The nonlinearity arises due to the coupling between diffusive mixing and the gravity-driven flow: diffusive mixing reduces the flow velocity (Eq. 4.31), which in turn reduces the diffusive mixing by lowering the rate at which the interfacial area between the two fluids grows. This coupling does not occur in classical Taylor dispersion because the velocity is constant during Poiseuille flow.

In Equation 3.13, the Taylor slumping term dominates the Fickian diffusion term at early times when the aspect ratio of the flow is small relative to the Rayleigh number: $L/H \ll Ra/\sqrt{120}$. This result comes from scaling x by the lateral extent of the flow, L, and taking the ratio of the coefficients of the Taylor slumping term and Fickian diffusion term. When the Taylor slumping term dominates, the Fickian diffusion term may be neglected and the equation admits an exact, analytical similarity solution in the variable $\xi_{\mathrm{Ts}} = x/(H^4V^2t/120D)^{1/4}$:

$$\frac{\overline{c}}{c_{\mathrm{s}}} = \frac{1}{2} - \frac{1}{2\sqrt{12}}\left[\xi_{\mathrm{Ts}}\left(\alpha^2 - \xi_{\mathrm{Ts}}^2\right)^{1/2} + \alpha^2 \arcsin\left(\frac{\xi_{\mathrm{Ts}}}{\alpha}\right)\right], \tag{3.15}$$

where $\alpha = (48/\pi^2)^{1/4}$. This solution agrees well with numerical results (Figure 3-6a).

In Taylor slumping, the lateral velocities decrease *sub-diffusively* in time, scaling as $u \sim t^{-3/4}$. Based on the similarity variable, the expression for the lateral velocity is $u = \xi_{\mathrm{Ts}}(H^4V^2/480Dt^3)^{1/4}$, where ξ_{Ts} can now be interpreted as a function of the average

116
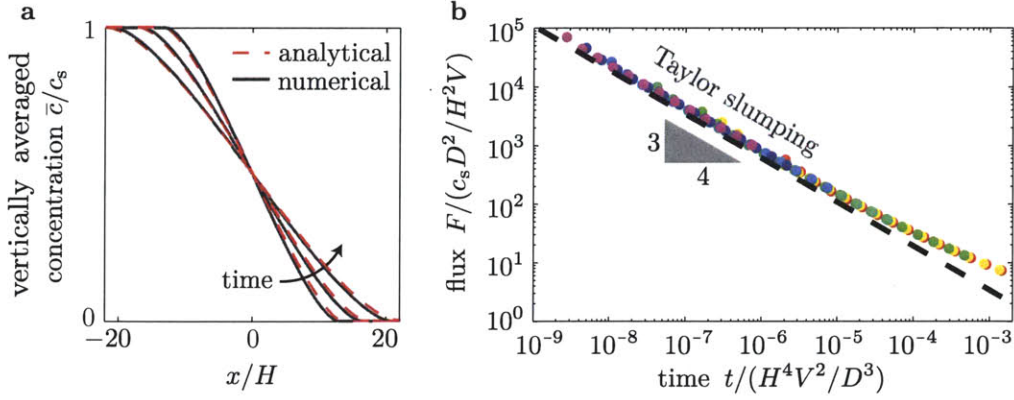
Figure 3-6: **a.** The analytical model for the vertically averaged concentration during the Taylor slumping regime (Eq. 4.25) agrees well with the numerical profile ($Ra = 1000$; $t/(H/V) = 670, 1700, 4500$). **b.** The mass flux obtained from this model (dashed, Eq. 4.29) also agrees well with numerical results (circles; $Ra = 300, 700, 1000, 2150, 4650, 10000$). Here we only show data after the onset of Taylor slumping for clarity. The transition time to the next regime is $t_{\text{ld}} \sim H^4 V^2/D^3$, as shown by the simultaneous departure of all data from the dashed line.

concentration. For example, at the leading edge of the current where the average concentration is zero, $\xi_{\text{Ts}} = \alpha$ and $u = \alpha(H^4 V^2/480 D t^3)^{1/4}$. The velocity decreases faster than in the previous regime, in which velocity decreases diffusively in time, due to the reduction in velocity caused by diffusive mixing (Eq. 4.31).

Since the velocities are sub-diffusive, the mass flux during Taylor slumping is also sub-diffusive:

$$F_{\text{Ts}} = \frac{1}{H} \frac{d}{dt} \left(H \int_0^\infty \bar{c} \, dx \right) = \frac{c_{\text{s}}}{(3240 \pi^6)^{1/4}} \left(\frac{H^4 V^2}{D t^3} \right)^{1/4}. \tag{3.16}$$

This expression agrees well with numerical results (Figure 3-6**b**), helping validate the Taylor slumping model.

3.4.5 Late diffusion (ld)

At times much later than $t_{\text{ld}} = 2H^4 V^2/405 \pi^4 D^3$, the Taylor slumping term in Equation 3.13 becomes negligible compared to the Fickian diffusion term. This can can been seen by comparing the fluxes due to Taylor slumping (Eq. 4.29) and Fickian diffusion (Eq. 3.7). At these late times, the vertically averaged density gradient, which drives the flow, becomes very small and causes the horizontal flow to become very slow (Eq. 4.31). When the horizontal flow becomes slow, the vertical mass transfer due to diffusion dominates the lateral mass transfer due to the flow, and the concentration becomes nearly uniform in the

vertical direction. The relationship between the vertical concentration gradient and the horizontal velocity can be found explicitly from a perturbation analysis (Eq. B7): $\frac{\partial c}{\partial z} = \frac{1}{D}\frac{\partial \bar{c}}{\partial x}\int_0^z u\ dz + O(\varepsilon^2)$. As a result of the slow flow and nearly complete vertical mixing, mass transfer occurs dominantly via Fickian diffusion in the lateral direction. This regime is the same as the first regime, early diffusion, and may be modeled by the same equation (Eq. 3.6).

For some conditions, the late diffusion regime occurs immediately after the early diffusion regime, and there is no distinction between them. Subtracting the end time of the early diffusion regime from the onset time of the late diffusion regime yields an expression for the duration of the intermediate regimes: $t_{\text{ld}} - t_{\text{ss}} = 2D/405\pi^4 V^2\left(Ra^4 - 2.3\right)$. When $Ra \lesssim 1$, the duration is zero and the two diffusion regimes occur consecutively.

3.5   Conclusion

The gravity-driven flow of two miscible fluids in a horizontal porous layer evolves through five regimes. When the fluids are initially separated by a sharp interface, the first regime is diffusion. In the next two regimes, the gravity-driven flow dominates. At the beginning of the flow, when the lateral extent of the current is less than the aquifer thickness, the fluid-fluid interface tilts in an S-shaped curve. In this regime, the leading edge of the interface propagates at a constant velocity. When the extent of the current exceeds the aquifer thickness, the fluid interface changes from an S-shaped curve to a straight line. In this regime, the leading edge continually decelerates, exhibiting a diffusive scaling in time. In the following regime, Taylor slumping, the flow becomes coupled to diffusive mixing. The flow affects diffusive mixing via Taylor dispersion at the aquifer scale, in which the non-uniform flow velocities elongate the fluid-fluid interface over which diffusion acts to mix the fluids. Diffusive mixing affects the flow by reducing the lateral density gradient that drives the flow. This coupling causes the flow to decelerate *sub-diffusively*. Eventually, the velocity becomes so low that diffusion causes the fluids to be nearly completely mixed in the vertical direction. In this regime, lateral diffusion through the aquifer again becomes the dominant mass transfer process. All of these regimes can be described by analytical models, which when combined in series, provide a complete picture of the entire evolution of the flow, as shown in Figure 3-7.

The evolution of the flux is indicative, for example, of the rate of dissolution that can be expected from CO_2 injected and stored in geological traps. In geological CO_2 sequestration, relevant values of Ra exhibit a large range due to the large ranges of aquifer thickness and permeability [47, 138]. Assuming $\Delta\rho = 5\text{kg/m}^3$, $k = 10\text{--}1000\text{mD}$, $\mu = 1\text{mPas}$, $\phi = 0.2$, $H = 25\text{--}500\text{m}$, $D = 1 \times 10^{-9}\text{m}^2/\text{s}$, Ra ranges from about 500 to over 1 million [150]: a range for which it is likely that all five regimes will play a role (Figure 3-7).

While the models have been derived under the assumption of negligible hydrodynamic dispersion, four of the five models remain valid even in systems with strong dispersivity. Dispersion will not affect the first and final regimes in which lateral Fickian diffusion dominates, because the flow velocities are negligibly small in these regimes, which in turn makes hydrodynamic dispersion negligibly small. It will also not affect the models of S-slumping or straight-line slumping, since these models are based on the assumption of negligible fluid mixing. These models will still be valid at early times for which advection dominates diffusion and dispersion, though the timespan over which they are valid will likely be reduced since dispersion would cause the fluids to mix more rapidly.

While hydrodynamic dispersion will not affect most of the regimes, it will affect Taylor slumping since this regime describes the interplay between fluid mixing and gravity-driven advection. As a result, the model for Taylor slumping will be accurate in very slow flows for which dispersion is negligible. If dispersion is not negligible, the physical mechanism captured by the Taylor slumping model will likely still be valid: mixing will lead to a reduced lateral density gradient, which will decrease the horizontal velocity until lateral diffusion dominates the mass transfer. Hydrodynamic dispersion, however, will likely accelerate this process by enhancing the mixing.
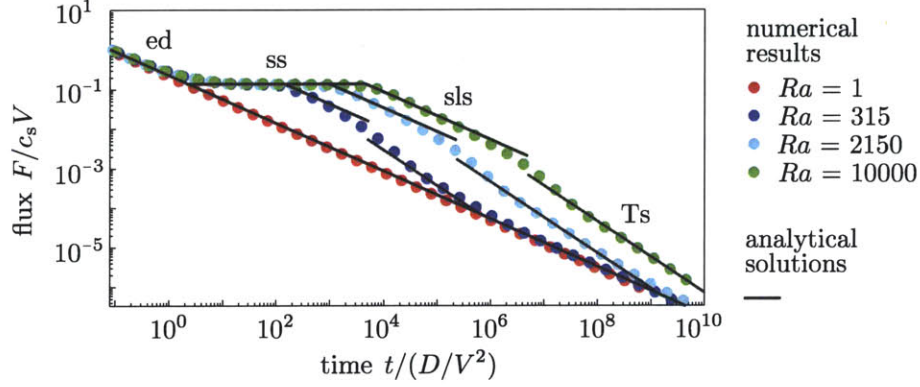
Figure 3-7: The entire evolution of the miscible lock-exchange problem in a horizontal porous layer may be described by combining analytical solutions for five flow regimes.

3.6 Supplementary material

3.6.1 Early diffusion

To derive the model for the early diffusion regime, we scale the variables as follows:

$$z = H\zeta, \ x = L\eta, \ t = (H^2/D)\tau, \ p = \overline{P}p' + \rho_0 g H\zeta, \ c = c_s c', \ v = Vv', \ u = Vu', \quad (3.17)$$

where $\overline{P} = \Delta\rho g H$ is the characteristic pressure and $V = \Delta\rho g k/\mu\phi$ is the characteristic velocity. We define a similarity variable, $\xi_{ed} = \eta/\sqrt{\tau}$. The scaled concentration equation (Eq. 4.3) is then:

$$-\frac{\xi_{ed}}{2}\frac{\partial c'}{\partial \xi_{ed}} + \tau^{1/2}Ra\frac{\partial}{\partial \xi_{ed}}\left(u'c'\right) + \tau Ra\frac{\partial}{\partial \zeta}\left(w'c'\right) - \frac{\partial^2 c'}{\partial \xi_{ed}^2} - \tau\frac{\partial^2 c'}{\partial \zeta^2} = 0. \quad (3.18)$$

In the limit $\tau \to 0$, it reduces to:

$$\frac{\xi_{ed}}{2}\frac{dc'}{d\xi_{ed}} + \frac{d^2 c'}{d\xi_{ed}^2} = 0. \quad (3.19)$$

This equation is also obtained in the limit $Ra \to 0$ since the initial condition and boundary conditions make $\partial^2 c'/\partial\zeta^2 = 0$ for all times. The equation is the self-similar form of a one-dimensional diffusion equation in a laterally infinite domain. The solution is given in Equation 3.6.

120

3.6.2 Taylor slumping

To derive the model for Taylor slumping, we vertically-average the concentration equation (Eq. 4.3):

$$\frac{\partial \overline{c}}{\partial t} + \frac{\partial}{\partial x}\overline{uc} - D\frac{\partial^2 \overline{c}}{\partial x^2} = 0, \tag{3.20}$$

where overbars denote vertical averages (e.g. $\overline{c} = 1/H \int_0^H c\, dz$). We then obtain an expression for the average advective flux, $\overline{uc}$, via a perturbation analysis of both the averaged and unaveraged governing equations. We begin the perturbation analysis by scaling the variables as follows:

$$z = H\zeta, \quad x = L\xi, \quad p = \overline{P}p' + \rho_0 g H\zeta, \quad c = c_{\mathrm{s}}c', \quad v = Vv', \quad u = Uu', \quad t = T\tau, \tag{3.21}$$

where $V = \Delta\rho g k/\mu\phi$, $U = \varepsilon V$, $P = \Delta\rho g H$, and $T = L/U$. $\varepsilon = H/L$, where L is the lateral extent of the flow, which is unknown a priori but assumed to be large relative to the layer thickness, H, so that $\varepsilon \ll 1$. We expand the variables in ε: $c' = c_0' + \varepsilon^2 c_2' + O(\varepsilon^4)$, $u' = u_0' + \varepsilon^2 u_2' + O(\varepsilon^4)$, $v' = v_0' + \varepsilon^2 v_2' + O(\varepsilon^4)$, and $p' = p_0' + \varepsilon^2 p_2' + O(\varepsilon^4)$. The scaled, vertically averaged concentration equation (Eq. 3.20) to $O(\varepsilon^2)$ is:

$$Ra\left[\frac{\partial}{\partial \tau}\left(\overline{c_0'} + \varepsilon^2 \overline{c_2'}\right) + \frac{\partial}{\partial \xi}\left(\overline{u_0'c_0'} + \varepsilon^2\overline{u_0'c_2'} + \varepsilon^2\overline{u_2'c_0'}\right)\right] - \frac{\partial^2}{\partial \xi^2}\left(\overline{c_0'} + \varepsilon^2\overline{c_2'}\right) = 0. \tag{3.22}$$

We obtain c_0', c_2', and u_0' from the unaveraged concentration equation (Eq. 4.3):

$$\begin{aligned} O(\varepsilon^0) &: Ra\frac{\partial\left(v_0'c_0'\right)}{\partial \zeta} - \frac{\partial^2 c_0'}{\partial \zeta^2} = 0, \\ O(\varepsilon^2) &: Ra\left[\frac{\partial c_0'}{\partial \tau} + \frac{\partial\left(u_0'c_0'\right)}{\partial \xi}\right] + Ra\frac{\partial\left(v_0'c_2'\right)}{\partial \zeta} + Ra\frac{\partial\left(v_2'c_0'\right)}{\partial \zeta} - \frac{\partial^2 c_0'}{\partial \xi^2} - \frac{\partial^2 c_2'}{\partial \zeta^2} = 0, \end{aligned} \tag{3.23}$$

and mass conservation equation (Eq. 4.1):

$$\begin{aligned} O(\varepsilon^0) &: \frac{\partial v_0'}{\partial \zeta} = 0, \\ O(\varepsilon^2) &: \frac{\partial u_0'}{\partial \xi} + \frac{\partial v_2'}{\partial \zeta} = 0, \end{aligned} \tag{3.24}$$

To obtain u_0', we first solve Equation 3.24 at $O(\varepsilon^0)$ using the boundary condition $v_0'(\zeta = 0, 1) = 0$ to find $v_0' = 0$. This indicates that the pressure at $O(\varepsilon^0)$ is hydrostatic, and enables

us to find u_0' using Darcy's law:

$$u_0' = \frac{\partial c_0'}{\partial \xi} \left(\frac{1}{2} - \zeta \right).$$

(3.25)

To obtain c_0', we solve Equation 3.23 at $O(\varepsilon^0)$ to find $c_0' = f(\xi, \tau)$; in other words, c_0' is not a function of ζ. This result makes use of the no-flux boundary conditions at $\zeta = 0, 1$. To obtain c_2', we solve Equation 3.23 at $O(\varepsilon^2)$, using Equation 3.24 at $O(\varepsilon^2)$ to simplify the advective part and Equation 3.22 at $O(\varepsilon)$ to remove the time derivative. Requiring $\overline{c_2'} = 0$, we find:

$$c_2' = \frac{Ra}{2} \left(\frac{\partial c_0'}{\partial \xi} \right)^2 \left(-\frac{1}{12} + \frac{\zeta^2}{2} - \frac{\zeta^3}{3} \right).$$

(3.26)

We now evaluate the average advective fluxes in Equation 3.22: $\overline{u_0' c_0'} = \overline{u_0'} c_0' = 0$ and $\overline{u_2' c_0'} = \overline{u_2'} c_0' = 0$ since the average lateral velocity is always zero. This can be seen by averaging the mass conservation equation (Eq. 4.1) and using the boundary conditions $u'(\xi \to \pm\infty) = 0$ to find $\overline{u'} = 0$. The remaining advective flux is:

$$\overline{u_0' c_2'} = -\frac{Ra}{120} \left(\frac{\partial c_0'}{\partial \xi} \right)^3.$$

(3.27)

We now substitute this expression into Equation 3.22 and replace c_0 using $c_0 = \bar{c} + O(\varepsilon^4)$:

$$Ra \left[\frac{\partial \overline{c'}}{\partial \tau} - \varepsilon^2 \frac{Ra}{120} \frac{\partial}{\partial \xi} \left(\left[\frac{\partial \overline{c'}}{\partial \xi} \right]^2 \frac{\partial \overline{c'}}{\partial \xi} \right) \right] - \frac{\partial^2 \bar{c}}{\partial \xi^2} + O(\varepsilon^4) = 0.$$

(3.28)

This is the scaled version of the equation for Taylor slumping (Eq. 3.13).

122

Chapter 4

CO_2 dissolution in structural and stratigraphic traps

4.1 Summary

Storing CO_2 in structural and stratigraphic traps is a viable option to reduce anthropogenic emissions. While dissolution of the CO_2 stored in these traps reduces the long-term leakage risk, the dissolution process remains poorly understood in systems that reflect the appropriate subsurface geometry. Here, we study dissolution in a porous layer that exhibits a feature relevant for CO_2 storage in structural and stratigraphic traps: a finite CO_2 source along the top boundary that extends only part way into the layer. This feature represents the finite extent of the interface between free-phase CO_2 pooled in a trap and the underlying brine. Using theory and simulations, we describe the dissolution mechanisms in this system for a wide range of times and Rayleigh numbers, and classify the behavior into six regimes. For each regime, we quantify the dissolution flux numerically and model it analytically, with the goal of providing simple expressions to estimate the dissolution rate in real systems. We find that, at late times, the dissolution flux decreases relative to early times as the flow of unsaturated water to the CO_2 source becomes constrained by a lateral exchange flow though the reservoir. Application of the models to several representative reservoirs indicates that dissolution is strongly affected by the reservoir properties, but that thick reservoirs with high permeabilities could potentially dissolve hundreds of megatons of CO_2 in tens of years.

4.2 Introduction

Structural and stratigraphic traps are regions in a deep layer of porous rock in which an overlying, low-permeability seal exhibits a concave-down geometry [80]. In structural traps, this geometry is due to either a large-scale fold in the reservoir or the intersection of a fault with a dipping region of the reservoir. In the case of a fold, the seal is typically a layer of fine-grained rock such as shale or mudstone called a caprock; in the case of a fault, the seal is due to both the caprock and impermeable material within the fault. In stratigraphic traps, the concave-down shape is due to changes in rock type. For example, a dipping reservoir may pinch out between two layers of fine-grained rock or terminate in a unconformity against fine-grained rock (figure 4-1).

Structural and stratigraphic traps are attractive sites for CO_2 sequestration [62]. Their low-permeability seal inhibits the upward migration of CO_2, reducing the risk of leakage to a shallower formation or the surface. While a low-permeability seal can be present at many locations in a reservoir, structural and stratigraphic traps are particularly appealing because their concave-down geometry also constrains the lateral spread of CO_2, reducing the risk that it will migrate away from the injection site to potential leakage pathways such as faults or abandoned wells. Another attractive feature is that many traps have proven seals. When the trap is located in an oil and gas field, for example, the seal quality is confirmed by the fact that it has retained buoyant hydrocarbons for millions of years.

While structural and stratigraphic traps reduce the risk of CO_2 leakage, they do not eliminate it. The seal may contain small fractures or faults that allow leakage but that are not identified in the characterization stage of a sequestration project. In the injection stage, the seal may be compromised by accidentally overpressurizing the reservoir, which could hydraulically fracture the seal or cause slip along a pre-existing fault in the seal [61, 139, 28, 109]. After the injection well has been closed, the seal may be damaged by seismic activity in the future.

Dissolution of the CO_2 into the groundwater mitigates the risk of leakage from an imperfect or compromised seal. This is because water with dissolved CO_2 is more dense than the ambient groundwater, and will tend to sink rather than rise though a leakage pathway. Estimating the dissolution rate will help constrain the quantity of CO_2 that will remain in the target reservoir, and the quantity that will escape.
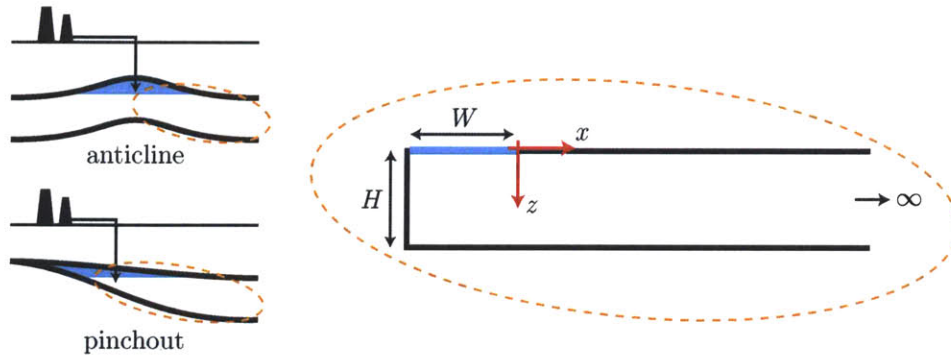
Figure 4-1: We study CO_2 dissolution in a porous layer that exhibits features of structural traps such as anticlines and stratigraphic traps such as pinchouts between low-permeability rock. The layer is semi-infinite to represent the large lateral extent of a deep, geologic reservoir. A portion of the top boundary (blue line) is held at the saturated CO_2 concentration to represent the finite CO_2-groundwater interface.

CO_2 dissolution has been well studied in idealized systems. These systems commonly include laterally infinite porous layers [48, 167, 138, 143], laterally periodic porous layers [136, 135, 69], and laterally closed porous layers in which the side walls are no-flow boundaries [138, 64, 123, 87, 11, 68, 144]. The CO_2-brine interface is typically represented by fixing the top boundary of the system at CO_2 saturation. In these systems, dissolution initially occurs via diffusion only, leading to a diffuse boundary layer of CO_2-rich fluid below the top boundary. Since the boundary layer is more dense than the underlying fluid, it is unstable and breaks up into descending fingers after a time proportional to D/V^2, where D is the diffusion coefficient and V is the characteristic buoyancy velocity, as defined in §4.3 [48, 167, 138, 64, 143]. Due to conservation of mass, fresh water simultaneously rises upward, leading to sharp concentration gradients at the top boundary that increase the dissolution flux. The exact expression of the enhanced dissolution flux remains controversial: experimental studies in analog systems suggest it depends on the Rayleigh number [11, 123], while numerical studies indicate it is independent, at least in the limit of very large Rayleigh numbers [135, 69]. After the fingers reach the bottom of the reservoir, dissolved CO_2 begins to circulate back to the top, lowering the concentration gradients and causing the dissolution rate to continually decrease [144, 68].

Here, we study CO_2 dissolution in a porous layer that more closely reflects storage in a structural or stratigraphic trap. Like most previous studies, we represent the interface between the free-phase CO_2 and groundwater via a boundary condition: we fix the concentration along the top boundary at the saturated CO_2 concentration. Unlike many studies,

however, we apply this condition along only part of the top boundary to represent the finite extent of the interface. To account for the observation that many traps exist in reservoirs that are laterally extensive relative to the thickness of the layer and width of the trap, we set the right boundary at infinity. This combination of a finite CO_2 source in a laterally extensive layer represents either a stratigraphic trap or a structural trap like an anticline that is nearly symmetric about its axial plane (figure 4-1).

While this system represents a geologic trap, it is an idealization. In contrast to an actual trap, the porous layer is homogeneous, isotropic, rectilinear, and perfectly horizontal. There is also no natural background flow and we neglect hydrodynamic dispersion. We invoke these simplifications to focus on the physics of dissolution from a finite CO_2 source, and address some of the limitations they entail in the Discussion section.

In contexts outside of CO_2 sequestration, some studies have investigated natural convection in geometries similar to our idealized CO_2 trap. Elder [45] studied heat transfer in a porous medium in which a portion of the lower boundary was held at an elevated temperature. This system, sometimes called the Elder problem, is similar to ours in that both involve a laterally finite source modeled by a Dirichlet boundary condition; it differs in that the medium is finite and the remaining walls are all held at zero temperature, so a steady-state exists. Wooding et al. [165] and Wooding et al. [166] studied the infiltration of dense, saltwater fingers into a porous layer from an overlying salt lake. This system, often called the salt-lake problem, is also similar to ours in that it involves a finite source; it differs in that the lake exhibits evaporative loss, which both concentrates the salt and drives convection from the surrounding area to the lake, partially stabilizing the saline boundary layer. Cheng and Chang [27] studied boundary layer flow in a porous medium partially overlain by a cold boundary or partially underlain by a hot boundary. This system is similar to ours in the same way as the Elder and salt-lake problems. However, it differs in that the domain is laterally infinite and vertically semi-infinite. Furthermore, due to the boundary-layer approximation, the analysis of Cheng and Chang [27] can not capture fingering or any subsequent behavior. While all of these studies provide insight into natural convection from a finite source, they provide a limited understanding of how CO_2 dissolves in the subsurface.

We find that CO_2 dissolution in our idealized geologic trap occurs through several mechanisms. These mechanisms vary spatially along the length of the CO_2 source: along the

inner regions of the source far from the edge, the dissolution mechanisms are nearly identical to those observed in previous studies of CO_2 dissolution; near the edge, however, the mechanisms are novel and are strongly impacted by flow in the porous layer outside the source region. The dissolution mechanisms also vary temporally, and the different periods of behavior can be organized into seven regimes (figure 4-2). For each regime, we describe the mechanisms and quantify the dissolution flux numerically. We also develop an analytical model of the dissolution flux in each regime, with the goal of providing simple expressions to estimate dissolution rates that can be expected in practice.
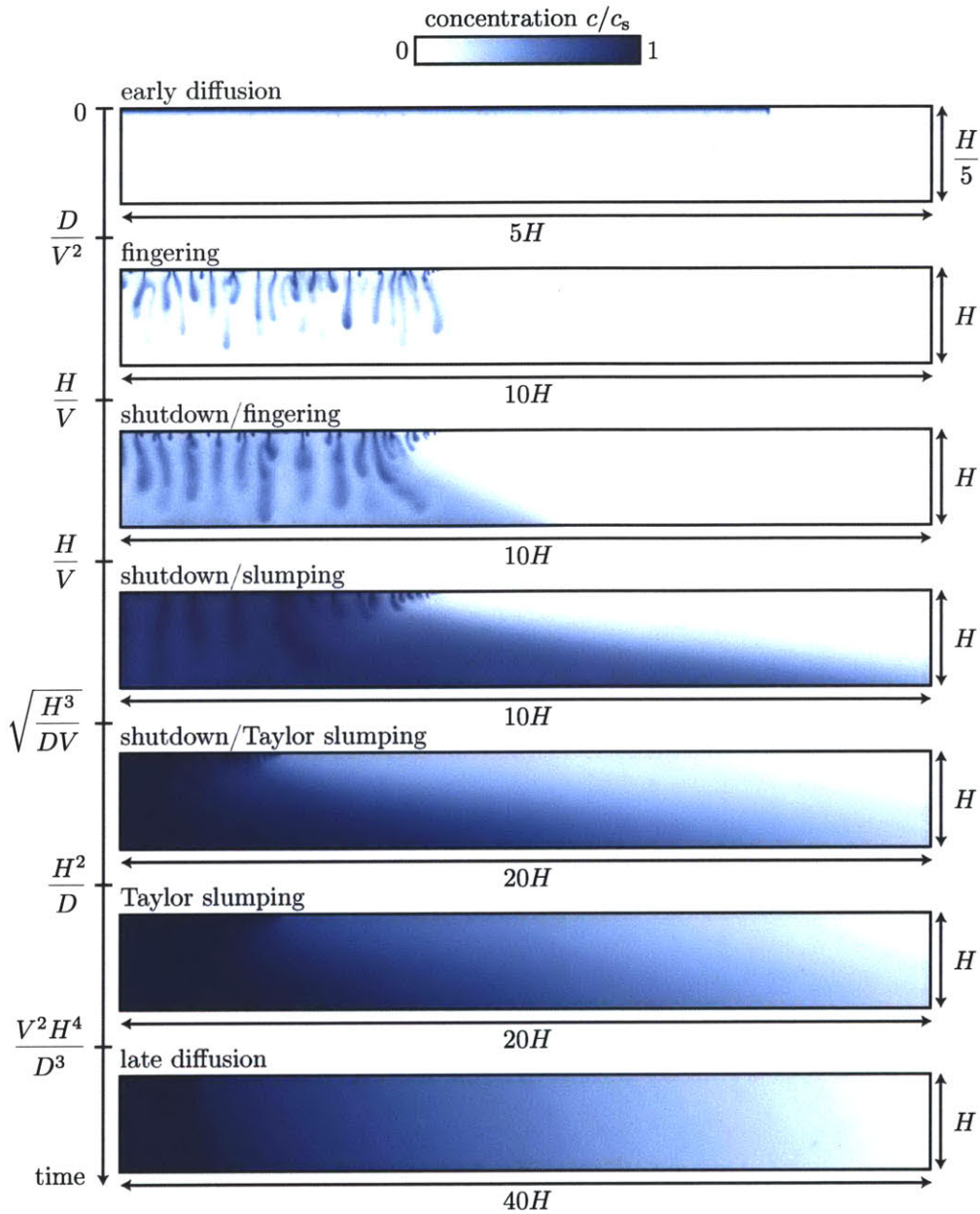
Figure 4-2: Dissolution evolves through the seven regimes shown here ($Ra = 3000$). The color scale represents the concentration of CO_2, c, normalized to the saturated concentration, c_s. The scalings of the transition times between the regimes are shown in terms of the layer thickness, H, the diffusion coefficient, D, and the characteristic velocity, $V = \Delta \rho g k / \mu \phi$ (see §4.3). When $Ra = VH/D$ is sufficiently small, the first and final transition times become equal, the duration of the intermediate regimes becomes zero, and the system transitions directly to the late diffusion regime.

4.3 Governing equations

Under the Boussineq approximation, the density-driven flow of incompressible, miscible fluids in a porous medium is described by the following system of equations [127]:

$$\boldsymbol{\nabla} \cdot \boldsymbol{u} = 0, \tag{4.1}$$

$$\boldsymbol{u} = -\frac{k}{\mu\phi} \left(\boldsymbol{\nabla} p - \rho(c)g\hat{\boldsymbol{z}} \right), \tag{4.2}$$

$$\frac{\partial c}{\partial t} + \boldsymbol{u} \cdot \boldsymbol{\nabla} c - D\nabla^2 c = 0. \tag{4.3}$$

Equation 4.1 expresses conservation of mass for the entire fluid mixture, equation 4.2 is Darcy's law, and equation 4.3 is the concentration equation. The variables are as follows: c is the CO_2 concentration, D is the diffusion coefficient, $\boldsymbol{u} = (u, v)$ is the pore velocity, k is the permeability, μ is the dynamic viscosity, ϕ is the porosity, p is the pressure, g is the gravitational acceleration, and ρ is the density. We assume that density is a linear function of the concentration: $\rho = \rho_0 + \Delta\rho\frac{c}{c_s}$, where $\Delta\rho$ is the density difference between water and CO_2-saturated water, and c_s is the saturated concentration of CO_2. Substituting Darcy's law into equation 4.1 yields the pressure equation:

$$\nabla^2 p = g\frac{\partial\rho}{\partial z}. \tag{4.4}$$

Taking the curl of Darcy's law yields the vorticity equation:

$$\omega = \frac{\partial u}{\partial z} - \frac{\partial v}{\partial z} = -V\frac{\partial c'}{\partial x}, \tag{4.5}$$

where ω is the vorticity in the y-direction (see figure 4-1), c' is the concentration normalized to the saturated concentration ($c' = c/c_s$), and $V = \Delta\rho gk/\mu\phi$ is the characteristic buoyancy velocity. This equation shows that lateral concentration gradients drive vortical flow.

The initial condition is that the velocity and concentration are zero everywhere:

$$\boldsymbol{u}(x, z, t = 0) = \boldsymbol{0}, \qquad c(x, z, t = 0) = 0. \tag{4.6}$$

The boundary condition for the concentration equation along the top of the layer is defined

129

piecewise:

$$c(z = 0, -W \leq x \leq 0) = c_{\mathrm{s}}, \qquad \left. \frac{\partial c}{\partial z} \right|_{z=0, x>0} = 0, \qquad (4.7)$$

where W is the width of the CO_2 source (figure 4-1). For most of the study, we perturb the constant-concentration boundary condition with random noise of magnitude $\varepsilon = 1 \times 10^{-3} c_{\mathrm{s}}$. The remaining boundary conditions are no-diffusion on the bottom and left walls and no-flow on all walls; the right wall is infinitely far away:

$$v(z = 0, H) = u(x = -W, \infty) = \left. \frac{\partial c}{\partial z} \right|_{z=H} = \left. \frac{\partial c}{\partial x} \right|_{x=-W,\infty} = 0. \qquad (4.8)$$

The key variable we use to parametrize the system is the mean dissolution flux. The point flux, f, is defined at every location along the CO_2 source via Fick's law; the mean flux, $\overline{f}$, is the lateral average:

$$f(x, t) = -D \left. \frac{\partial c}{\partial z} \right|_{z=0}, \qquad \overline{f}(t) = \frac{1}{W} \int_{-W}^{0} f(x, t) \, dx. \qquad (4.9)$$

When all the equations are made dimensionless, there are two governing parameters. One is the Rayleigh number, $Ra = VH/D$, which compares the strength of advection to diffusion. The second is the dimensionless width of the CO_2 source. For early regimes at high Rayleigh numbers, we use the most unstable wavelength, λ_{c}, to non-dimensionalize the width; this parameter roughly reflects the characteristic finger width immediately after the onset of fingering. Based on the results of stability analyses, we define the most unstable wavelength to be $\lambda_{\mathrm{c}} = 90D/V^2$ [48, 167, 138], which qualitatively agrees with our numerical results. For late regimes after the fingers reach the bottom of the layer, we typically use the layer thickness, H, to non-dimensionalize the width. Since we expect the length of the CO_2-brine interface to be larger than the reservoir thickness in practice, we focus on systems for which $W \geq 4H$.

In general, we solve the governing equations numerically. We integrate the pressure equation using finite volumes and solve it with a fast Poisson solver. To solve the concentration equation (eq 4.3), we also integrate using finite volumes, but additionally employ linear reconstructions and the MC limiter to maintain second-order accuracy [101]. We integrate in time using Runge-Kutta methods [94]: for short-time simulations, we use an explicit, two-stage method, and for longer simulations, we switch to an implicit-explicit two-

stage method to remove the time-step restriction from the diffusion term [6]. Both time integration methods are second-order accurate. We have performed a convergence analysis to confirm that the numerical method and discretizations used are sufficient to quantify the dissolution flux accurately.

4.4 Dissolution regimes

4.4.1 Early diffusion (ed)

At the earliest times, dissolution occurs via diffusion without convective enhancement in regions far from the edge of the source. This process creates a diffuse layer of CO_2-rich fluid directly under the top boundary.

At the edge of the source, however, convection begins immediately since the smallest amount of diffusion leads to a lateral concentration gradient there, which drives vortical flow (eq. 4.5). For $Ra \gtrsim 55$, this flow creates a single finger at the edge (figure 4-3a), as has been observed in the Elder and salt-lake problems [45, 165, 166]. The propagation of this finger perturbs a neighboring region of the diffuse, CO_2-rich boundary layer, which locally destabilizes the layer and creates an adjacent finger (figure 4-3b). This process successively triggers fingering along the source until other perturbations—either numerical or physical—destabilize the entire boundary layer (figure 4-3c). For the remainder of the study, we impose random perturbations in the constant-concentration boundary of magnitude $\varepsilon = 1 \times 10^{-3} c_s$, for which only one or two fingers form at the edge before the entire boundary layer destabilizes (figure 4-3d). This decision was motivated by the expectation that large perturbations will be present during CO_2 storage in real geologic traps.

When the length of the CO_2 source is large, the initial convection exerts a negligible effect on the mean dissolution flux. For the perturbation we impose and $Ra \lesssim 55$, the initial convection is negligible provided $W \geq 4H$. For $Ra \gtrsim 55$, fingering occurs at the edge, so the domain must be much larger than the characteristic width of a finger for the fingering process to be negligible. Numerically, we find that convection is negligible provided $W > 30\lambda_c$. When convection is negligible, the flux may be modeled by the flux for a 1D-diffusion problem in a semi-infinite domain [31],

$$\overline{f}_{\text{ed}} = c_{\text{s}} \left(\frac{D}{\pi t} \right)^{1/2} , \qquad (4.10)$$

131
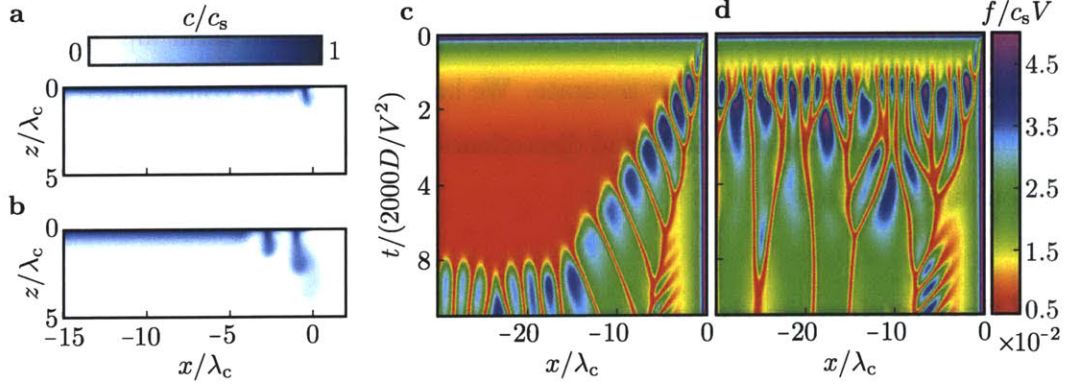
Figure 4-3: Initially, dissolution occurs via diffusion without convection along the interior of the CO_2 source, but convection occurs immediately at the edge (all results for $Ra = 4000$). **a.** Convection causes a single finger to form at the edge for high Ra ($t = 927D/V^2$, $\lambda_c = 90D/V$). **b.** This finger triggers the formation of an adjacent finger ($t = 3015D/V^2$). **c.** Fingering propagates inward until the entire source becomes unstable. This process is reflected in the point fluxes along the source: since finger roots are highly saturated, the vertical concentration gradient immediately above a finger is small, and the dissolution flux is therefore also small. As a result, the dark red branches in the surface plot of the point fluxes trace the finger movements. Here, a small perturbation is present ($\varepsilon = 1 \times 10^{-14} c_s$), so the fingering front can advance far to the left before the perturbation triggers fingering everywhere. **d.** When a larger perturbation is present ($\varepsilon = 1 \times 10^{-3} c_s$), the perturbation triggers fingering across the whole source relatively quickly before the fingering front can advance far from the edge.

as shown in figure 4-4.

The diffusion model is valid before the system transitions to the next regime, which depends on the Rayleigh number. For $Ra \lesssim 55$, the next regime is late diffusion and the transition occurs when the diffusion front reaches the bottom of the layer: $t_{ld1} = H^2/D$ (figure 4-4**a**). For $Ra \gtrsim 133$, the next regime is fingering and the transition occurs at $t_f = \psi D/V^2$, as found in previous studies [48, 167, 138, 64, 143]. The constant ψ depends on the criterion used to define the onset of fingering. Here, we define the onset as the time when the mean flux reaches a local minimum before rising sharply due to fingering (figure 4-4**b**). Based on this criterion, we find that $\psi \approx 2000$. For intermediate Rayleigh numbers, $55 \lesssim Ra \lesssim 133$, the subsequent regime is unclear so the transition is not well defined; however, we find that the diffusion solution is valid until a time between t_{ld1} and t_f.

4.4.2   Fingering (f)

In the fingering regime, CO_2 diffuses into a thin boundary layer that breaks up into sinking fingers. Over the interior of the CO_2 source, this behavior is nearly identical to the fingering
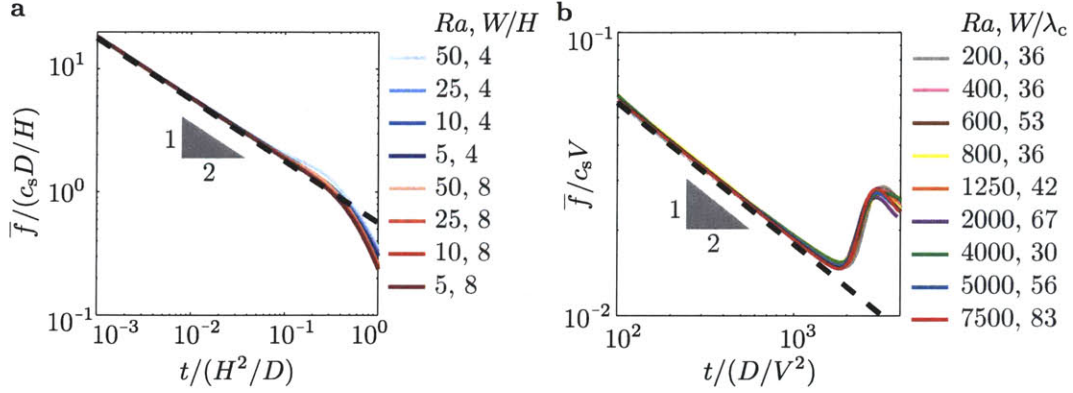
132

Figure 4-4: During the early diffusion regime, the mean dissolution flux, $\overline{f}$, can be modeled by the flux from a 1D diffusion problem (dashed lines; eq 4.10), provided the source is large enough for edge convection to be negligible. **a.** For $Ra \lesssim 55$, edge convection is negligible provided $W \gtrsim 4H$, and all numerically-measured fluxes (colored) collapse to the diffusion solution. This solution becomes invalid at $t_{ld1} \sim H^2/D$, when the system transitions to the late diffusion regime. **b.** For $Ra \gtrsim 133$, all numerically-measured fluxes (colored) collapse to the diffusion solution provided $W \gtrsim 30\lambda_c$. The diffusion solution becomes invalid at $t_f \sim D/V^2$, when the system transitions to the fingering regime.

process described in previous studies: as the fingers fall, relatively unsaturated water simultaneously rises to the source, which maintains large concentration gradients that increase the dissolution rate compared to the previous regime. Near the edge of the source, however, the unsaturated water comes dominantly from the porous layer outside the source region (figure 4-5**a**). Since the water does not travel upward between descending fingers to reach the source, it is nearly completely unsaturated, leading to higher dissolution fluxes than in the interior (figure 4-5**b**). These fluxes are similar in magnitude to those that occur immediately after the onset of fingering, when the dissolution flux reaches a local maximum [144]. Directly at the edge, the inflow of water stabilizes a small boundary layer, which can be modeled with the boundary layer solution derived by Cheng and Chang [27] (figure 4-5**c**).

For $Ra \gtrsim 2000$, the mean dissolution flux during the fingering regime oscillates, but remains approximately constant in time (figure 4-5**d**). Since the fluxes near the edge are larger than those in the interior, the value of the mean flux depends on the size of the CO_2 source. We find that when the source is larger than about $100\lambda_c$, the mean flux converges to

$$\overline{f}_f \approx 0.017 c_s V, \qquad (4.11)$$

in agreement with previous results (figure 4-5**e**) [135, 69]. The flux begins to decrease from this value at about $t_{sf} = 15H/V$, which is the time required for dissolved CO_2 to sink to the bottom in fingers and then recirculate back the the top boundary.

133

For $133 < Ra < 2000$, the flux rises to a peak after the onset of fingering and then continually declines with minor oscillations, as observed in previous work [64]. While the flux fails to exhibit a steady steady, equation 4.11 provides a lower bound on the flux. Since the flux continually declines, the transition to the next regime is not well defined, but we adopt the transition time for higher Rayleigh numbers ($t_{sf} = 15H/V$) and find agreement with numerical results.

4.4.3 Shutdown/fingering (sf)

During the shutdown/fingering regime, the source region exhibits three zones of different behavior (figure 4-6a). In the inner zone, dissolved CO_2 sinks to the bottom of the layer in fingers and then recirculates back to the top boundary, where it reduces the concentration gradients and therefore also the dissolution fluxes. This behavior is essentially identical to the convective shutdown behavior observed in closed systems [68, 144]. In the *outer zone*, fingering occurs in the unsaturated water that flows in from the porous layer outside the source region. This inflow is the counter-current to the flow of dense, CO_2-rich fluid that migrates away from the source along the bottom of the layer (figure 4-6a). In the *middle zone*, dissolved CO_2 from the outer zone enters from the right and flows to the left along the top part of the layer (figure 4-6b). CO_2 also dissolves via fingering in this zone, but the fingers dominantly remain in the top part of the layer; this is reflected in the observation that the vertical velocities go to zero along the midline of the layer (figure 4-6c). As the flow advances toward the interior, dissolution continues until the concentration rises to values similar to those in the inner zone, at which point the horizontal velocities become very small and the dissolved CO_2 sinks to the bottom. In the bottom part of the layer, the dissolved CO_2 flows to the right as a dense gravity current and eventually leaves the source region.

To model the mean dissolution flux in this regime, we first obtain models for each of the three zones, focusing on high-Ra systems ($Ra \gtrsim 2000$). In the outer zone, the dissolution mechanism is very similar to the previous regime and the mean dissolution flux can be modeled with the previous result: $\overline{f}_{oz} = 0.017c_sV$. While the actual flux is slightly higher due to the inflow of nearly completely unsaturated water, we use this value for simplicity and find it to be sufficiently accurate. This zone extends over the range $x_{mz} \leq x \leq 0$, where x_{mz} is the right boundary of the middle zone (figure 4-6a). We find empirically that $x_{mz} \approx -0.3H$.
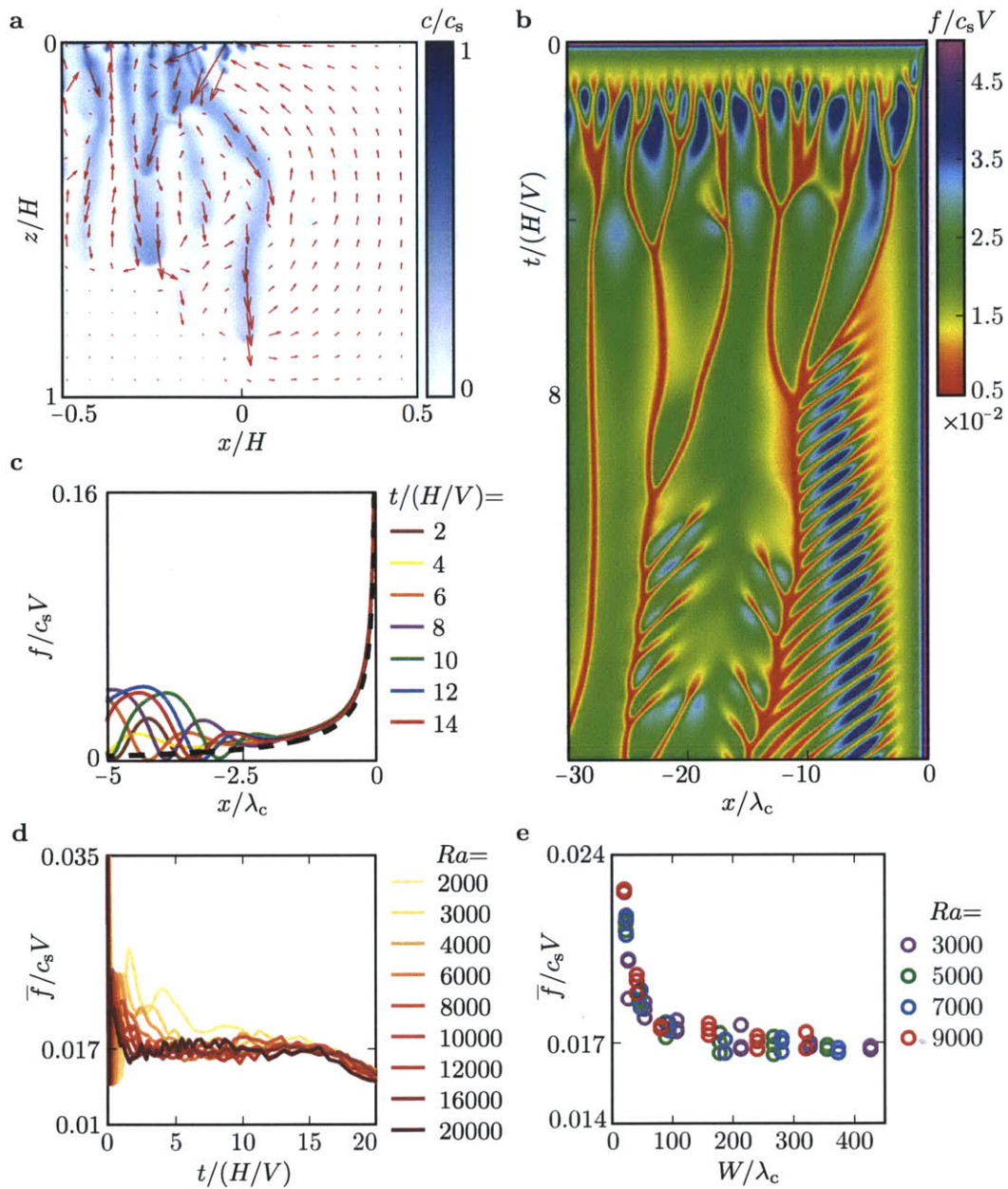
Figure 4-5: During the fingering regime, CO_2-rich fingers fall to the bottom of the layer and fresh water circulates to the source. **a.** Over the interior of the source, the unsaturated water comes from below; at the edge, it comes from the porous layer to the right (shown for $Ra = 10,000$). **b.** The inflow of water from outside the source region sweeps fingers to the interior, as shown by the repetition of diagonal red branches along the right side of the surface plot ($Ra = 10,000$). The blue regions between the branches indicate that the fluxes are higher near the edge than in the interior. **c.** A stable boundary layer exists directly at the edge. Numerical measurements of the flux there (colored) agree with the analytical solution (dashed). **d.** For $Ra \gtrsim 2000$, the mean dissolution flux oscillates but is approximately constant in time ($W \gg 100\lambda_c$). **e.** When the length of the CO_2 source is larger than about $100\lambda_c$, the mean flux converges to $\overline{f} \approx 0.017 c_s V$.
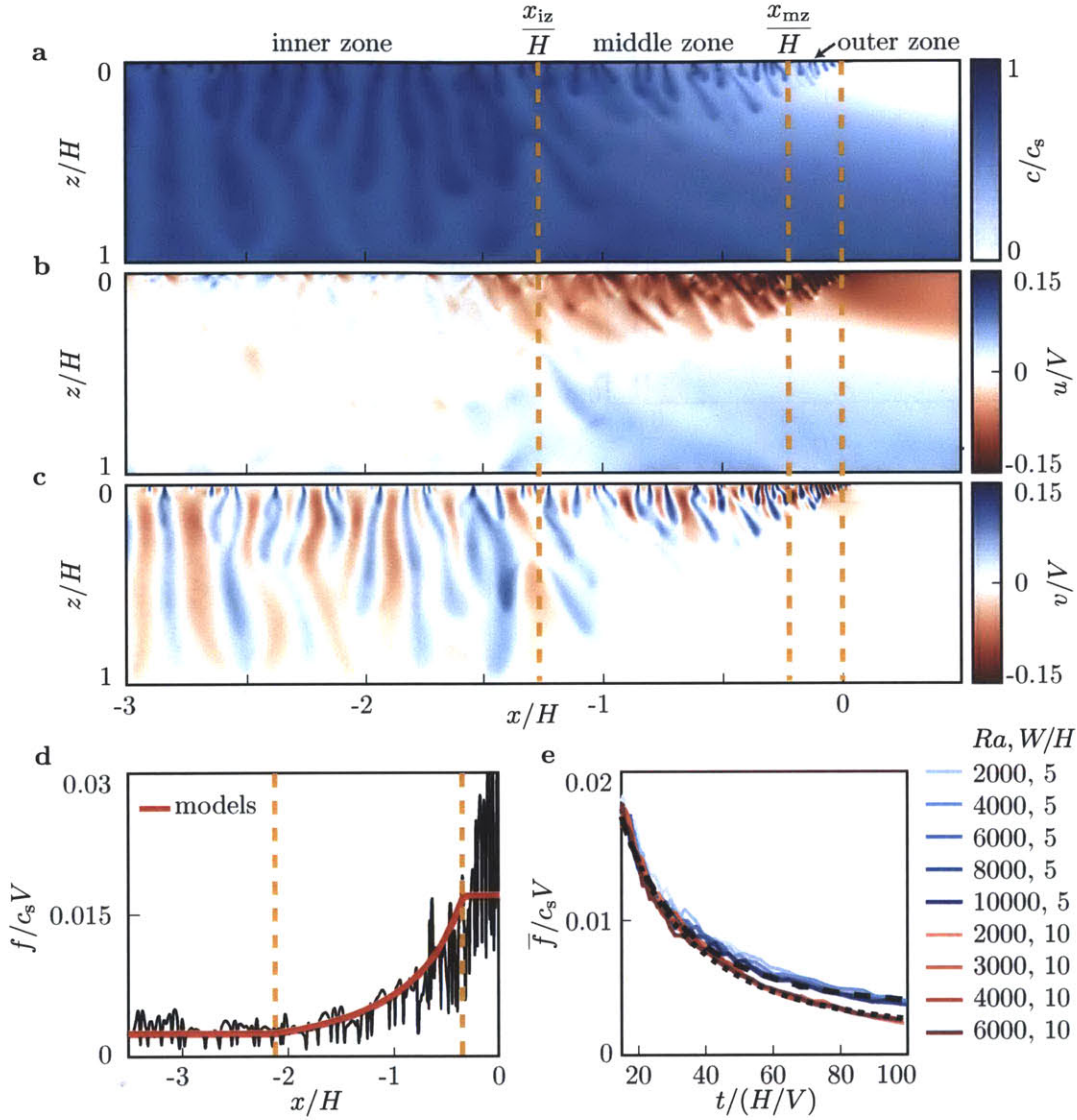
Figure 4-6: In the shutdown/fingering regime, the source region can be divided into three zones (dashed orange lines). **a.** In the inner zone, dissolution decreases due to the accumulation of dissolved CO_2. In the outer zone, dissolution remains at relatively high rates due to the inflow of unsaturated water along the top of the layer. In the middle zone, the dissolution rate transitions between the neighboring zones. **b.** The horizontal velocities in the middle zone are dominantly to the left in the upper part of the layer, sweeping dissolved CO_2 toward the interior. In the lower part of the layer, they are dominantly to the right, carrying dissolved CO_2 outside of the source region. **c.** The vertical velocities in the middle zone are large in the upper part of the layer but nearly vanish at the centerline, indicating that fingering is mostly confined to the top. **d.** Analytical models for the dissolution flux in each zone (red; eqs 4.13, 4.16, and 4.11) agree well with numerically-measured fluxes along the source (black). **e.** We average the flux models from each zone to find the mean dissolution flux over the entire source. The averaged model (long dashed: $W = 5H$, short dashed: $W = 10H$; eq 4.18) agrees well with numerical results for $Ra \gtrsim 2000$.

136

In the inner zone, dissolution occurs via the convective shutdown mechanism described by Hewitt et al. [68] and Slim et al. [144], and can be modeled with the box models they derived:

$$\overline{\overline{c}}_{iz} = 1 - (1 + \kappa(t - t_0)V/H)^{-1}, \tag{4.12}$$

$$\overline{f}_{iz} = c_s V \kappa \left(1 - \overline{\overline{c}}_{iz}\right)^2. \tag{4.13}$$

Here, $\overline{\overline{c}}_{iz}$ is the dimensionless mean concentration in the inner zone (double overbars denote averaging over both vertical and horizontal dimensions), $\overline{f}_{iz}$ is the mean dissolution flux into the inner zone, t_0 is a virtual time origin, and κ is a constant. Slim et al. [144] used the ad hoc value of $\kappa = 0.05$, and Hewitt et al. [68] derived the value to be $\kappa = 0.028$ based on analogy to Rayleigh-Bénard convection; both used $t_0 = 0$. We empirically find that $\kappa = 0.028$ and $t_0 = 5H/V$ provide the best fit to the data.

In the middle zone, we develop a model for the upper part of the layer that couples horizontal advection and dissolution due to fingering. To derive the model, we vertically average the concentration equation (eq 4.3) and make several assumptions. We assume that diffusion is negligible compared to advection outside the boundary layer at $z = 0$, and that the horizontal velocity in the upper part of the layer, u_{mz}, is independent of both x and z. Numerical results show that this is not strictly true, but we find that this simplification captures the general behavior and yields acceptable results. We also assume that the vertical mass flux from the upper part of the layer to the lower part is negligible. This assumption is valid over most of the middle zone since the high CO_2 concentrations in the underlying gravity current cause the vertical velocities to become negligibly small along the midline of the layer (figure 4-6c). The assumption is invalid at the left boundary of the zone were nearly all the dissolved CO_2 sinks to the bottom layer, but we find that this region is small and has a minor impact on the results. Finally, we assume that the dissolution flux can be modeled with the expression from the convective shutdown model, equation 4.13. Since the convective shutdown model is derived via horizontal averaging over several finger widths, this assumption causes our model to capture behavior at the scale of several fingers.

Under these assumptions, we derive an advection equation that incorporates the expression for the dissolution flux from the shutdown model (eq 4.13) as a forcing term:

$$\frac{\partial \overline{c}}{\partial t} + u_{mz} \frac{\partial \overline{c}}{\partial x} = \frac{V\kappa}{\eta} \left(1 - \overline{c}\right)^2, \tag{4.14}$$

where η is the thickness of the upper layer and overbars denote vertical averages over η. For the boundary condition, we fix the concentration at the right boundary: $\overline{c}'(x = x_{\mathrm{mz}}) = \overline{c}'_{\mathrm{R}}$, where $\overline{c}'_{\mathrm{R}}$ is the vertically averaged concentration that enters from the outer zone. Based on numerical observations, the behavior in the upper layer is essentially time invariant, so we solve the equation at steady state::

$$\overline{c}'_{\mathrm{mz}} = 1 - \left(\frac{V\kappa}{u_{\mathrm{mz}}\eta} (x - x_{\mathrm{mz}}) + \frac{1}{1 - \overline{c}'_{\mathrm{R}}} \right)^{-1}, \tag{4.15}$$

$$\overline{f}_{\mathrm{mz}} = c_{\mathrm{s}} V\kappa \left(\frac{V\kappa}{u_{\mathrm{mz}}\eta} (x - x_{\mathrm{mz}}) + \frac{1}{1 - \overline{c}'_{\mathrm{R}}} \right)^{-2}. \tag{4.16}$$

Since the model is a hyperbolic equation, the position of the downstream boundary to the left, x_{iz}, was not required for the solution. We define the location of this boundary *a posteriori* as the point at which the vertically averaged concentration in the middle zone equals the mean concentration in the inner zone. Equating equations 4.12 and 4.15, we find:

$$x_{\mathrm{iz}} = x_{\mathrm{mz}} + \frac{u_{\mathrm{mz}}\eta}{V\kappa} \left(\kappa (t - t_0) \frac{V}{H} - \frac{\overline{c}'_{\mathrm{R}}}{1 - \overline{c}'_{\mathrm{R}}} \right). \tag{4.17}$$

Based on this definition, the location of the left boundary continually moves toward the interior as the inner region becomes more saturated, which agrees with observations from the simulations. We set the thickness of the top layer and the velocity empirically from numerical data: $\eta = 0.3H$ and $u_{\mathrm{mz}} = -0.07V$. We set the mean concentration at the right boundary to ensure continuity of the dissolution flux with the outer zone: $\overline{c}'_{\mathrm{R}} = 1 - (\overline{f}_{\mathrm{oz}}/\kappa)^{1/2} = 0.22$ (see eq 4.13). This value matches observations from the simulations (figure 4-6a).

We find that, for $Ra \gtrsim 2000$, the dissolution flux at every location along the CO_2 source can be approximated by combining the models for each of the three zones (figure 4-6d). To determine the mean dissolution flux over the source, we average the models:

$$\overline{f}_{\mathrm{sf}} = \frac{1}{W} \left[\int_{-W}^{x_{\mathrm{iz}}} \overline{f}_{\mathrm{iz}} dx + \int_{x_{\mathrm{iz}}}^{x_{\mathrm{mz}}} \overline{f}_{\mathrm{mz}} dx + \int_{x_{\mathrm{mz}}}^{0} \overline{f}_{\mathrm{oz}} dx \right], \tag{4.18}$$

As shown in figure 4-6e, the solution for the mean flux agrees with numerical measurements. The solution becomes inaccurate at roughly $t_{\mathrm{ss}} = 100H/V$, when the system transitions to the next regime.

4.4.4 Shutdown/slumping (ss)

In the shutdown/slumping regime, the source region exhibits two zones of different behavior (figure 4-7a). In the inner zone, the dissolution mechanism is the same as in the previous regime: convective shutdown. In the outer zone, the mechanism is similar to that in the previous regime: dissolution occurs via fingering into relatively unsaturated fluid that flows in from the layer outside the source region. As before, this flow is the counter current to the dense, CO_2-rich gravity current that slumps away from the source. The difference is that, in this regime, the extent of the gravity current is large relative to the thickness of the layer, and as a result, the flux of CO_2 out of the source region continually decreases with time. Since the outer zone is nearly saturated, this causes the dissolution flux into the outer zone to also continually decrease with time, whereas previously it was constant.

To model dissolution in the outer zone, we develop a box model that relates the mean dissolution flux to the flux into the dense gravity current. To derive the model, we average the concentration equation (eq 4.3) over the outer zone in both the vertical and horizontal directions:

$$\frac{\partial \overline{\overline{c}}_{oz}}{\partial t} = \frac{1}{|x_{iz}|}\left(\overline{f}_h(x = x_{iz}) - \overline{f}_h(x = 0)\right) + \frac{1}{H}\overline{f}_{oz}. \qquad (4.19)$$

$\overline{\overline{c}}_{oz}$ is the dimensionless mean concentration in the outer zone, $\overline{f}_h(x = x_{iz})$ is the mean horizontal mass flux from the inner zone to the outer zone, $\overline{f}_h(x = 0)$ is the mean horizontal mass flux from the outer zone into the gravity current, and $\overline{f}_{oz}$ is the mean dissolution flux into the outer zone (figure 4-7a). When the accumulation term on the left and the mean flux from the inner zone to the outer zone are negligible, the equation becomes

$$\overline{f}_{oz} = \frac{H}{|x_{iz}|}\overline{f}_h(x = 0), \qquad (4.20)$$

which states that the mean dissolution flux in the outer zone is directly proportional to the flux into the gravity current. Based on numerical results, we find that the flux from the inner zone to the outer zone is approximately zero when $x_{iz} = 3H$ (figure 4-7c). In contrast to the previous regime, the location of the boundary is fixed in this regime.

To quantify the flux into the gravity current, we model the migration of the current. We assume that vertical velocities in the current are negligible compared to the horizontal velocities (Dupuit approximation), which is justified by the large lateral extent of the current

139

relative to its height in this regime [17]. We also assume sharp interfaces. Since diffusion is the only mechanism by which mass enters the system, the interface is always diffuse, but we treat is as sharp for simplicity and find agreement with numerical results for high Rayleigh numbers ($Ra \gtrsim 2000$). Under these assumptions, the height of the sharp interface, h, can be modeled by the following equation [17, 34, 77]:

$$\frac{\partial h}{\partial t} - V \frac{\partial}{\partial x}\left[h\left(1 - \frac{h}{H}\right)\frac{\partial h}{\partial x}\right] = 0, \tag{4.21}$$

where h is measured from the bottom of the layer. We solve this equation in a semi-infinite domain with the left boundary fixed at the right edge of the source region. For the left boundary condition, we fix the height of the current at $x = 0$ to be $h = 0.7H$ based on the observation that the current remains pinned at the edge of the source. We transform the equation into a self-similar form using the similarity variable $\xi_{ss} = x/(VHt)^{1/2}$, and then integrate it numerically. We find that the solution matches the gravity current in the full, 2D simulations (figure 4-7b). From the solution, we calculate the mass flux into the current to be

$$\overline{f}_h(x = 0) = \frac{1}{H}\frac{d}{dt}\left(c_c \int_0^{x_n} h\, dx\right) = 0.26 c_c \left(\frac{HV}{t}\right)^{1/2}, \tag{4.22}$$

where x_n is the rightmost edge of the current at which $h = 0$ and c_c is the concentration of the current, which we set empirically to $0.65 c_s$. This expression shows that the flux into the gravity current decreases diffusively in time with the scaling $t^{-1/2}$, which is due to the fact that the horizontal velocities in the current decrease diffusively in time.

To model the mean dissolution flux over the entire source, $\overline{f}_{ss}$, we average the fluxes from both zones:

$$\begin{aligned}
\overline{f}_{ss} &= \frac{1}{W}\left[\int_{-W}^{x_{iz}} \overline{f}_{iz}dx + \int_{x_{iz}}^{0} \overline{f}_{oz}dx\right], \\
&= c_s V \frac{1}{W}\left[(W - 3H)\kappa\left(1 + \kappa(t - t_0)\frac{V}{H}\right)^{-2} + 0.26H\frac{c_c}{c_s}\left(\frac{H}{Vt}\right)^{1/2}\right].
\end{aligned} \tag{4.23}$$

This expression agrees with numerical measurements of the mean flux (figure 4-7d). It becomes invalid at $t_{sT} = 6(H^3/VD)^{1/2}$, when the system transitions to the shutdown/Taylor slumping regime.
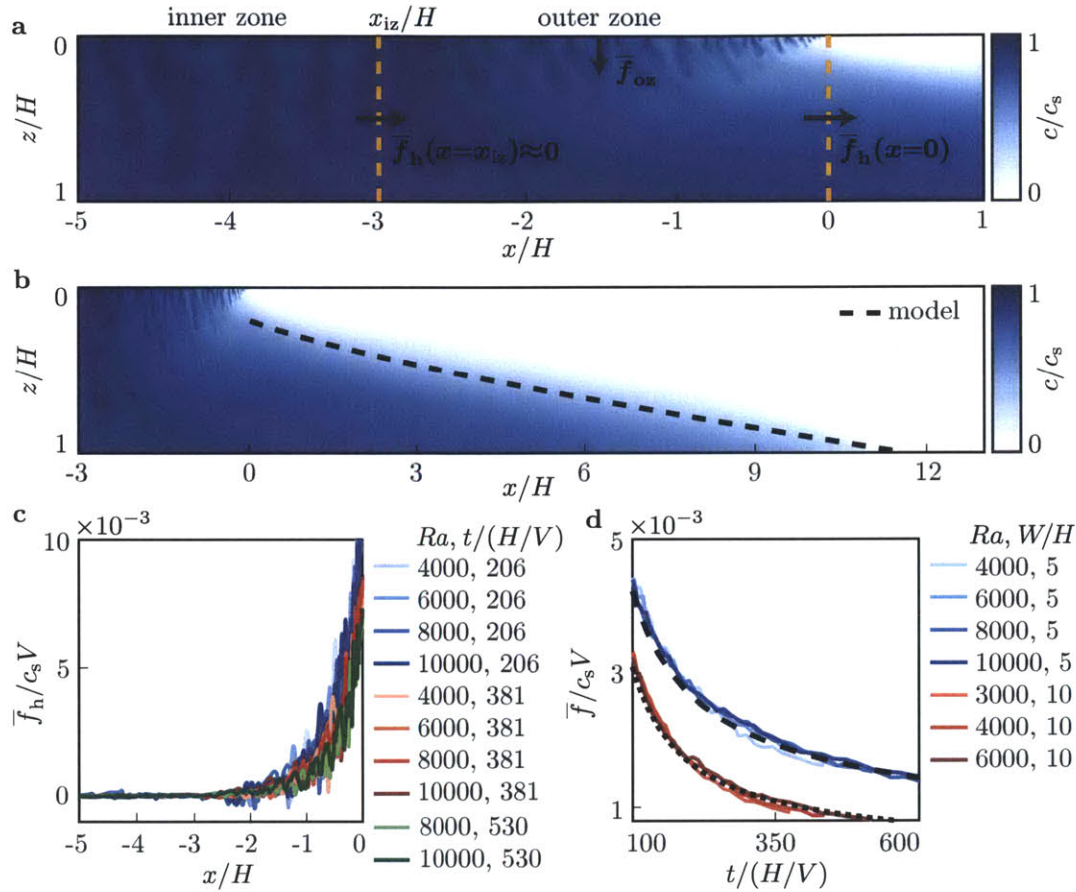
Figure 4-7: **a.** In the shutdown/slumping regime, the source region can be divided into two zones as shown by the dashed orange lines ($Ra = 10,000$). The inner zone is the same as in the previous regime. The flux into the outer zone, $\overline{f}_{oz}$, can be modeled from the flux into the dense gravity current, $\overline{f}_h(x = 0)$. **b.** The flux into the gravity current can be derived from a sharp-interface model of the current (dashed; eq 4.21), which matches the shape of the current from full, 2D simulations ($Ra = 10,000$). **c.** The flux into the current provides a good approximation of the flux into the outer zone when the flux between the two zones, $\overline{f}_h(x = x_{iz})$, is very small. Numerical measurements of the mean horizontal flux, $\overline{f}_h$, indicate that this can be achieved by placing the zone boundary at $x_{iz} = -3H$. **d.** The model for the mean dissolution flux over the entire source (short dashed: $W = 10H$, long dashed: $W = 5H$; eq 4.23) agrees with numerical results (colored). Data are truncated at the onset of the next regime for clarity.

4.4.5 Shutdown/Taylor slumping (sT)

In the shutdown/Taylor slumping regime, the source region can be divided into the same two zones present in the previous regime. The inner zone is exactly the same, with dissolution occurring via convective shutdown. The outer zone exhibits similar behavior to the previous regime in that the dissolution rate is limited by rate at which CO_2-rich fluid can slump away from the source region as a dense gravity current. It differs, however, in the nature of the gravity current. Whereas previously advection dominated diffusion, in this regime diffusion becomes equally important and a broad transition zone develops between the dense current and the over-riding counter-current (figure 4-2). As a result of diffusive mixing, the current decelerates faster than in the previous regime, and consequently the flux of CO_2 out of the source region also decreases faster. A complementary interpretation is that the dissolution flux decreases faster because the counter-current no longer supplies nearly unsaturated fluid to the source region, but rather fluid with high saturations of CO_2 originating from the dense gravity current.

To model the dissolution flux in the outer zone, we employ the box model from the previous regime that relates the dissolution flux to the flux into the dense gravity current (eq 4.20). However, to model the flux into the current, we now use a model that captures diffusive mixing between the dense current and the counter-current. The model, called the Taylor slumping model, is a partial differential equation for the vertically averaged concentration in the porous layer, $\bar{c}$ [148]:

$$\frac{\partial \bar{c}}{\partial t} - D\frac{\partial^2 \bar{c}}{\partial x^2} - \frac{\partial}{\partial x}\left(\frac{H^4 V^2}{120 D c_s^2}\left[\frac{\partial \bar{c}}{\partial x}\right]^2 \frac{\partial \bar{c}}{\partial x}\right) = 0. \tag{4.24}$$

The middle term in this equation is a Fickian diffusion term. The rightmost term can be interpreted as a nonlinear diffusion term that captures the coupling between Taylor dispersion at the aquifer scale and the reduction in lateral concentration gradients that drive flow [148]. Scaling these terms shows that the Fickian diffusion term is negligible compared to the nonlinear term when the aspect ratio of the current is small relative to the Rayleigh number: $L/H \ll Ra/\sqrt{120}$, where L is the lateral extent of the current. As a result, the nonlinear term dominates at early times before the current becomes too large, and we neglect the Fickian diffusion term until the last regime.

We solve the Taylor slumping equation in a semi-infinite domain with the left boundary

at the right edge of the source region. For the boundary condition, we fix the vertically averaged concentration to the completely saturated concentration ($\overline{c'}(x = 0) = 1$). Since the actual concentration at the boundary remains below saturation, this simplification introduces error in the model; however, the error decreases with time as the source region approaches saturation. We solve the equation analytically via a similarity solution in the variable $\xi_{Ts} = x/(H^4 V^2 t/120 D)^{1/4}$:

$$\frac{\overline{c}}{c_s} = 1 - \frac{1}{2\sqrt{12}} \left[\xi_{Ts} \left(\alpha^2 - \xi_{Ts}^2 \right)^{1/2} + \alpha^2 \arcsin \left(\frac{\xi_{Ts}}{\alpha} \right) \right], \tag{4.25}$$

where $\alpha = (198/\pi^2)^{1/4}$. This solution agrees with numerical measurements of the vertically averaged concentration. The agreement improves over time since the model is an asymptotic [148], and since the boundary condition becomes increasingly accurate with time (figure 4-8a). From the solution, we find the flux into the current:

$$\overline{f}_h(x = 0) = \frac{1}{H} \frac{d}{dt} \left(H \int_0^\infty \overline{c} \, dx \right) = c_s \left(\frac{8}{405 \pi^6} \right)^{1/4} \left(\frac{H^4 V^2}{D t^3} \right)^{1/4}. \tag{4.26}$$

This equation agrees with the numerically measured fluxes out of the source region (figure 4-8b). It shows that, in contrast to the previous regime, the flux into the gravity current decreases sub-diffusively. We find empirically that equation 4.26 becomes valid at time $t_{sT} = 6(T_A T_D)^{1/2} = 6(H^3/VD)^{1/2}$, where $T_A = H/V$ is the characteristic advection time across the layer and $T_D = H^2/D$ is the characteristic diffusion time across the layer. While the precise physical origin of this scaling is unclear, the dependence on both advection and diffusion timescales is reasonable since the model couples advection and diffusion.

While the convective shutdown mechanism continues to operate in the inner zone, we use an extended form of model from the previous regimes. The extended model captures behavior at low Rayleigh numbers and long times more accurately than the previous model. It was derived by Hewitt et al. [68]:

$$\overline{\overline{c}}_{iz} = 1 - \gamma \left[(1 + \gamma) e^{\kappa \gamma (t - t_0) V/H} - 1 \right]^{-1}, \tag{4.27}$$

$$\overline{f}_{iz} = c_s V \kappa \left[\left(1 - \overline{\overline{c}}_{iz} \right)^2 + \gamma \left(1 - \overline{\overline{c}}_{iz} \right) \right], \tag{4.28}$$

where $\gamma = \beta/\kappa Ra$ and $\beta = 2.75$. The previously used model can be derived from this model

143

when $\gamma \ll 1$. As with the previous model, this model agrees with numerical measurements of the dissolution flux in the inner zone (figure 4-8c).

To determine the mean dissolution flux over the source region, we average the fluxes in the inner and outer zones. The flux into the inner zone is given by the extended convective shutdown model (eq 4.28). The flux into the outer zone is given by combining the box model (eq 4.20) with the expression for the flux into the gravity current (eq 4.26). For the left boundary of the box model, we take $x_{iz} = -3H$ as in the previous regime. The mean dissolution flux is then

$$
\begin{aligned}
\overline{f}_{sT} &= \frac{1}{W} \left(\int_{-W}^{x_{iz}} \overline{f}_{iz} dx + \int_{x_{iz}}^{0} \overline{f}_{oz} dx \right), \\
&= \frac{1}{W} \left[(W - 3H)\overline{f}_{iz} + c_s H \left(\frac{8}{405\pi^6} \right)^{1/4} \left(\frac{H^4 V^2}{Dt^3} \right)^{1/4} \right],
\end{aligned}
\tag{4.29}
$$

where $\overline{f}_{iz}$ is given by eq 4.28. This expression agrees with numerically measured fluxes. The agreement improves for larger Rayleigh numbers because the shutdown model becomes more accurate for larger Rayleigh numbers. The agreement also improves with time as the Taylor slumping model becomes more accurate (figure 4-8d).

This validity of equation 4.29 is limited by the late-time validity of the convective shutdown model. We estimate the time at which the convective shutdown model becomes invalid as the time when the effective Rayleigh number, Ra_e, decreases to the critical value for convection, Ra_c. The effective Rayleigh number is based on the density difference between the saturated upper boundary and the fluid in the porous layer, and as a result, is a function of the mean concentration in the layer. Following Hewitt et al. [68], we define the effective Rayleigh number as $Ra_e = 4Ra(1 - \overline{\overline{c}}_{iz})$. The critical Rayleigh number in a Rayleigh-Bénard flow is $Ra_c = 4\pi^2$ [127]. While the present system is not a Rayleigh-Bénard problem, we take this value because the derivation of Hewitt et al. [68] is based on an analogy to Rayleigh-Bénard flow. Solving for the time at which $Ra_e = Ra_c$ yields $t_{Ts} = (H^2/D)(1/\beta) \ln[(4\beta/\kappa Ra_c)(1 + \gamma)^{-1}]$, which in the limit of large Ra ($\gamma \ll 1$) becomes $t_{Ts} \approx H^2/D$. Numerical results confirm the validity of the model until this time (figure 4-8c).
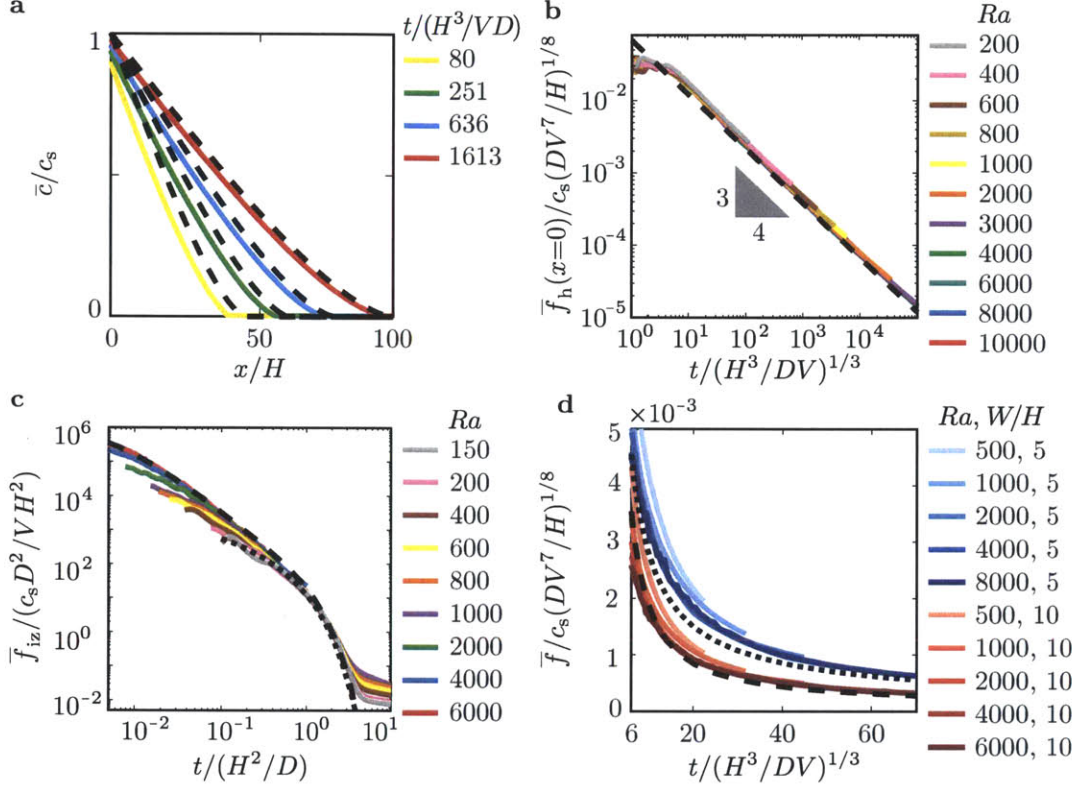
Figure 4-8: **a.** In the shutdown/Taylor slumping regime, the dissolution flux into the outer zone is controlled by the flux into a diffuse gravity current, which we model with the Taylor slumping model (eq 4.24). The model results for the vertically averaged concentration in the layer (dashed; eq 4.25) agree with numerical measurements (colored), particularly at late times. **b.** The model results for the flux into the gravity current (dashed; eq 4.26) agree with numerical measurements of the flux (colored) exiting the source region (all data for $W \geq 3H$). Data are truncated at the transition to the next regime for clarity. The simultaneous convergence of all data to the model indicates that the onset time of Taylor slumping scales as $t_{\mathrm{sT}} \sim (H^3/VD)^{1/2}$, which is the onset of the shutdown/Taylor slumping regime. **c.** In the inner zone, dissolution continues to occur via convective shutdown. In this regime, we use an extended form of the shutdown model (long dashed: $Ra = 6000$, short dashed: $Ra = 150$; eq 4.28), which describes the numerical fluxes (colored) for $Ra \gtrsim 133$ until $t_{\mathrm{Ts}} \sim H^2/D$, when the system transitions to the next regime. **d.** The model for the mean dissolution flux from the entire source (long dashed: $Ra = 6000, W = 10H$, short dashed: $Ra = 8000, W = 5H$; eq 4.29) agrees with numerical measurements (colored), particularly for large times and Rayleigh numbers. Again, data are truncated at the transition to the next regime for clarity.

145

4.4.6 Taylor slumping (Ts)

After time $t_{Ts} = H^2/D$, the interior of the source region is essentially completely saturated with CO_2 and convection becomes negligible there (figure 4-2). At the edge, convection slows but continues to enhance dissolution via the influx of water with relatively low CO_2 concentrations from the layer outside the source region. While the concentrations are low relative to the concentrations in the interior of the source where convection is nearly absent, they are near saturation due to diffusive mixing from the dense gravity current. This behavior is exactly the same as in the previous regime, but the concentrations in the inflow are higher since the dense gravity current is now longer.

To model the mean dissolution flux in this regime, we use a box model that spans the entire source region. As in the previous two regimes, the model relates the dissolution flux to the flux from the edge of the source into the layer. To model the flux into the layer, we again use the result from the Taylor slumping model (eq 4.26). The mean dissolution flux is:

$$\overline{f}_{Ts} = \frac{H}{W}\overline{f}_h(x = 0) = c_s\frac{H}{W}\left(\frac{8}{405\pi^6}\right)^{1/4}\left(\frac{H^4V^2}{Dt^3}\right)^{1/4}. \tag{4.30}$$

This equation represents a lower bound on the dissolution flux since it assumes that the accumulation of CO_2 in the entire source region is negligible. In practice, the accumulation is non-zero, but approaches zero with time as the layer becomes completely saturated. The equation agrees with numerical results (figure 4-9a).

4.4.7 Late diffusion (ld)

At the latest times, convection is negligible relative to diffusion over the entire domain. The dominant dissolution mechanism is diffusion without convective enhancement at the edge of the source, and the dominant transport mechanism outside the source region is lateral diffusion through the porous layer. For high Rayleigh numbers ($Ra \gtrsim 133$), this behavior occurs when the dense gravity current that transports CO_2 away from the source becomes very long. When the current becomes long, the horizontal density gradient that drives the flow becomes very small and, as a result, the velocity becomes very small. The relationship between the lateral velocity, u, and the gradient of vertically-averaged density, $\overline{\rho}$, is

$$u(z) = \frac{gkH}{\phi\mu}\frac{\partial\overline{\rho}}{\partial x}\left(\frac{1}{2} - \frac{z}{H}\right) + O(\epsilon^2), \tag{4.31}$$
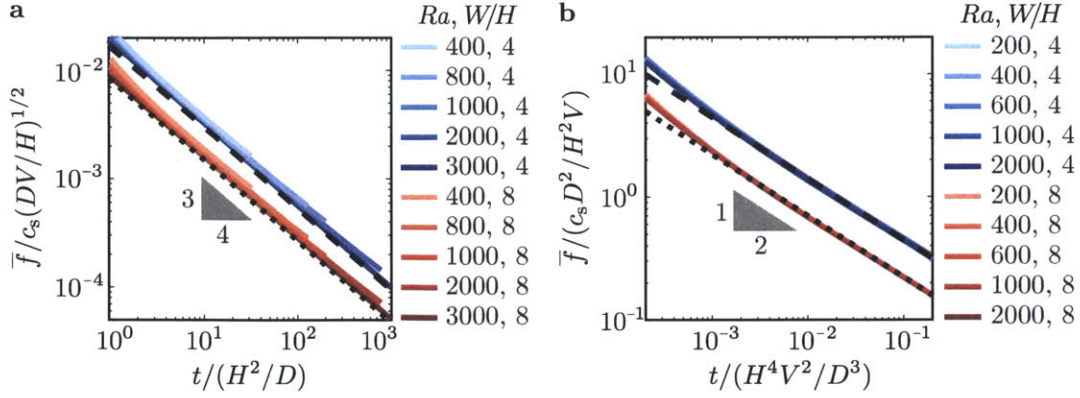
146

Figure 4-9: In the last two regimes, Taylor slumping and late diffusion, we model the mean dissolution flux using only the horizontal flux out of the source region. **a.** Numerical measurements of the dissolution flux (colored) in the Taylor slumping regime agree with the model (long dashed: $W = 4H$, short dashed: $W = 8H$; eq 4.30). The data are truncated at the onset of the next regime for clarity. **b.** Numerical measurements of the dissolution flux (colored) in the late diffusion regime also agree with our model (long dashed: $W = 4H$, short dashed: $W = 8H$; eq 4.32). The simultaneous convergence of numerical results to the model indicates that, for $Ra \gtrsim 133$, the onset time of late diffusion scales as $t_{\mathrm{ld2}} \sim H^4 V^2/D^3$.

where $\epsilon = H/L$ and L is the horizontal extent of the flow [148]. By equating the flux from lateral diffusion (eq 4.32) with the flux from Taylor slumping (eq 4.30), we find the time at which diffusion dominates to be $t_{\mathrm{ld2}} = (8/405\pi^4)(H^4 V^2/D^3)$.

For lower Rayleigh numbers, the transition to dissolution via lateral diffusion occurs at a different time. For $Ra \lesssim 55$, the previous regime is early diffusion, in which dissolution occurs dominantly via diffusion in the vertical direction without convective enhancement. When vertical diffusion is the preceding mechanism, the transition occurs when the diffusion front reaches the bottom of the layer at approximately $t_{\mathrm{ld1}} = H^2/D$, as discussed previously.

To model the dissolution flux, we use a box model that spans the entire source region as in the previous regime. To model the lateral flux out of the source region, we use the flux from a 1D diffusion problem in a semi-infinite domain. The mean dissolution flux is then:

$$\overline{f}_{\mathrm{ld}} = \frac{H}{W}\overline{f}_{\mathrm{h}}(x = 0) = \frac{H}{W}c_{\mathrm{s}}\left(\frac{D}{\pi t}\right)^{1/2}. \tag{4.32}$$

This is the same equation as for the first regime (eq 4.10), but with an additional dependence on the ratio of the layer thickness, H, to the width of the source, W. This dependence indicates that when the source width is large relative to the layer thickness, the late-time dissolution flux will be smaller than the early-time flux since all the mass transfer must

occur though a smaller space. This solution agrees with numerically measured dissolution fluxes (figure 4-9b).

4.5 Summary of regimes

We classify dissolution into seven regimes. In the early diffusion regime, dissolution occurs dominantly via diffusion without convective enhancement. In the fingering regime, dense, CO_2-rich fluid sinks away from the source in fingers while relatively unsaturated fluid rises upward, leading to an elevated dissolution flux that is approximately constant in time. In the shutdown/fingering regime, the inner zone of the source region undergoes convective shutdown, in which the dissolution rate slows due to the recirculation of CO_2-rich fluid from the fingers back up to the source; the outer zone continues to exhibit fingering in a return flow of nearly fresh water from the porous layer outside the source region. In the shutdown/slumping and shutdown/Taylor slumping regimes, convective shutdown continues in the inner zone, while dissolution in the outer zone is constrained by the rate at which CO_2-rich fluid can migrate away from the source as a gravity current. This gravity current exhibits a sharp boundary with the over-riding counter current in the shutdown/slumping regime, and the dissolution flux in the outer zone decreases diffusively in time. However, in the shutdown/Taylor slumping regime, the boundary becomes highly diffuse and the dissolution flux in the outer zone decreases sub-diffusively in time. In the Taylor slumping regime, dissolution at the edge continues to be limited by the migration of a diffuse gravity current, but convective shutdown ceases in the inner zone due to nearly complete saturation of the layer. Finally, in the late diffusion regime, dissolution occurs via lateral diffusion though the porous layer with negligible convection.

All of the regimes can be organized into the phase diagram in figure 4-10. This diagram shows that the occurrence of the regimes depends on the Rayleigh number. For the highest Rayleigh numbers ($Ra \gtrsim 2000$), all regimes occur: dissolution begins in the early diffusion regime, then transitions through the fingering regime, the three regimes with convective shutdown, the Taylor slumping regime, and finally the late diffusion regime. For smaller Rayleigh numbers, fewer regimes occur as convection becomes increasingly less important relative to diffusion. For the smallest Rayleigh numbers ($Ra \lesssim 55$), none of the regimes with convective enhancement occur: dissolution begins in the early diffusion regime and
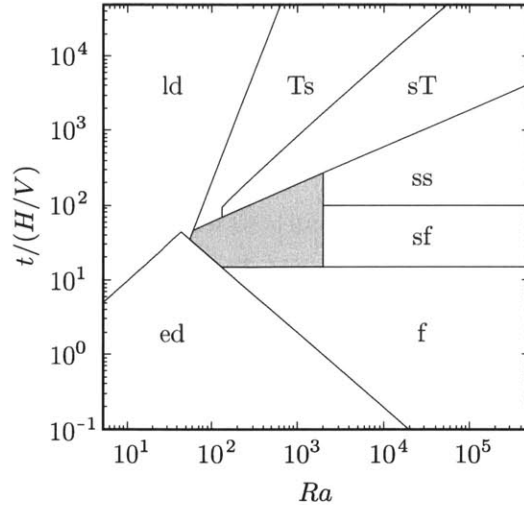
Figure 4-10: Phase diagram of the dissolution regimes. Tracing a vertical line through the diagram illustrates the regimes that occur for a particular Rayleigh number. The gray region in the center represents conditions for which we did not model dissolution. The sharp angle on the border between the Taylor slumping (Ts) and shutdown/Tayor slumping (sT) regimes occurs at $Ra = 133$, the leftmost extent of the fingering regime (f), due to uncertainty about the validity of the convective shutdown mechanism for lower Rayleigh numbers.

transitions directly to the late diffusion regime.

4.6 Application

Since all the models have been derived for an idealized system, their applicability to real geologic traps is uncertain. While our system is 2D, rectilinear, perfectly horizontal, and homogeneous, real geologic traps typically exhibit complex 3D geometries and heterogeneity at a variety of scales due to features such as lenses and layers of fine-grained rock. In addition, the length of the CO_2-brine interface in a real trap continually decreases as the CO_2 dissolves, whereas the interface length in our system is constant (figure 4-1). Due to the large number of differences and their complexity, we can not at this stage rigorously evaluate the accuracy of our models in real traps or determine whether they provide upper or lower bounds on the dissolution rates. Some features of real traps, such as slope and natural groundwater flow, will likely lead to higher dissolution rates in practice, but the effect of other features such as heterogeneity is more difficult to predict. Consequently, we emphasize that the main contribution of the study is, strictly speaking, the elucidation of how dissolution is affected by the finite CO_2-brine interface that exists during storage in geologic traps.

149

trap type	thickness H [m]	permeability k [mD]	Ra
thick, high perm.	200	1000	2×10^5
thin, high perm.	20	1000	2×10^4
thick, low perm.	200	10	2×10^3
thin, low perm.	20	10	2×10^2

Table 4.1: We apply the dissolution models to four types of simplified geologic traps.

While our models are based on several assumptions, applying them to real geologic traps can be useful. Since the models are all analytical, they can quickly provide rough estimates of the dissolution rates that can be expected in practice, and can help constrain the time required to completely dissolve a volume of injected CO_2. While highly uncertain, these estimates are useful because there are currently several sequestration projects worldwide either injecting or planning to inject CO_2 into structural and stratigraphic traps, but there are limited techniques available to quickly predict dissolution rates over the lifetime of the project. While large simulations incorporating site-specific geometry and geology play an important role in quantifying these rates, they are time-consuming to develop and the information they provide is also highly uncertain due to uncertainty in the subsurface properties. In addition, uncertainty arises from the inability of conventional simulations to resolve the small length scales associated with the fingering instability, which plays a key role in the dissolution process.

With their limitations in mind, we apply the models to a few simplified geologic traps. The traps are characterized by six dimensional parameters: the layer thickness, H; the width of the CO_2-brine interface, W; the length of the trap in the $\hat{y}$-direction, L (see figure 4-1); the CO_2 diffusivity, D; the saturated CO_2 concentration, c_s; and the buoyancy velocity, $V = \Delta\rho g k/\mu\phi$. We set the parameters to represent a range of conditions that may be encountered in the subsurface [150, 113]. While all of these parameters exhibit variability, for simplicity we set most of them to fixed values: $L = 40$ km, $D = 1 \times 10^{-9}$ m^2/s, $\Delta\rho = 10$ kg/m^3, $\mu = 6$ mPa s, $\phi = 0.15$, and $c_s = 50$ kg/m^3. For the layer thickness and permeability, two of the most highly variable parameters, we consider low and high values: for the layer thickness, we consider $H = 20$ m and $H = 200$ m, and for the permeability, we consider $k = 10$ mD and $k = 1000$ mD (1 mD $\approx 10^{-15}$ m^2). These permeabilities lead to two buoyancy velocities: 0.3 m/yr and 30 m/yr, respectively. Combining the buoyancy velocities and layer thicknesses yields the four simple traps shown in table 4.1. For each

trap, we consider two values for the width of the CO_2-brine interface: $W = 5$ km and $W = 15$ km.

While the traps are idealizations, they reflect properties from real sequestration projects. The thin, low-permeability trap displays similarities to the upper zones in the Nagaoka project ($H \approx 10$ m, $k \approx 10$ mD) [117], and the B-sandstone in the Tensleep Formation in the Teapot Dome ($H \approx 30$ m, $k \approx 30$ mD) [28]. The thin, high-permeability trap displays similarities to the Naylor Field in the CO2CRC Otway Project ($H \approx 25$ m, $k \approx 700$ mD) [156], and the thick, low-permeability trap exhibits properties similar to the Mt. Simon Sandstone in the Cincinnatti Arch ($H \approx 100$ m, $k \approx 10 - 200$ mD) [113]. The thick, high-permeability trap has properties similar to the Utsira Formation in the Sleipner Project ($H \approx 250$ m, $k \approx 5000$ mD), which is not a structural or stratigraphic trap, but is often used to contextualize results of CO_2 dissolution models [123, 68, 105].

For each idealized trap, we calculate the dissolution flux over ten million years. For most of the traps, the models completely specify the behavior. However, for the thin, low-permeability trap ($Ra = 200$), there is a period of time for which we did not develop models (see figure 4-10). For these times, we approximate the dissolution flux with a straight line in log space that connects the models we do have; this approximation is a power law in linear space.

The results show a few similarities between the traps, but several differences. The traps are similar in that they all exhibit monotonic decreases in the dissolution flux: the flux first decreases diffusively in the early diffusion regime, becomes constant during the fingering regime, declines sharply in the regimes with convective shutdown, and then decreases more slowly but still sub-diffusively during the Taylor slumping regime (figure 4-11a). However, the detailed trajectories of the fluxes are very different among the traps, with the durations of the different regimes and the magnitude of the fluxes during those regimes varying by orders of magnitude (figure 4-11b). For example, in the high-permeability traps, fingering occurs after about 20 days and the dissolution flux is about 30 $kton/km^2/yr$ (all tons are metric tons), but in the low-permeability traps fingering occurs after about 600 years and the flux is roughly 300 $ton/km^2/yr$. The time at which the regimes with convective shutdown and gravity currents occur is different for each trap: it ranges from 10 years in the thin, high-permeability trap to about 10,000 years in the thick, low-permeability trap. The magnitude of the fluxes during these regimes also vary widely among the traps.
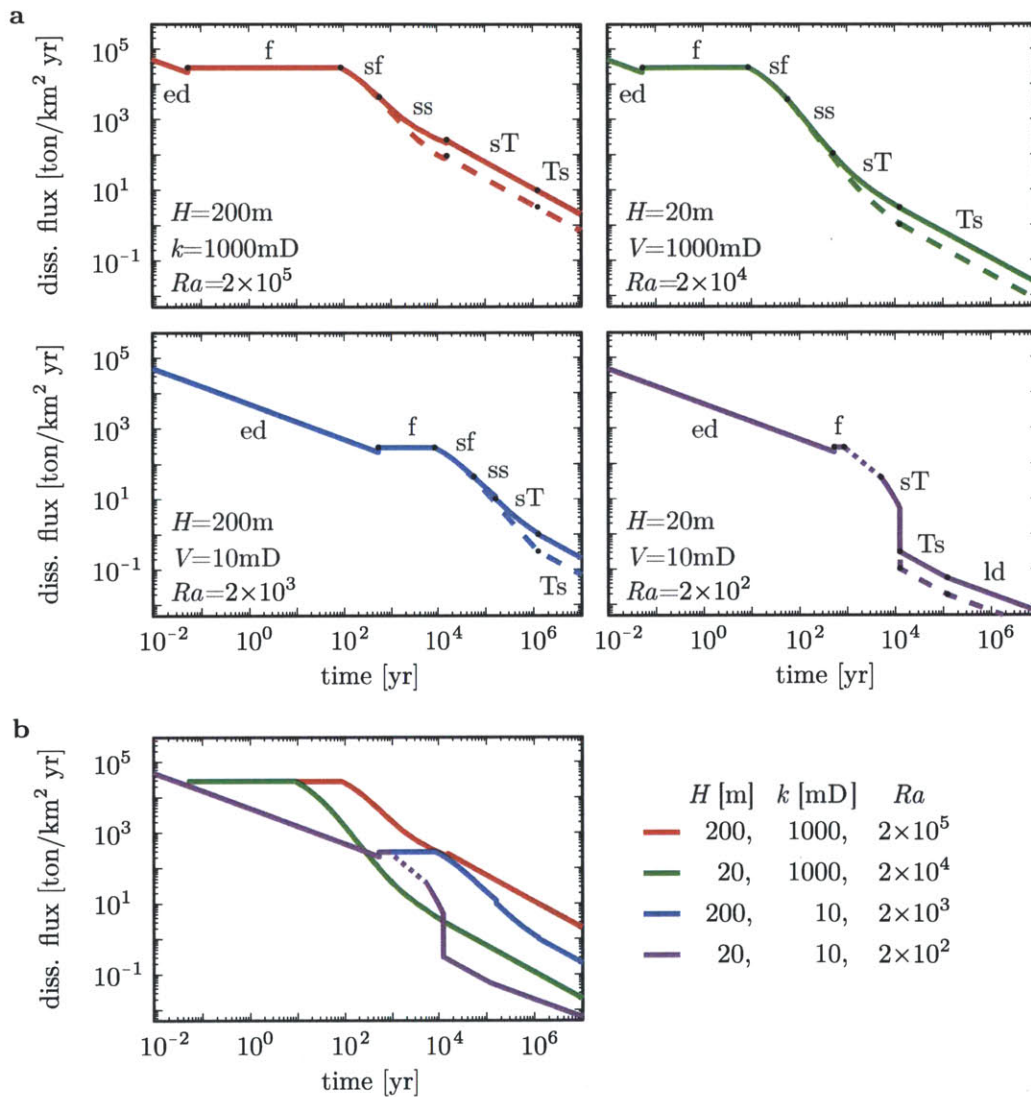
151

Figure 4-11: We calculate the evolution of the dissolution flux in four idealized geologic traps characterized in table 4.1. The short dashed line on the purple curve marks the time period we did not explicitly model, but that we approximate. The steep drop in the purple curve is due to the fact that the model for the Taylor slumping regime (Ts) represents a lower bound on the flux. **a.** The fluxes in each trap exhibit the same general trend: a monotonic decrease, with a period of constant flux during the fingering regime (f). In addition, the wide traps (dashed; $W = 15$ km) exhibit lower fluxes at late times compared to the narrow traps (solid; $W = 5$ km). However, the detailed trajectories for each trap exhibit several differences, such as orders of magnitude variation in the transition times between the regimes (black circles) and the magnitude of the flux during the regimes. **b.** These discrepancies are highlighted by comparing the trajectories on the same plot ($W = 5$ km).
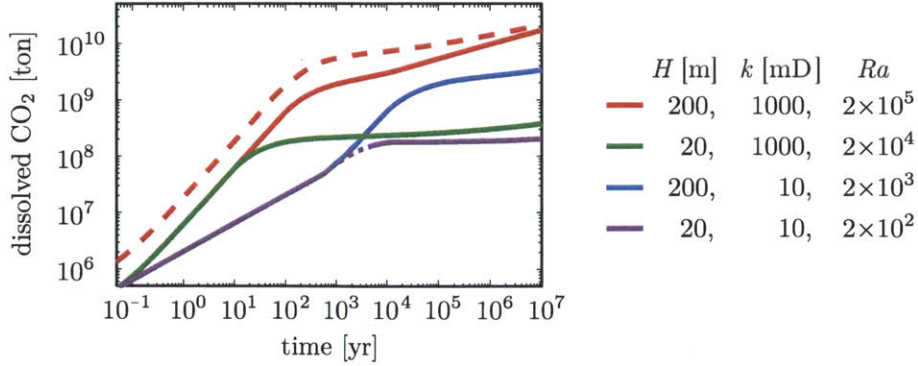
Figure 4-12: For each idealized trap, we integrate the dissolution flux to calculate the dissolved mass of CO_2 vs. time (solid: $W = 5$ km; dashed: $W = 15$ km). The high-permeability traps (red, green) dissolve more CO_2 at short times compared to the low-permeability traps (blue, purple). At late time, however, the quantity of dissolved CO_2 depends on the trap thickness: the thick traps (red, blue) ultimately dissolve more than the thin traps (green, purple). In all traps, large interface widths (large Ws) lead to more dissolved CO_2 for all times we consider (we only show one example for clarity). Comparison to figure 4-11 shows the opposite effect on the flux.

By integrating the dissolution fluxes, we calculate the cumulative mass of CO_2 dissolved over time in each trap (figure 4-12). In practice, this quantity is of course constrained by the storage capacity of the trap, but in our idealized model the storage capacity is undetermined because the trap geometry is not fully specified. We find that at early times, the high-permeability traps dissolve more CO_2 than the low-permeability traps due to both the shorter onset time for the fingering regime ($t_f \sim D/V^2$) and the larger magnitude of the flux during the regime ($\overline{f}_f = 0.017c_sV$). These traps dissolve hundreds of megatons of CO_2 over tens of years, whereas the low-permeability traps barely exceed 10 megatons. At late times, the dissolved mass of CO_2 depends on both the permeability and trap thickness, since the thickness impacts the end of fingering and the subsequent regimes. The thin traps nearly plateau at a little over 100 megatons of CO_2, while the thick traps reach over 1 billion tons—about half the annual emissions of coal- and gas-fired power plants in the US [158]. In all traps, the amount of dissolved CO_2 increases after the end of fingering, though this behavior is negligible in the thin, low-permeability trap and is most pronounced in the thick, high-permeability trap.

While the width of the CO_2-brine interface in our models is constant, the results illustrate that this parameter has a complex effect on dissolution. For the large interface width ($W = 15$ km), the mean dissolution flux is always lower at late times than for the small width ($W = 5$ km) (figure 4-11a). This is due to the fact that, for small W, the relatively

153

large dissolution rates in the outer zone have a stronger impact on the mean behavior. The results for the cumulative CO_2 dissolution, however, exhibit the opposite trend: in all of the traps, the larger interface width leads to the most dissolution for all times up to 10 million years (figure 4-12). This indicates that increased surface area over which dissolution occurs at early times is more important than the increased dissolution fluxes at the edge at late times. In an actual geologic trap in which the interface width continually decreases, both the early-time advantage of large surface areas and the late time advantage of relatively large edge-zones will likely exist.

4.7 Discussion and conclusion

We find that CO_2 dissolution in a geologic trap varies both spatially and temporally. In general, the CO_2 source region exhibits at least two zones of different behavior: an outer zone adjacent to the edge of the source, and an inner zone far away from the edge. In the inner zone, the dissolution mechanisms are nearly identical to those observed in closed systems. Dissolution first occurs via vertical diffusion without convective enhancement, then via fingering, and then via convective shutdown. In the outer zone, however, the mechanisms are strongly impacted by the porous layer outside the source region, which continues to supply relatively unsaturated water long after the inner zone becomes highly saturated. During the fingering and shutdown/fingering regimes, this influx of unsaturated water is approximately constant in time, and as a result, the dissolution flux near the edge is also constant. During the shutdown/slumping regime, the influx of water and dissolution flux decrease diffusively with time due to the migration of dense, CO_2-rich flow away from the source as a gravity current. During the shutdown/Taylor-slumping and Taylor slumping regimes, the influx of water and dissolution flux decrease sub-diffusively in time due to diffusive mixing between the dense gravity current and the low-concentration counter-current. At the latest times, convection becomes negligible relative to diffusion and the dissolution flux becomes limited by lateral diffusion though the porous layer.

Applying the regime models to several representative geologic traps informs the relative importance of the different regimes and provides rough estimates of how much CO_2 may be dissolved in practice. In general, we find that the onset times of the regimes and the magnitudes of the dissolution flux depends strongly on the reservoir properties. This

154

result indicates that there is no typical dissolution behavior and suggests that accurately quantifying dissolution requires a site-specific approach. In addition, it encourages the use of dissolution models in the site-selection process, since a well-chosen site could potentially dissolve hundreds of megatons of CO_2 within tens of years.

Bibliography

[1] Salinity of the Mt. Simon Sandstone in the Illinois Basin. Technical report, Midwest Geological Sequestration Consortium, 2005.

[2] Report of the Interagency Task Force on Carbon Capture and Storage. http://www.epa.gov/climatechange/policy/ccs_task_force.html, 2010.

[3] Mean daily average temperature map of the United States. http://cdo.ncdc.noaa.gov/cgi-bin/climaps/climaps.pl, 2010.

[4] P. L. Applin and E. R. Appin. Regional subsurface stratigraphy and structure of Florida and southern Georgia. *AAPG Bulletin*, 28(12):1673–1753, 1944.

[5] P. L. Applin and E. R. Applin. The Gulf Series in northern Florida and southern Georgia. Professional Paper 524-G, USGS, 1967.

[6] U. M. Ascher, S. J. Ruuth, and R. J. Spiteri. Implicit-explicit Runge-Kutta methods for time-dependent partial differential equations. *Appl. Numer. Math.*, 25:151–167, 1997.

[7] W. R. Aucott. Hydrology of the southeastern Coastal Plain aquifer system in South Carolina and parts of Georgia and North Carolina. Professional Paper 1410-E, USGS, 1996.

[8] S. Bachu. Screening and ranking of sedimentary basins for sequestration of CO_2 in geological media in response to climate change. *Environ. Geol.*, 44:277–289, 2003.

[9] S. Bachu and J. J. Adams. Sequestration of CO_2 in geological media in response to climate change: capacity of deep saline aquifers to sequester CO_2 in solution. *Energ. Convers. Manage.*, 44:3151 – 3175, 2003.

[10] S. Bachu, D. Bonijoly, J. Bradshaw, R. Burruss, S. Holloway, N. P. Christensen, and O. M. Mathiassen. CO_2 storage capacity estimation: Methodology and gaps. *Int. J. Greenh. Gas Con.*, 1:430–443, 2007.

[11] S. Backhaus, K. Turitsyn, and R. E. Ecke. Convective instability and mass transport of diffusion layers in a Hele-Shaw geometry. *Phys. Rev. Lett.*, 106:104501, 2011.

[12] G. I. Barenblatt. On some unsteady motions of fluids and gases in a porous medium. *Appl. Math. and Mech. (PMM)*, 16:67–78, 1952.

[13] G. I. Barenblatt. *Scaling, Self-Similarity, and Intermediate Asymptotics*. Cambridge University Press, 1996.

[14] R. A. Barker and M. Pernik. Regional hydrology and simulation of deep ground-water flow in the Southeastern Coastal Plain aquifer system in Mississippi, Alabama, Georgia, and South Carolina. Professional Paper 1410-C, USGS, 1994.

[15] D. A. Barnes, D. H. Bacon, and S. R. Kelley. Geological sequestration of carbon dioxide in the Cambrian Mount Simon Sandstone: regional storage capacity, site characterization, and large-scale injection feasibility, Michigan Basin. *Environ. Geosci.*, 16 (3):163–183, 2009.

[16] M. Batzle and Z. Wang. Seismic properties of pore fluids. *Geophysics*, 57:1396–1408, 1992.

[17] J. Bear. *Dynamics of Fluids in Porous Media.* Elsevier, New York, reprinted with corrections, Dover, New York, 1988, 1972.

[18] D. B. Bennion and S. Bachu. Drainage and imbibition relative permeability relationships for supercritical CO_2/brine and H_2S/brine systems in intergranular sandstone, carbonate, shale, and anhydrite rocks. *Soc. Pet. Eng. J.*, 11(3):487–496, 2008.

[19] S. M. Benson and D. R. Cole. CO_2 sequestration in deep sedimentary formations. *Elements*, 4(5):325–331, 2008.

[20] P. D. Bergman and E. M. Winter. Disposal of carbon dioxide in aquifers in the US. *Energ. Convers. Manage.*, 36(6–9):523–526, 1995.

[21] M. Bickle, A. Chadwick, H. E. Huppert, M. Hallworth, and S. Lyle. Modeling carbon dioxide accumulation at Sleipner: Implications for underground carbon storage. *Earth Planet. Sci. Lett.*, 255(1–2):164–176, 2007.

[22] J. T. Birkholzer, Q. Zhou, and C.-F. Tsang. Large-scale impact of CO_2 storage in deep saline aquifers: a sensitivity study on pressure response in stratified systems. *Int. J. Greenh. Gas Con.*, 3:181–194, 2009.

[23] K. Bjørlykke. Fluid flow in sedimentary basins. *Sediment. Geol.*, 86:137–158, 1993.

[24] J. Bradshaw, S. Bachu, D. Bonijoly, R. Burruss, S. Holloway, N. P. Christensen, and O. M. Mathiassen. CO_2 storage capacity estimation: issues and development of standards. *Int. J. Greenh. Gas Con.*, 1:62–68, 2007.

[25] Carbon Capture and Sequestration Technologies at MIT. CO_2 thermophysical property calculator. http://sequestration.mit.edu/tools/index.html.

[26] H. D. Cheng. *Multilayered Aquifer Systems: Fundamentals and Applications.* Marcel Dekker, 2000.

[27] P. Cheng and I. Chang. Buoyancy induced flows in a saturated porous medium adjacent to impermeable horizontal surfaces. *Int. J. Heat Mass Trans.*, 19:1267–1272, 1976.

[28] L. Chiaramonte, M. D. Zoback, J. Friedmann, and V. Stamp. Seal integrity and feasibility of CO_2 sequestration in the Teapot Dome EOR pilot: geomechanical site characterization. *Environ. Geol.*, 54(8):1667–1675, 2008.

[29] National Research Council. Induced seismicity potential in energy technologies. Technical report, 2012.

[30] L. C. Craig et al. Stratigraphy of the Morrison and related formations, Colorado Plateau Region. Bulletin 1009-E, USGS, 1955.

[31] J. Crank. *The Mathematics of Diffusion*. Oxford University Press, 1980.

[32] J. Croisé, L. Schlickenrieder, P. Marschall, J. Y. Boisson, P. Vogel, and S. Yamamoto. Hydrogeological investigations in a low permeability claystone formation: the Mont Terri Rock Laboratory. *Phys. Chem. Earth*, 29:3–15, 2004.

[33] W. L. Dam, J. M. Kernodle, G. W. Levings, and S. D. Craigg. Hydrogeology of the Morrison Formation in the San Juan structural basin, New Mexico, Colorado, Arizona, and Utah. Hydrologic Investigations Atlas HA-720-J, USGS, 1990.

[34] G. De Josselin De Jong. The simultaneous flow of fresh and salt water in aquifers of large horizontal extension determined by shear flow and vortex theory. *Proc. Euromech.*, 143:75–82, 1981.

[35] R. de Loubens and T. S. Ramakrishnan. Analysis and computation of gravity-induced migration in porous media. *J. Fluid Mech.*, 675:60–86, 2011.

[36] M. Dentz, D. M. Tartakovsky, E. Abarca, A. Guadagnini, X. Sanchez-vila, and J. Carrera. Variable-density flow in porous media. *J. Fluid Mech.*, 561:209–235, 2006.

[37] D. N. Dewhurst, Y. Yang, and A. C. Aplin. Permeability and fluid flow in natural mudstones. In A. C. Aplin, A. J. Fleet, and J. H. S. Macquaker, editors, *Muds and Mudstones: Physical and Fluid-flow Properties*, volume 158, pages 23–43. Geological Society of London, 1999.

[38] J. J. Dooley. Valuing national and basin level geologic CO_2 storage capacity assessments in a broader context. *Int. J. Greenh. Gas Con.*, 5:177–178, 2011.

[39] J. J. Dooley, R. T. Dahowski, C. L. Davidson, S. Bachu, N. Gupta, and J. Gale. A CO_2 storage supply curve for North America and its implications for the deployment of carbon dioxide capture and storage systems. *Proc. 7th Intl. Conf. Greenh. Gas Control Technol. Vol. 1, Peer-reviewed papers and plenary presentations*, 2004.

[40] J. S. Downey. Geohydrology of the Madison and associated aquifers in parts of Montana, North Dakota, South Dakota, and Wyoming. Professional Paper 1273-G, USGS, 1984.

[41] J. S. Downey and G. A. Dinwiddie. The regional aquifer system underlying the Northern Great Plains in parts of Montana, North Dakota, South Dakota, and Wyoming–summary. Professional Paper 1402-A, USGS, 1988.

[42] Z. Duan and R. Sun. An improved model calculating CO_2 solubility in pure water and aqueous NaCl solutions from 273 to 533 K and from 0 to 2000 bar. *Chem. Geol.*, 193:257–271, 2003.

[43] E. B. Dussan V. and F. M. Auzerais. Buoyancy-induced flow in porous media generated near a drilled oil well. Part 1. The accumulation of filtrate at a horizontal impermeable boundary. *J. Fluid Mech.*, 254:283–311, 1993.

159

[44] C. Ehlig-Economides and M. J. Economides. Sequestering carbon dioxide in a closed underground volume. *J. Pet. Sci. Eng.*, 70:118–125, 2010.

[45] J. W. Elder. Transient convection in a porous medium. *J. Fluid Mech.*, 27(3):609–623, 1967.

[46] R. M. Enick and S. M. Scott. CO_2 solubility in water and brine under reservoir conditions. *Chem. Eng. Commun.*, 90(1):23–33, 1990.

[47] J. Ennis-King and L. Paterson. Role of convective mixing in the long-term storage of carbon dioxide in deep saline formations. *Soc. Pet. Eng. J.*, 10(3):349–356, 2005.

[48] J. Ennis-King, I. Preston, and L. Paterson. Onset of convection in anisotropic porous media subject to a rapid change in boundary conditions. *Phys. Fluids*, 17:084107, 2005.

[49] M. E. Erdogan and P. C. Chatwin. The effects of curvature and buoyancy on the laminar dispersion of solute in a horizontal tube. *J. Fluid Mech.*, 29(3):465–484, 1967.

[50] S. Escoffier, F. Homand, A. Giraud, N. Hoteit, and K. Su. Under stress permeability determination of the Meuse/Haute-Marne mudstone. *Eng. Geol.*, 81:329–340, 2005.

[51] P. Falkowski, R. J. Scholes, E. Boyle, J. Canadell, D. Canfield, J. Elser, N. Gruber, K. Hibbard, P. Hogberg, S. Linder, F. T. Mackenzie, III Moore, B., T. Pedersen, Y. Rosenthal, S. Seitzinger, V. Smetacek, and W. Steffen. The global carbon cycle: A test of our knowledge of Earth as a system. *Science*, 290(5490):291–296, 2000.

[52] R. Q. Foote, L. M. Massingill, and R. H. Wells. Petroleum geology and the distribution of conventional crude oil, natural gas, and natural gas liquids, East Texas Basin. Open-File Report 88-450-K, USGS, 1988.

[53] G. W. Freethey and G. E. Cordy. Geohydrology of Mesozoic rocks in the Upper Colorado River Basin in Arizona, Colorado, New Mexico, Utah, and Wyoming, excluding the San Juan Basin. Professional Paper 1411-C, USGS, 1991.

[54] G. W. Freethey, B. A. Kimball, D. E. Wilberg, and J. W. Hood. General hydrogeology of the aquifers of Mesozoic age, Upper Colorado River Basin – excluding the San Juan Basin – Colorado, Utah, Wyoming, and Arizona. Hydrologic Atlas 698, USGS, 1988.

[55] R. A. Freeze and J. A. Cherry. *Groundwater*. Prentice Hall, 1979.

[56] S. E. Frezon, T. M. Finn, and J. H. Lister. Total thickness of sedimentary rocks in the conterminous United States, 1983.

[57] S. E. Frezon, T. M. Finn, and K. L. Varnes. Map of sedimentary basins in the conterminous United States. http://pubs.er.usgs.gov/usgspubs/om/om223, 1988.

[58] S. J. Friedmann, J. J. Dooley, H. Held, and O. Edenhofer. The low cost of geological assessment for underground CO_2 storage: Policy and economic implications. *Energy Conv. Manag.*, 47(13–14):1894–1901, 2006.

[59] W. E. Galloway, D. K. Hobday, and K. Magara. Frio Formation of Texas Gulf Coastal Plain: depositional systems, structural framework, and hydrocarbon distribution. *AAPG Bulletin*, 66(6):649–648, 1982.

[60] J. E. Garcia. Density of aqueous solutions of CO_2. Technical Report 49023, Lawrence Berkeley National Laboratory, 2001.

[61] J. R. Grasso. Mechanics of seismic instabilities induced by the recovery of hydrocarbons. *Pure Appl. Geophys.*, 139(3/4):507–534, 1992.

[62] W. D. Gunter, S. Bachu, and S. Benson. The role of hydrogeological and geochemical trapping in sedimentary basins for secure geological storage of carbon dioxide. In S. J. Baines and R. H. Worden, editors, *Geological Storage of Carbon Dioxide*, volume 233 of *Geological Society, London, Special Publications*, pages 129–145. 2004.

[63] N. Gupta. *Geologic and fluid-density controls on the hydrodynamics of the Mt. Simon Sandstone and overlying geologic units in Ohio and surrounding states*. PhD thesis, The Ohio State University, 1993.

[64] H. Hassanzadeh, M. Pooladi-Darvish, and D. W. Keith. Scaling behavior of convective mixing, with application to geological storage of CO_2. *A.I.Ch.E.*, 53(5):1121–1131, 2007.

[65] H. R. Henry. Effects of dispersion on salt encroachment in coastal aquifers. Technical Report 1613-C, USGS, 1964.

[66] M. A. Hesse, H. A. Tchelepi, B. J. Cantwell, and F. M. Orr. Gravity currents in horizontal porous layers: transition from early to late self-similarity. *J. Fluid Mech.*, 577:363–383, 2007.

[67] M. A. Hesse, F. M. Orr, Jr., and H. A. Tchelepi. Gravity currents with residual trapping. *J. Fluid Mech.*, 611:35–60, 2008.

[68] D. R. Hewitt, J. A. Neufeld, and J. R. Lister. Convective shutdown in a porous medium at high Rayleigh number. *J. Fluid Mech.*, 719, 2013.

[69] J. J. Hidalgo, J. Fe, L. Cueto-Felgueroso, and R. Juanes. Scaling of convective mixing in porous media. *Phys. Rev. Lett.*, 109:264503, 2012.

[70] M. Hoffert, K. Caldeira, G. Benford, D. Criswell, C. Green, H. Herzog, A. Jain, H. Kheshgi, K. Lackner, J. Lewis, H. Douglas Lightfoot, W. Manheimer, J. Mankins, M. Mauel, L. J. Perkins, M. E. Schlesinger, T. Volk, and T. M. L. Wigley. Advanced technology paths to global climate stability: energy for a greenhouse planet. *Science*, 298:981–987, 2002.

[71] J. D. Hoholick, T. Metarko, and P. E. Potter. Regional variations of porosity and cement: St. Peter and Mt. Simon sandstones in Illinois Basin. *AAPG Bulletin*, 68(6): 753–764, 1984.

[72] S. D. Hovorka. Optimal geological environments for carbon dioxide disposal in saline aquifers in the United States. Contract Report DE-AC26-98FT40417, Bureau of Economic Geology, The University of Texas at Austin, 1999.

[73] S. D. Hovorka, C. Doughty, P. R. Knox, C. T. Green, K. Pruess, and S. M. Benson. Evaluation of brine-bearing sands of the Frio Formation, Upper Texas Gulf Coast for geologic sequestration of CO_2. In *Proceedings, First National Conference on Carbon Sequestration, May 14-17, Washington, DC*, 2001.

[74] S. D. Hovorka, M. L. Romero, A. G. Warne, W. A. Ambrose, T. A. Tremblay, R. H. Trevino, and D. Sasson. Brine-formation database. http://www.beg.utexas.edu/environqlty/co2seq/dispslsalnt01.htm, November 2003.

[75] S. D. Hovorka, M. L. Romero, A. G. Warne, W. A. Ambrose, T. A. Tremblay, R. H. Trevino, and D. Sasson. Brine-formation database. http://www.beg.utexas.edu/environqlty/co2seq/, November 2003.

[76] S. D. Hovorka, M. L. Romero, A. G. Warne, W. A. Ambrose, T. A. Tremblay, R. H. Trevino, and D. Sasson. Sequestration of greenhouse gases in brine formations. http://www.beg.utexas.edu/environqlty/co2seq/dispslsalnt01.htm, 2003.

[77] H. E. Huppert and A. W. Woods. Gravity-driven flows in porous layers. *J. Fluid Mech.*, 292:55–69, 1995.

[78] International Energy Agency. CO_2 emissions from fuel combustion – highlights. http://www.iea.org/co2highlights/, 2011.

[79] International Energy Agency. Electricity generation by fuel in the United States (1972–2008). http://www.iea.org/stats, 2011.

[80] IPCC. *Special Report on Carbon Dioxide Capture and Storage, B. Metz et al. (eds.)*. Cambridge University Press, 2005.

[81] R. Juanes, E. J. Spiteri, F. M. Orr, Jr., and M. J. Blunt. Impact of relative permeability hysteresis on geological CO_2 storage. *Water Resour. Res.*, 42:W12418, 2006.

[82] R. Juanes, C. W. MacMinn, and M. L. Szulczewski. The footprint of the CO_2 plume during carbon dioxide storage in saline aquifers: storage efficiency for capillary trapping at the basin scale. *Transp. Porous Media*, 82:19–30, 2010.

[83] R. Juanes, B. H. Hager, and H. J. Herzog. No geologic evidence that seismicity causes fault leakage that would render large-scale carbon capture and storage unsuccessful. *Proc. Natl. Acad. Sci. USA*, 109(52):E3623, 2012.

[84] J. M. Kernodle. Hydrogeology and steady-state simulation of ground-water flow in the San Juan Basin New Mexico, Colorado, Arizona, and Utah. Water-Resources Investigation Report 95-4187, USGS, 1996.

[85] Y. K. Kharaka and J. S. Hanor. Deep fluids in the continents: I. Sedimentary basins. In J. I. Drever, editor, *Treatise on Geochemistry*, volume 5. Elsevier, 2007.

[86] P. B. King and H. M. Beikman. Geologic map of the United States. US Geological Survey, 1974.

[87] T. J. Kneafsey and K. Pruess. Laboratory flow experiments for visualizing carbon dioxide-induced, density-driven brine convection. *Transp. Porous Med.*, 82:123–139, 2010.

[88] D. R. Kolata. *Interior Cratonic Basins*, chapter 2, pages 59–73. A.A.P.G, 1990.

[89] L. F. Konikow and C. E. Neuzil. A method to estimate groundwater depletion from confining layers. *Water Resour. Res.*, 43:W07417, 2007.

[90] C. W. Kreitler, M. S. Akhter, and A. C. Donnelly. Hydrologic hydrochemical characterization of Texas Frio Formation used for deep-well injection of chemical wastes. *Environ. Geol. Water Sci.*, 16(2):107–120, 1990.

[91] A. Kron and G. Heiken. Geothermal gradient map of the United States. Technical report, Los Alamos National Lab, 1980.

[92] K. S. Lackner. A guide to CO_2 sequestration. *Science*, 300(5626):1677–1678, 2003.

[93] L. Lake. *Enhanced Oil Recovery*. Prentice Hall, 1989.

[94] J. D. Lambert. *Numerical Methods for Ordinary Differential Systems: The Initial Value Problem*. Wiley, 1991.

[95] D. C. Lampe. Hydrogeologic framework of bedrock units and initial salinity distribution for a simulation of groundwater glow for the Lake Michigan Basin. Scientific Investigations Report 2009-5060, USGS, 2009.

[96] A. J. Landman and R. J. Schotting. Heat and brine transport in porous media: the Oberbeck-Boussinesq approximation revisited. *Transp. Porous Med.*, 70:355–373, 2007.

[97] R. W. Lee. Water–quality maps for selected Upper Cretaceous water–bearing zones in the southeastern coastal plain. Water-Resources Investigations Report 85-4193, USGS, 1985.

[98] R. W. Lee. Geochemistry of ground water in the Southeastern Coastal Plain Aquifer System in Mississippi, Alabama, Georgia, and South Carolina. Professional Paper 1410–D, USGS, 1994.

[99] H. E. Leetaru and J. H. McBride. Reservoir uncertainty, Precambrian topography, and carbon sequestration in the Mt. Simon Sandstone, Illinois Basin. *Environ. Geosci.*, 16(4):235–243, 2009.

[100] R. J. LeVeque. *Numerical Methods for Conservation Laws*. Birkhäuser Verlag, Berlin, second edition, 1992.

[101] R. J. LeVeque. *Finite Volume Methods for Hyperbolic Problems*. Cambridge University Press, 2002.

[102] O. B. Lloyd, Jr. and W. L. Lyke. The ground water atlas of the United States: Illinois, Indiana, Kentucky, Ohio, Tennessee. URL: http://capp.water.usgs.gov/gwa/ch_k/index.html, 1995. Accessed 05-20-2008.

[103] R. G. Loucks, M. M. Dodge, and W. E. Galloway. Regional controls on diagenesis and reservoir quality in lower Tertiary sandstones along the lower Texas Gulf Coast. In D. A. McDonald and R. C. Surdam, editors, *Clastic diagenesis*. AAPG, 1984.

[104] S. Lyle, H. E. Huppert, M. Hallworth, M. Bickle, and A. Chadwick. Axisymmetric gravity currents in a porous medium. *J. Fluid Mech.*, 543:293–302, 2005.

[105] C. W. MacMinn and R. Juanes. Buoyant currents arrested by convective dissolution. *Geophys. Rev. Lett.*, 40, 2013. doi:10.1002/grl.50473.

[106] C. W. MacMinn, M. L. Szulczewski, and R. Juanes. CO_2 migration in saline aquifers. Part 1: Capillary trapping under slope and groundwater flow. *J. Fluid Mech.*, 662: 329–351, 2010.

[107] C. W. MacMinn, M. L. Szulczewski, and R. Juanes. CO_2 migration in saline aquifers. Part 2. Capillary and solubility trapping. *J. Fluid. Mech.*, 688:321–351, 2011.

[108] R. J. Mandle and A. L. Kontis. Simulation of regional ground-water flow in the Cambrian-Ordovician aquifer system in the northern Midwest, United States. Professional Paper 1405-C, USGS, 1992.

[109] S. A. Mathias, P. E. Hardisty, M. R. Trudell, and R. W. Zimmerman. Screening and selection of sites for CO_2 sequestration based on pressure buildup. *Int. J. Greenh. Gas Con.*, 3:577–585, 2009.

[110] B. J. O. L. McPherson and B. S. Cole. Multiphase CO_2 flow, transport and sequestration in the Powder River Basin, Wyoming, USA. *J. Geochem. Explor.*, 69–70:65–69, 2000.

[111] W. F. Meents, A. H. Bell, O. W. Rees, and W. G. Tilbury. Illinois oilfield brines: their geologic occurrence and chemical composition. Illinois Petroleum 66, Illinois State Geological Survey, 1952.

[112] E. A. Merewether. Stratigraphy and tectonic implications of Upper Cretaceous rocks in the Powder River Basin, northeastern Wyoming and southeastern Montana. Bulletin 1917-T, USGS, 1996.

[113] K. Michael, A. Golab, V. Shulakova, J. Ennis-King, G. Allinson, S. Sharma, and T. Aiken. Geological storage of CO_2 in saline aquifers—a review of the experience from existing storage operations. *Int. J. Greenh. Gas Con.*, 4:659–667, 2010.

[114] J. A. Miller. The ground water atlas of the United States: Alabama, Florida, Georgia, South Carolina. URL: http://capp.water.usgs.gov/gwa/ch_g/index.html, 1998. Accessed 05-20-2008.

[115] S. Mishra, J. F. Pickens, and J. Delay. New approaches for transient testing and long-term pressure monitoring of low-permeability caprocks. In *Proceedings of the International Symposium on Site Characterization for CO_2 Geological Storage*, 2006.

[116] MIT. *The Future of Coal – An Interdisciplinary MIT Study.* MIT Press, 2007.

[117] S. Mito, Z. Xue, and T. Sato. Effect of formation water composition on predicting CO_2 behavior: a case study at the Nagaoka post-injection monitoring site. *Appl. Geochem.*, 30:33–40, 2013.

[118] R. A. Morton and L. S. Land. Regional variations in formation water chemistry, Frio Formation (Oligocene), Texas Gulf Coast. *AAPG Bulletin*, 71(2):191–206, 1987.

[119] M. Nathenson and M. Guffanti. Geothermal gradients in the conterminous United States. *J. Geophys. Res.*, 93:6437–6450, 1988.

[120] National Energy Technology Laboratory. Carbon sequestration atlas of the United States and Canada—Third edition, 2010. http://www.netl.doe.gov/technologies/carbon_seq/refshelf/atlas/.

[121] National Imagery and Mapping Agency. Digital terrain elevation data (DTED Level 0). http//:www.geocomm.com.

[122] S. Neglia. Migration of fluids in sedimentary basins. *AAPG Bulletin*, 63(4):573–597, 1979.

[123] J. A. Neufeld, M. A. Hesse, A. Riaz, M. A. Hallworth, H. A. Tchelepi, and H. E. Huppert. Convective dissolution of carbon dioxide in saline aquifers. *Geophys. Rev. Lett.*, 37:L22404, 2010.

[124] C. E. Neuzil. How permeable are clays and shales? *Water Resour. Res.*, 30(2): 145–150, 1994.

[125] N. Nguyen. *Micromixers: Fundamentals, Design and Fabrication.* Elsevier, 2011.

[126] J.-P. Nicot. Evaluation of large-scale CO_2 storage on fresh-water sections of aquifers: An example from the Texas Gulf Coast Basin. *Int. J. Greenh. Gas Con.*, 2(4):582–593, 2008.

[127] D. A. Nield and A. Bejan. *Convection in Porous Media.* Springer, 4 edition, 2013.

[128] J. M. Nordbotten and M. A. Celia. Similarity solutions for fluid injection into confined aquifers. *J. Fluid Mech.*, 561:307–327, 2006.

[129] J. M. Nordbotten, D. Kavetski, M. A. Celia, and S. Bachu. Model for CO_2 leakage including multiple geological layers and multiple leaky wells. *Environ. Sci. Technol.*, 43(3):743–749, 2009.

[130] M. J. Oak, L. E. Baker, and D. C. Thomas. Three-phase relative permeability of Berea sandstone. *J. Pet. Technol.*, 42(8):1054–1061, August 1990.

[131] F. M. Orr, Jr. Onshore geologic storage of CO_2. *Science*, 325:1656–1658, 2009.

[132] P. Ortoleva, editor. *Basin Compartments and Seals.* AAPG Memoir 61. AAPG, 1994.

[133] S. Pacala and R. Socolow. Stability wedges: Solving the climate problem for the next 50 years with current technologies. *Science*, 305:968–972, 2004.

[134] A. Paster and G. Dagan. Mixing at the interface between two fluids in porous media: a boundary-layer solution. *J. Fluid Mech.*, 584:455–472, 2007.

[135] G. S. H. Pau, J. B. Bell, K. Pruess, A. S. Almgren, M. J. Lijewskia, and K. Zhang. High-resolution simulation and characterization of density-driven flow in CO_2 storage in saline aquifers. *Adv. Water Resour.*, 33(4):443–455, 2010.

[136] S. Rapaka, S. Chen, R. Pawar, P. Stauffer, and D. Zhang. Non-modal growth of perturbations in density-driven convection in porous media. *J. Fluid Mech.*, 609: 285–303, 2008.

[137] R. A. Renken. Hydrology of the southeastern Coastal Plain aquifer system in Mississippi, Alabama, Georgia, and South Carolina. Professional Paper 1410-B, USGS, 1996.

[138] A. Riaz, M. Hesse, H. A. Tchelepi, and F. M. Orr, Jr. Onset of convection in a gravitationally unstable, diffusive boundary layer in porous media. *J. Fluid Mech.*, 548:87–111, 2006.

[139] J. Rutqvist and C. Tsang. A study of caprock hydromechanical changes associated with CO_2-injection into a brine formation. *Environ. Geol.*, 42:296–305, 2002.

[140] P. D. Ryder and A. F. Ardis. Hydrology of the Texas Gulf Coast aquifer systems. Open-File Report 91-64, USGS, 1991.

[141] L. Y. Sadler, M. B. Rahnama, and G. P. Whittle. Laboratory measurement of the permeability of Selma Chalk using an improved experimental technique. *Hazard. Waste Hazard. Mater.*, 9(4):331–343, 1992.

[142] D. P. Schrag. Preparing to capture carbon. *Science*, 315:812–813, 2007.

[143] A. C. Slim and T. S. Ramakrishnana. Onset and cessation of time-dependent, dissolution-driven convection in porous media. *Phys. Fluids*, 22:124103, 2010.

[144] A. C. Slim, M. M. Bandi, Joel C. Miller, and L. Mahadevan. Dissolution-driven convection in a Hele-Shaw cell. *Phys. Fluids*, 25:024101, 2013.

[145] R. Smith. Longitudinal dispersion of a buoyant contaminant in a shallow channel. *J. Fluid Mech.*, 78(4):677–688, 1976.

[146] E. W. Strom and M. J. Mallory. Hydrogeology and simulation of ground-water flow in the Eutaw-McShan Aquifer and in the Tuscaloosa Aquifer system in northeastern Mississippi. Water-Resources Investigation Report 94-4223, USGS, 1995.

[147] M. L. Szulczewski. Storage capacity and injection rate estimates for CO_2 sequestration in deep saline aquifers in the conterminous United States. Master's thesis, Massachusetts Institute of Technology, 2009.

[148] M. L. Szulczewski and R. Juanes. The evolution of miscible gravity currents in horizontal porous layers. *J. Fluid Mech.*, 719:82–96, 2013.

[149] M. L. Szulczewski, C. W. MacMinn, and R. Juanes. How pressure buildup and CO_2 migration can both constrain storage capacity in deep saline aquifers. In *10th Intl. Conf. Greenhouse Gas Control Technol., GHGT-10*, Amsterdam, The Netherlands, September 19–23, 2010.

[150] M. L. Szulczewski, C. W. MacMinn, H. J. Herzog, and R. Juanes. Lifetime of carbon capture and storage as a climate-change mitigation technology. *Proc. Natl. Acad. Sci. USA*, 109(14):5185–5189, 2012.

[151] D.M. Tartakovsky, A. Guadagnini, X. Sanchez-Vila, M. Dentz, and J. Carrera. A perturbation solution to the transient Henry problem for sea water intrusion. In *Developments in Water Science*, volume 55, pages 1573–1581, 2004.

[152] G. I. Taylor. Dispersion of soluble matter in solvent flowing slowly through a tube. *Proc. R. Soc. Lond. A*, 219(1137):186–203, 1953.

[153] T. Tokunaga, S. Hosoya, H. Tosaka, and K. Kojima. An estimation of the intrinsic permeability of argillaceous rocks and the effects of long-term fluid migration. In S. J. Düppenbecker and J. E. Iliffe, editors, *Basin Modelling: Practice and Progress*, volume 141, pages 83–94. Geological Society of London, 1998.

[154] H. Trapp, Jr. Hydrogeologic framework of the Northern Atlantic Coastal Plain in parts of North Carolina, Virginia, Maryland, Delaware, New Jersey, and New York. Professional Paper 1404-G, USGS, 1992.

[155] H. Trapp, Jr. and M. A. Horn. The ground water atlas of the United States: Delaware, Maryland, New Jersey, North Carolina, Pennsylvania, Virginia, West Virginia. URL: http://capp.water.usgs.gov/gwa/ch_l/index.html, 1997. Accessed 05-20-2008.

[156] J. Underschultz, C. Boreham, T. Dance, L. Stalker, B. Freifeld, D. Kirste, and J. Ennis-King. CO_2 storage in a depleted gas field: an overview of the CO2CRC Otway Project and initial results. *Int. J. Greenh. Gas Con.*, 5:922–932, 2011.

[157] US Energy Information Administration. Annual energy outlook 2010. Technical Report DOE/EIA-0383, 2010.

[158] US Energy Information Administration, US Department of Energy. Emissions of greenhouse gases in the United States 2008. Report No. DOE/EIA-0573(2008), http://www.eia.gov/oiaf/1605/ggrpt/pdf/0573(2008).pdf, 2009.

[159] D. Vella and H. E. Huppert. Gravity currents in a porous medium at an inclined plane. *J. Fluid Mech.*, 555:353–362, 2006.

[160] H. F. Wang. *Theory of Linear Poroelasticity*. Princeton University Press, 2000.

[161] R. L. Whitehead. The ground water atlas of the United States: Montana, North Dakota, South Dakota, Wyoming. URL: http://capp.water.usgs.gov/gwa/ch_i/index.html, 1996. Accessed 05-20-2008.

[162] L.H. Wickstrom, E. R. Venteris, J. A. Harper, J. McDonald, E. R. Slucher, K. M. Carter, S. F. Greb, J. G. Wells, W. B. Harrison III B. C. Nuttall, R. A. Riley, J. A. Drahovzal, J. A. Rupp, K. L. Avary, S. Lanham, D. A. Barnes, N. Gupta, M. A. Baranoski, P. Radhakkrishnan, M. P. Solis, G. R. Baum, D. Powers, M. E. Hohn, M. P. Parris, K. McCoy, G. M. Grammer, S. Pool, C. Luckhardt, and P Kish. Characterization of geologic sequestration opportunities in the MRCSP Region: final report under DOE cooperative aggrement DE-PS26-05NT42255, 2005.

[163] T. M. L. Wigley, R. Richels, and J. A. Edmonds. Economic and environmental choices in the stabilization of atmospheric CO_2 concentrations. *Nature*, 379(6562):240–243, 1996.

[164] H. B. Willman, E. Atherton, T. C. Buschbach, C. Collinson, J. C. Frye, M. E. Hopkins, J. A. Lineback, and J. A. Simon. *Handbook of Illinois stratigraphy*. Number Bulletin 95. Illinois State Geological Survey, 1975.

[165] R. A. Wooding, S. W. Tyler, and I. White. Convection in groundwater below an evaporating salt lake. 1. Onset of instability. *Water Resour. Res.*, 33(6):1199–1217, 1997.

[166] R. A. Wooding, S. W. Tyler, and I. White. Convection in groundwater below an evaporating salt lake. 2. Evolution of fingers or plumes. *Water Resour. Res.*, 33(6): 1219–1228, 1997.

[167] X. Xu, S. Chen, and D. Zhang. Convective stability analysis of the long-term storage of carbon dioxide in deep saline aquifers. *Adv. Water Resour.*, 29:397–407, 2006.

[168] Y. C. Yortsos. A theoretical analysis of vertical flow equilibrium. *Transp. Porous Med.*, 18(2):107–129, 1995.

[169] H. L. Young and D. I. Siegel. Hydrogeology of the Cambrian-Ordovician aquifer system in the northern Midwest, United States, with a section on ground-water quality. Professional Paper 1405-B, USGS, 1992.

[170] Q. Zhou, J. T. Birkholzer, C.-F. Tsang, and J. Rutqvist. A method for quick assessment of CO_2 storage capacity in closed and semi-closed saline formations. *Int. J. Greenh. Gas Con.*, 2:626–639, 2008.

[171] M. D. Zoback. *Reservoir Geomechanics*. Cambridge University Press, 2007.

[172] M. D. Zoback and S. M. Gorelick. Earthquake triggering and large-scale geologic storage of carbon dioxide. *Proc. Natl. Acad. Sci. USA*, 109(26):10164–10168, 2012.

[173] M. L. Zoback and M. Zoback. State of stress in the conterminous United States. *J. Geophys. Res.*, 85(B11):6113–6156, 1980.